UNIVERSIDAD AUTÓNOMA DE MADRID
DEPARTAMENTO DE BIOQUÍMICA

NOVEL APPROACHES FOR THE MEASUREMENT OF TUMORAL pO_2 BY MAGNETIC RESONANCE METHODS

JESÚS PACHECO TORRES

MADRID, 2013

DEPARTAMENTO DE BIOQUÍMICA
FACULTAD DE MEDICINA
UNIVERSIDAD AUTÓNOMA DE MADRID

NOVEL APPROACHES FOR THE MEASUREMENT OF TUMORAL pO_2 BY MAGNETIC RESONANCE METHODS

Memoria de Tesis doctoral presentada por:
JESÚS PACHECO TORRES
Licenciado en Ciencias Químicas, para optar al grado de Doctor por la Universidad Autónoma de Madrid

Directores de tesis:

Dra. PALOMA BALLESTEROS GARCÍA
Dr. SEBASTIÁN CERDÁN GARCÍA-ESTELLER
Dra. PILAR LÓPEZ LARRUBIA

Tesis doctoral realizada en el Instituto de Investigaciones Biomédicas “Alberto Sols”

Paloma Ballesteros García. Catedrática de Química Orgánica de la Facultad de Ciencias de la Universidad Nacional de Educación a Distancia

Sebastian Cerdán García-Esteller, Profesor de Investigación del Instituto de Investigaciones Biomédicas "Alberto Sols", Consejo Superior de Investigaciones Científicas

Pilar Lopez-Larrubia, Científico Titular del Instituto de Investigaciones Biomédicas "Alberto Sols" Consejo Superior de Investigaciones Científicas

CERTIFICAN:

Que D**. Jesús Pacheco Torres** ha realizado en nuestros laboratorios y bajo nuestra dirección el presente trabajo que constituye su Tesis Doctoral, y que el mismo reúne a nuestro juicio todos los requisitos necesarios para su defensa pública.

Y para que así conste, firmamos el presente certificado en Madrid, a 30 de Septiembre de 2013.

Fdo.: Paloma Ballesteros García
Directora de Tesis
Catedrática de Universidad, UNED

Fdo.: Sebastián Cerdán García-Esteller
Director de Tesis
Profesor de Investigación, CSIC

Fdo.: Pilar López Larrubia
Directora de Tesis
Científico Titular, CSIC

Vº Bº Tutor: Juan Bernal Carrasco
Profesor de Investigación, CSI

A mis padres
A mis hermanos

“Imagination is more important than knowledge. For knowledge is limited to all we now know and understand, while imagination embraces the entire world, and all there ever will be to know and understand.”
Albert Einstein

“Bienaventurados los humildes pues ellos heredarán la tierra.”
Mateo 5:5

AGRADECIMIENTOS/ ACKNOWLEDGEMENTS

Han transcurrido más de 7 años desde que, tras algunos intentos fallidos, decidí trasladarme a Madrid para empezar un nuevo doctorado. Por ello, me gustaría empezar dando las gracias a todos aquellos que me concedieron esta nueva oportunidad. No fue una decisión sencilla, y las dudas me han asaltado durante estos años. Ahora, al final de este período, me alegro de haber perseverado. Sin embargo, no ha sido mérito exclusivamente mío. Fue posible gracias a la compañía de personas que me animaron y empujaron, personas que no me permitieron abandonar: mi familia, mis amigos, mis compañeros, mis directores… Esta tesis es en gran parte un logro suyo, por apoyarme durante todo este tiempo.

Es imposible nombrar en estas líneas a todas las personas e instituciones que durante este tiempo han pasado por mi vida y que, de una manera u otra, me han ayudado llegar hasta aquí. A todos ellos expresarles mi profundo agradecimiento. No obstante, existen ciertas personas e instituciones a las cuales, por su implicación directa en estos años de trabajo y formación, me gustaría mencionar. Empezaré dando las gracias a todo el personal del laboratorio del Prof. Ralph P. Mason en la UT Southwestern en Dallas. La labor allí realizada es una parte muy importante de esta tesis, y en general, de toda mi carrera científica. Me gustaría señalar especialmente al Dr. Dawen Zhao, por hacerme partícipe de su investigación y por todo su tiempo, esfuerzo y dedicación. También agradecer al Prof. Ralph P. Mason la confianza depositada en mí y su apoyo incondicional durante todo este tiempo. Finalmente y sin por ello ser menos importante, mi más sincero y profundo agradecimiento a Sandy y Jane, capaces de abrirme las puertas de su casa y hacerme sentir uno más de su familia.

Me gustaría destacar mi estancia en el Cancer Research Institute, en Cambridge, en el laboratorio del Prof. John Griffiths, como increíblemente positiva. Estoy muy agradecido a todas las personas que forman este laboratorio, en especial al Dr. Shen-Han Lee por tantas horas de trabajo compartido y al Prof. John Griffiths por ofrecerme esta fantástica oportunidad. Si bien el trabajo allí realizado no está directamente reflejado en esta tesis, muchos de los experimentos aquí descritos no habrían sido posibles sin los conocimientos y la experiencia adquiridos durante este período en Cambridge.

El laboratorio de la Dra. Paloma Ballesteros fue mi primer destino al trasladarme a Madrid. En él, a pesar del difícil ambiente por todo cuanto nos rodeaba, aprendí mucho y tuve la suerte de coincidir con grandes compañeros: Manuel, Jordi, Elena, María, Viviana y Carmen. En está época descubrí que aún quedaba una parte de químico dentro de mí y que me sigo sintiendo cómodo en un laboratorio de síntesis orgánica. El laboratorio del Dr. Sebastián Cerdán, en el Instituto de Investigación Biomédicas “Alberto Sols” ha sido mi “centro base” durante todos estos años. Aquí he tenido la oportunidad de trabajar con gran cantidad de investigadores y personal técnico de los que guardo muy buen recuerdo, como Marisa, Alejandra, Marina, Blanca, Daniel, Martina, Santiago, Laura, Alex, Inês, Tiago, Margarida, Rui,… Durante este tiempo, también me mantuve en estrecha colaboración

con el laboratorio de la Dra. Pilar López, especialmente con Miguel, Ana y Eva. Me gustaría extender mi gratitud a los servicios generales del IIB, en especial al SIERMAC y su jefa de servicio, Teresa Navarro, al Animalario y al servicio de Imagen Científica. Todos ellos desarrollan una excelente tarea sin la cual nuestra labor sería mucho más complicada cuando no imposible. Finalmente, agradecer también a otros investigadores y personal del IIB con los que tuve el placer de trabajar estrechamente, especialmente a Carlos, Ana, Anita, Iván y Paloma… De entre todas las personas con las que tuve el placer de coincidir, existe un grupo que, por una razón u otra, son especiales para mí: Patricia, Rocío, Teresa, Valeria y Nuria. Muchas gracias a todas por vuestra compañía, ayuda, enseñanzas, paciencia….

Mi agradecimiento especial también al Prof. Julio Alvarez-Builla y su grupo de Síntesis Orgánica de la Universidad de Alcalá de Henares por proporcionarme el misonidazol y otros de los nitroderivados utilizados en esta tesis. Se trata de compuestos sintetizados "a medida" y sin ellos no hubiera podido realizar muchos de los experimentos descritos. También me gustaría dar las gracias a los proyectos MULTIMAG e I2M2 de la Comunidad de Madrid por aportar la financiación necesaria para llevar a cabo este trabajo.

He tenido la suerte de contar con tres fantásticos directores de tesis sin los cuales este trabajo no hubiese alcanzado buen puerto. Me gustaría empezar agradeciendo a la Dra. Pilar López, quien fue capaz de ejercer como codirectora, compañera y amiga, combinándolo todo de manera admirable. Creo que estos años han sido un proceso de aprendizaje mutuo. Yo aún sigo aprendiendo de ella a todos los niveles, y espero continuar haciéndolo mucho tiempo. A la Prof. Paloma Ballesteros le debo la base de toda esta tesis, sin la cual nada hubiese sido posible. Gracias por llevar a cabo ese trabajo en ocasiones invisible, pero absolutamente imprescindible para todos. Y por supuesto, mi más profundo, sincero y sentido agradecimiento para el Prof. Sebastián Cerdán. Quisiera expresar mi admiración y reconocimiento por toda su trayectoria, por el trabajo realizado y los medios puestos a disposición de todos los que a él nos acercamos. En particular me gustaría subrayar sus enseñanzas y la confianza depositada en este proyecto y en mi persona, incluso en aquellos momentos en los que ni yo mismo creía en mí ni en nuestro objetivo.

Los buenos amigos te acompañan y te marcan. Mucha gente pasa por tu vida de manera temporal. Yo tengo la suerte de contar con unas cuantas personas que han estado a mi lado durante mucho tiempo: Carlos, Andrés, Mónica, David, Juana María, Antonio… A todos ellos un abrazo y mi profundo agradecimiento por ser parte de mí.

Por último, agradecer a la piedra angular sobre la que me sostengo y sin la cual todo se vendría abajo: mi familia. A mis padres, de manera especial, por estar siempre tan cerca y presentes, por acudir sin ser llamados, por el respeto a las decisiones tomadas, el apoyo y los buenos consejos. A mis hermanos Pablo y Rosalía, por ser el espejo en el que mirarme cada día y por darme fuerza para

seguir intentado mejorar y llegar aún más lejos. A mi abuela y tíos abuelos, simplemente por estar ahí. A mis primos y mis tíos, por construir una red de seguridad para todos en las que frenar nuestras caídas y ayudarnos a levantarnos.

Decía la Madre Teresa de Calcuta, "da siempre lo mejor de ti, y lo mejor vendrá..." Durante estos años siempre intenté dar lo mejor de mí. Ahora soy consciente de lo afortunado que fui pues lo mejor vino a través de las personas que me acompañaron.

Index

Index of figures

Index of tables

Index of schemes

Abstract/Resumen

Increasing evidence supports a strong relationship between tumor hypoxia and tumor aggressiveness, poor outcome and resistance to therapies. Tumor hypoxia results from the negative balance between the oxygen demands of the tissue and the capacity of the neovasculature to deliver satisfactory oxygen provisions. A plethora of treatments have been proposed recently to overcome specifically the hypoxic burden (photodynamic therapy, hyperoxic gas breathing during radiotherapy, hypoxia sensitive therapeutics …), aimed to improve the results of oncotherapy. However, the lack of suitable methods to assess tumor hypoxia in the clinic, makes it not possible to identify *a priori* those tumors potentially sensitive to the hypoxic directed treatment and, thus, those patients that could benefit from these novel therapies. Magnetic Resonance (MR) methods are well endowed to fulfill these needs. On these grounds, the aim of this thesis is to develop and implement novel strategies to measure tumor hypoxia using MR methods. To this end, we followed two independent approaches; 1) The development and implementation of novel exogenous contrast agents revealing tissue hypoxia and 2) The development and implementation of new and advanced methods of endogenous imaging contrast sensitive to the environmental oxygen tension.

In our first approach, we synthesized and characterized new 2-nitromidazole derivatives as exogenous hypoxia markers. Their potential use was investigated both in vitro and in cell cultures, and the results obtained compared with those generated by commercial hypoxia markers. We characterized the main determinants of the metabolism of nitroimidazole derivatives proposing a new mechanism for their bioreduction and sensitivity to hypoxia, implementing a new method to obtain hypoxia maps from the bioreduction of nitroimidazoles as detected non invasively by ^{1}H Magnetic Resonance Spectroscopy Imaging (MRSI).

In our second approach, we exploited the sensitivity of the relaxation times of endogenous tissue water to physiological oxygen concentrations. The paramagnetic nature of oxygen, induced appreciable, concentration dependent, T_1 shortening in vivo, as revealed by T_1 weighted MRI, an approached named Tissue Oxygenation Level Dependent (TOLD). Based on these images, we designed and tested a new MRI methodology to identify those tumors that could benefit from a hypoxia directed therapy as breathing gas mixtures with high oxygen content. Taken together, our results provide a new frame for the non invasive measurement of tumor hypoxia by Magnetic Resonance methods.

Cada día más evidencias apoyan la existencia de una fuerte relación entre hipoxia y agresividad tumoral, así como con un peor pronóstico y mayor resistencia a la terapias oncogénicas. La hipoxia tumoral resulta del balance negativo entre las demandas tisulares de oxígeno y la capacidad de la neovasculatura para satisfacer dichas necesidades. Recientemente, se ha propuesto toda una plétora de tratamientos específicamente dirigidos a superar el daño originado por la hipoxia (terapia fotodinámica, respiración de gases con alto contenido en oxígeno durante la radioterapia, fármacos sensibles a la hipoxia…) con el objetivo de mejorar los resultados de la oncoterapia. Sin embargo, la falta de una metodología clínica para evaluar la hipoxia tumoral hace imposible detectar, *a priori*, aquellos tumores potencialmente sensibles a los tratamientos dirigidos especificamente a la hipoxia y, por lo tanto, aquellos pacientes que específicamente se podrían beneficiar de estas nuevas terapias. Los métodos de Resonancia Magnética (RM) se presentan como una buena alternativa para realizar dicha tarea. En base a esto, el objetivo de esta tesis es el desarrollo y la implementación de nuevas estrategias para medida de la hipoxia tumoral empleando métodos de RM. Con este objetivo, se emplearon dos aproximaciones independientes: 1) Desarrollo e implementación de nuevos agentes de contraste exógenos para la mediada de hipoxia tisular y 2) Desarrollo e implementación de nuevos y avanzados métodos sensibles a la tensión de oxígeno utilizando un contraste endógeno.

En nuestro primer enfoque, sintetizamos y caracterizamos nuevos derivados de 2-nitroimidazol como marcadores de hipoxia exógenos. Su potencial aplicación se investigó in vitro y en cultivos celulares, y los resultados obtenidos se compararon con los generados por marcadores comerciales de hipoxia. Se caracterizaron los factores principales del metabolismo de los derivados de 2-nitroimidazol, proponiendo un nuevo mecanismo para su bioreducción y sensibilidad a hipoxia. Se implementó un nuevo método para la obtención de mapas de hipoxia basados en la bioreducción de 2-nitroimidazoles detectada de manera no invasiva mediante Imagen Espectroscópica de Resonancia Magnética de ^{1}H.

En nuestra segunda aproximación, utilizamos la dependencia de los tiempos de relajación del agua tisular con la concentración fisiológica de oxígeno. La naturaleza paramagnética de la molécula de oxígeno induce acortamientos del T_1 in vivo apreciables y dependientes de la concentración de oxígeno, según se observa en la Imagen de Resonancia Magnética (IRM) pesada en T_1, en una aproximación denominada Nivel Dependiente de Oxigenación Tisular. Basándonos en estas imágenes, se diseñó y se probó una nueva metodología de IRM para identificar aquellos tumores que podrían beneficiarse de una terapia dirigida a la modulación de la hipoxia, como respirar mezclas de gases con alto contenido en oxígeno. En conjunto, nuestros resultados proporcionan una nueva metodología para la medida no invasiva de la hipoxia tumoral por métodos de RM.

Abbreviations & Acronyms

19F RI: ^{19}F Retention Index.

ADC: Apparent Diffusion Coefficient.

ANOVA: analysis of variance.

ARDVARC: Alternating Relaxation Delays with Variable Acquisitions for Reduction of Clearance effects.

ARNT (HIF-1β): Aryl hydrocarbon Receptor Nuclear Translocator.

ATP: Adenosine-5'-triphosphate.

B0: Magnetic Field.

BOLD: Blood Oxygen Level Dependent.

CHO: Chinese hamster ovary cells.

CPMG: Carr Purcell Meiboom Gill.

CREB: cyclic AMP-response-element-binding protein.

Cu-ATSM: Copper diacetylbis-N(4)-methylthiosemicarbazone.

DCE: Dynamic Contrast Enhanced.

DMEM: Dulbecco's Modified Eagle Medium.

DTI: Diffusion Tensor Imaging.

DTNB: 5,5'-dithiobis(2-nitrobenzoate).

DWI: Diffusion Weighted Imaging.

EF5: 2-(2-Nitro-1*H*-imidazol-1-yl)-*N*-(2,2,3,3,3-pentafluoropropyl)acetamide.

EPI: Echo Planar Imaging.

EPR: Electron Paramagnetic Resonance.

FBS: Fetal Bovine Serum.

FIH: Factor Inhibiting HIF-1.

FOV: Field Of View.

FREDOM: Fluorocarbon Relaxometry using Echo planar imaging for Dynamic Oxygen Mapping.

GEMS: Gradient Echo Multiple Slice.

GR: Glutathione Reductase.

GSH: Reduced glutathione.

GSSG: Oxidized glutathione.

Hb: Hemoglobin.

HFB: Hexafluorobenzene.

HIF-1: Hypoxia-Inducible Factor-1.

HMDSO: Hexamethyldisiloxane.

HRE: Hypoxia-Response Element.

HR-MAS: High Resolution Magic Angle Spinning.

ISUCA: (+/-)2-(Imidazol-1-yl)Succinic Acid.

MISO: Misonidazole.

Misonidazole: (*RS*)-1-Methoxy-3-(2-nitroimidazol-1-yl)propan-2-ol.

MR: Magnetic Resonance.

MRI: Magnetic Resonance Imaging.

MRS: Magnetic Resonance Spectroscopy.

MRSI: Magnetic Resonance Spectroscopy Imaging.

Mtx: acquisition matrix.

NADH: Nicotinamide Adenine Dinucleotide.

NADP+: β-Nicotinamide Adenine Dinucleotide Phosphate Oxidized.

NADPH: β-Nicotinamide Adenine Dinucleotide Phosphate Reduced.

NF-kB: Nuclear Factor-kB.

NISUCA: Dimethyl 2-(2-Nitro-1*H*-imidazol-1-yl)succinate.

NIMAC: Methyl 2-(2-nitro-1H-imidazol-1-yl)acetate**.**

NIR: Near Infrared.

NPSH: Nonprotein Sulfhydryls.

OMRI: Overhauser-enhanced MRI.

P450ase : NADPH:Cytochrome-P450 reductase.

PCr: Phosphocreatine.

PET: Positron Emission Tomography.

PFC: Perfluorocarbon.

PHD: Prolyl hydroxylase-domain protein.

Pi: Inorganic Phosphate.

Pimonidzole: [(2-nitro-1H-imidazol-1-yl)methyl]-1-piperidineethanol (Ro 03-8799).

PISTOL: Proton Imaging of Siloxanes to map Tissue Oxygenation Levels.

PLSD: Protected Least Significant Difference.

PTSA: para-Toluenesulfonic acid.

PRESS: Point Resolved Spectroscopy.

pO_2: Partial pressure of oxygen.

pVHL: Von Hippel–Lindau tumor-suppressor protein.

RARE: Rapid Acquisition Relaxation Enhancement.

RIF: Radiation Induced Tumors.

ROS: Reactive Oxygen Species.

SE: Standard Error.

SEMS: Spin Echo Multiple Slice.

SI: Signal Intensity.

SOD: Superoxide Dismutase.

SPECT: Single-Photon Emission Computed Tomography.

SNR: Singal to Nosie Ratio.

T: Temperature.

T_1W: T_1 weighted images.

T_2W : T_2 weighted images.

T_2*W: T_2* weighted images.

TBAI: Tetrabutylammonium Iodide.

TE: Echo Time.

TNB: 2-nitro-5-thiobenzoate.

TOLD: Tissue Oxygen Level Dependent.

TR: Repetition Time

TSP: Trimethylsilyl -2,2´,3,3´tetradeutero-propionic acid.

VAPOR: Variable Pulse Power and Optimized Relaxation Delays.

VDT: Volume Doubling Time.

1. INTRODUCTION

The extracellular space of tissues is located between the cellular architectures and the capillary network providing a vital space for intercellular communication and regulatory metabolic interactions (Figure 1). The biochemical profile of this compartment modulates many vital intracellular functions including differentiation (47), tissue regeneration (222), angiogenesis (139), metastasis (33), proliferation (160) and apoptosis (69) or necrosis (195), among others. The extracellular millieu is characterized by a collection of environmental properties, such as pH, partial pressure of oxygen (pO_2), ionic composition and diffusion. These are significantly different from those of the intracellular or vascular spaces, configuring in this way a physiologically distinct compartment. Alterations in the environmental properties of tissues are known to occur very early during disease development, providing precious information for the diagnosis, prognosis and therapy assessment of the most prevalent and morbid pathologies in developed countries, with particular emphasis in cancer and ischemic episodes (61,92,132).

The biochemical properties of the microenvironment result from the balance between the cellular uptake and metabolism of substrates as glucose and oxygen from the capillaries, and the removal of waste products as lactate and H^+ through the tissue microvasculature (Figure 1a). Intracellular oxidative metabolism leads simultaneously to the production of freely diffusing CO_2 and H_2O (in fast equilibrium with HCO_3^- and H^+ through the carbonic anhidrase enzyme). Reductions in glucose or oxygen delivery either by systemic limitations or inadequate performance of the local capillary network, result in extracellular lactate and proton accumulation, two conditions commonly found during the early development of most pathologies, including tumors (Figure 1b). On these grounds, non invasive imaging of the microenvironment has gained substantial scientific and clinical interest in the last decades (63,88,190). Several techniques have been used for this purpose: positron emission tomography (PET) (13,189,212), single photon emission computed tomography (SPECT) (16,56,158), immunohistochemistry (114)... Among them, Magnetic Resonance (MR) methods present several favorable properties as noninvasiveness, high spatial and temporal resolution, good contrast between the different tissues and use no ionizing radiation, making the approach particularly suitable to investigate the properties of the extracellular microenvironment.

1.1. Hypoxia

The quantitative measurement of the oxygen tension in healthy and diseased tissues represents a long-standing endeavor of medicine and biology since Carl Scheele, Joseph Priestly and Antoine Lavoisier discovered molecular oxygen (48). The concept of hypoxia indicates oxygen shortage. In normal tissues as heart or brain, hypoxia may be attributed to ischemia, where the delivery of oxygen is insufficient to maintain normal physiological function. Hypoxia may occur due to a local decrease in vascular flow or to insufficient hemoglobin saturation. For instance, an acute myocardial

infarct will result in rapid oxygen depletion and loss of mechanical function. It has been shown, as expected, that the effects of hypoxia are much more rapid in the beating heart than in the arrested heart, and indeed, the rate loss of developed pressure is directly proportional to decrease in partial pressure of oxygen (pO_2) (225).

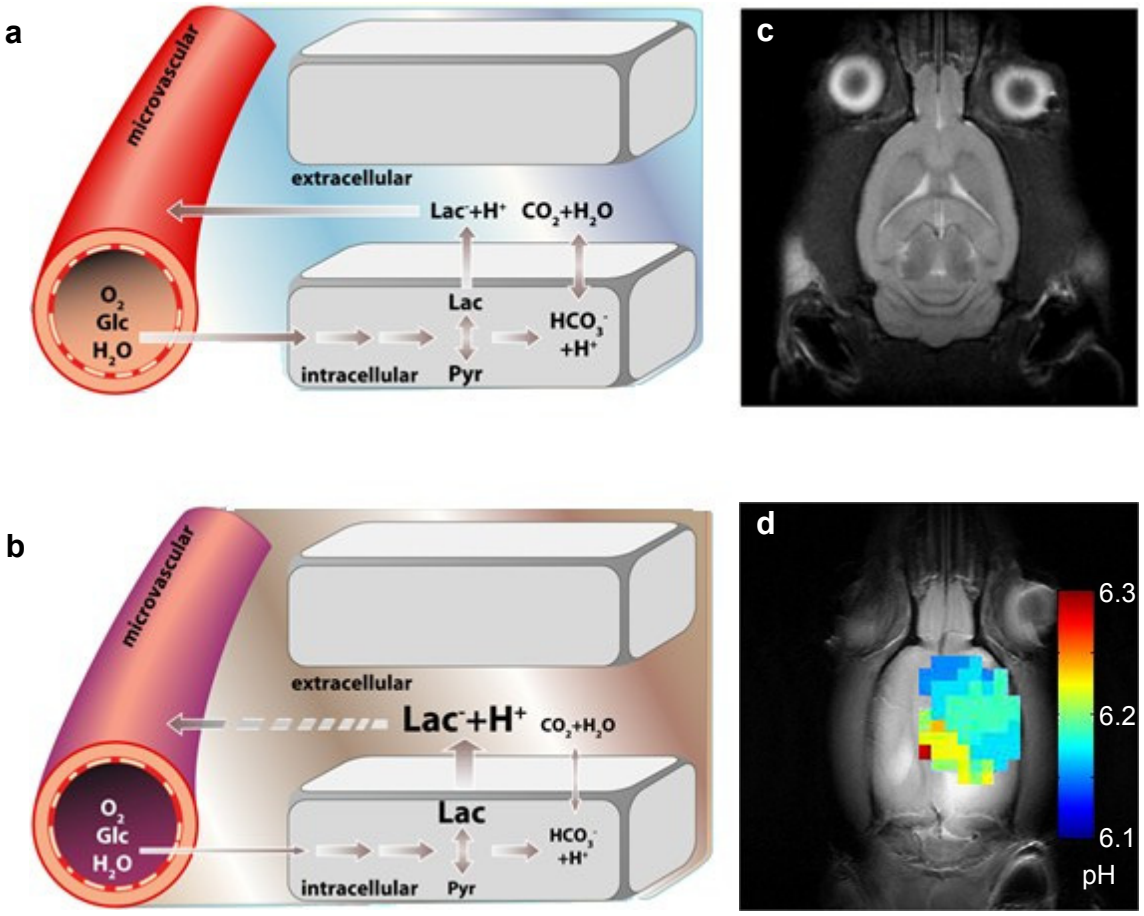

Figure 1. The extracelular microenvironment of tissues.
The extracellular microenvironment of tissues is located between the vascular and intracellular spaces. a) Under normal conditions it is characterized by physiological oxygen tension, and relatively low concentrations of lactate and H^+ due to the efficient perfusion and removal of metabolic products by the microvasculature. b) Reduced performance of the microvasculature (purple) under most pathological situations results in, reduced oxygen tensions, and concomitant lactate and H^+ accumulation in the diseased extravascular space (brown). Magnetic resonance imaging has progressed from conventional T_2 weighted anatomical images (c) to molecular images revealing particular properties of the extracellular environment as pH in the brain of a rata bearing a C6 tumor (d). In this work we extend these approaches to the imaging of oxygen tensions.

1.1.1. Tumor hypoxia

The definition of hypoxia in tumors may become far more complex, since neoplastic tissue is aberrant with no particular normal function, yet the well documented ability to grow and adapt to stress. Low oxygen levels are a recognized prognostic marker in oncology, with numerous reports linking tumoral hypoxia to therapy failure and poor patient outcome (196). To our knowledge, Gray et al. (65) were the first to provide evidence that some tumors are hypoxic in vivo. In particular, they

showed that human bronchial carcinomas with necrotic areas, located approximately 150 µm away from the nearest blood vessel, had lower oxygen tension than the surrounding tissues. It was not until 1988, however, that a direct relationship between tumor hypoxia and treatment failure was reported (59). Lymph nodes from squamous cell carcinoma of the head and neck showed significant differences in the median pO_2 (as investigated with polarographic electrodes) between tumors responding and not responding to radiotherapy. Since then, multiple studies have confirmed that pO_2 constitutes a crucial prognostic marker of patient outcome and therapy success (50,145,165,196), including chemotherapy (66,209), radiotherapy (66,72), photodynamic therapy (207,209) and surgical tumor resection (78). Indeed, a threefold increase in radio-resistance may occur when cells are irradiated under hypoxic conditions compared to cells irradiated under normoxic conditions (pO_2 > 15 Torr), in a single radiation dose (65).

In addition to increased resistance to therapies, a direct relationship has been proven between hypoxia and aggressiveness in different tumor types (50,80,208), suggesting that hypoxia constitutes a universally negative factor in the prognosis and treatment of neoplastic diseases (145,165). As a consequence, a collection of adjuvant therapeutic interventions related to hypoxia have been proposed in recent decades to improve the therapeutic outcome of cancers. These include i) "dose-painting", booster regimens and intensity modulated radiation therapy (IMRT) (55,117,119,198,224), ii) administration of adjuvant hypoxic cell selective cytotoxins, even though clinical trials with tirapazamine were discontinued and iii) breathing hyperoxic gas mixtures. Indeed, many clinical trials have explored oxygen (O_2), carbogen (mixture of 95 % O_2 and 5 % CO_2) or hyperbaric gas breathing (154). The meta analysis by Overgaard et al. (152,153) of some 10,000 patients indicated a clinical advantage for manipulating tumor hypoxia. However, the overall conclusion was that there was a pressing need to identify those tumors (viz. patients) that would actually benefit from it. On these grounds, more precise and robust measurements of the oxygen levels in vivo would allow a better selection of patients responding positively to hypoxia-directed treatments and a more adequate understanding of the significance of tumor oxygen levels on the outcome of the different therapies.

It is relevant to point out here that no single pO_2 threshold can be widely applied to determine the limit for hypoxic and normoxic areas in all tissues. In other words, hypoxia does not have an absolute definition and does not entail a universal threshold. Normal tissue shows a typical Gaussian distribution of oxygen tensions with values of pO_2 ranging from 20 to 80 mmHg, with a median value around 50 mm Hg, none of them less than 10mm Hg (6). However, the oxygen levels reported for tumors are very often lower than those of healthy tissues. In this context, oxygen tensions that may be considered normoxic in some tissues may represent hypoxic situations for others, and vice versa, as illustrated in Table 1.

Table 1. Median values of pO_2 determined in different tissues and cancer types.

Healthy Tissue	Median pO_2 (mmHg)	Reference
Breast	52	(206)
Subcutis	51	(206)
Skeletal muscle	37	(206)
Cervix	42	(207)
Pancreas	57	(210)
Rectal mucosa	52	(210)
Kidney	31	(210)
Skeletal muscle	25 -30	(210)
Liver	30	(210)
Brain	24 - 27	(210)
Neoplastic tissue	**Median pO_2 (mmHg)**	**Reference**
Breast cancer	3-15	(206)
K1735 malignant melanoma	37.8 ± 5.1	(231)
RENCA renal cell carcinoma	24.8 ± 17.9	(231)
Lewis lung carcinoma	1.8 ± 1.1	(231)
Cervix cancer	10	(207)
Soft tissue sarcoma	20/7.5[a]	(28)
Cervical carcinoma	4.5	(27)
Squamous carcinoma metastatic to lymph nodes	12.6	(27)
Head and neck cancer	4.8/4.3[b] - 9	(29) - (145)
Uterine cervix	12.5 - 9	(207) - (210)
Prostate Cancer	2 - 21	(210)
Brain tumors	13	(210)

[a] Median values for non-recurrent/recurrent tumors respectively.
[b] Median values for primary/metastatic (cervical nodes) tumors respectively.

1.1.2. Causes and consequences of tumor hypoxia

Tissue hypoxia arises from an imbalance between the oxygen demands of the tissue and the capacity for oxygen delivery of the neighboring microvasculature. Its main causes and consequences are summarized in Figure 2.

Oxygen consumption in tumors may be increased up to five-fold as a result of the augmented metabolic demand of rapidly growing cancerous tissues (134). On the other hand, oxygen availability to the tumor will depend on the adequate performance of its microvascular bed, and thus on the efficiency of neovascularization (77,134,144). These processes are tightly balanced in normal tissues, but their regulation is often lost in cancer, resulting in abnormal microvasculature performance, reduced perfusion and impaired oxygen or nutrient delivery to the tumor (57,138). Vascular deficiencies in tumors can be broadly divided into structural or functional. Structural deficiencies include caliber variations with dilated and narrowed single branches of tumor vessels, chaotic vascular networks and disturbed precapillary architecture. Functional limitations consist basically of:

immature vessels, increased transcapillary and vascular permeability, interstitial hypertension, increased flow resistance and nonperfusing vessels (57,133). However, the aberrant neovasculature may not be the only cause of reduced oxygen availability in the tumor. Additional causes may include low environmental pO_2, as in pulmonary disease, or the inability of cells to use oxygen properly because of a toxic challenge, as in cyanide poisoning (80). Tumor- or therapy-related anemia may also dicrease the global capacity of blood to transport oxygen, aggravating this situation (205).The first recognized consequence of hypoxia is the shift from aerobic to anaerobic metabolism (42), a circumstance known as the Warburg effect (60). Reduced oxygen availability is currently known, however, to induce important genomic and proteomic changes in cells. Numerous links have been reported between tumor hypoxia and an increased ability to metastasize (112,163), induce angiogenesis (77,112), apoptosis (57,64,71), cell immortalization (186), expression of growth factors for cell proliferation (71,112,187), cellular dedifferentiation (74) and genetic instability (80). All these changes are largely thought to be a result of hypoxia-driven alterations in the expression of a battery of hypoxia-sensitive genes (35,71,187). Remarkably, very important overlaps exist between hypoxia-induced genes and activated cancer pathways. Some oncogenes, tumor suppressor genes, stress proteins and cytokines induced by hypoxia are constitutive of well-known cancer pathways, and increasing evidence supports the close dialog between hypoxia and some oncogenic signaling pathways (126).

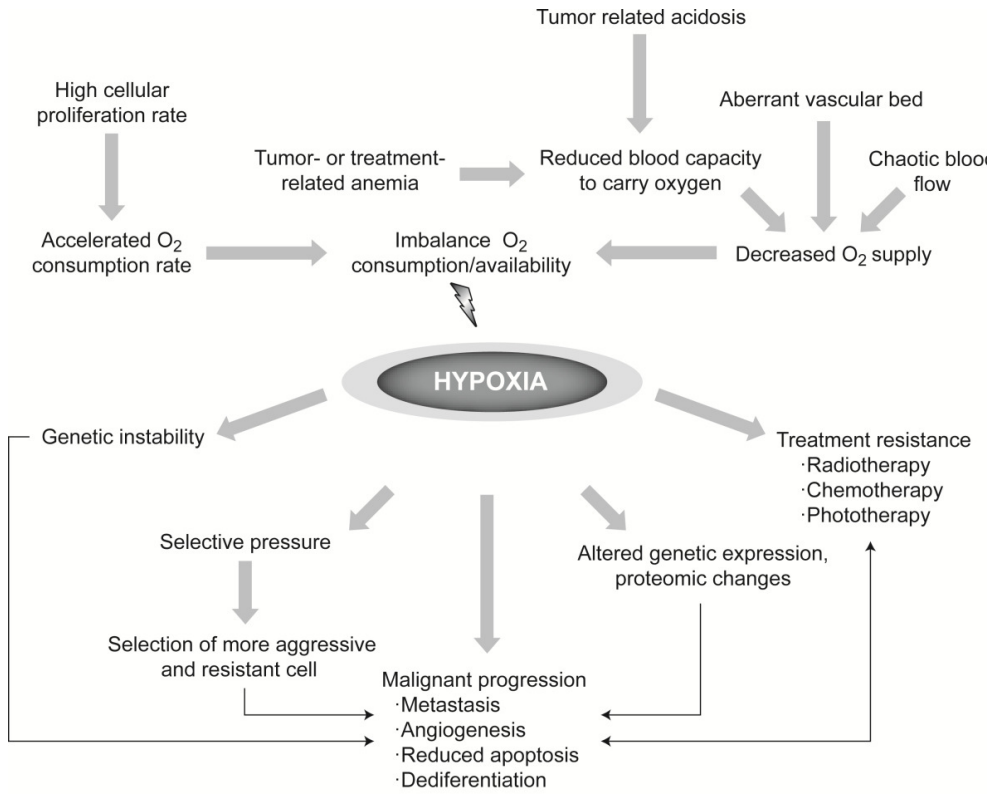

Figure 2. Main causes (top) and consequences (bottom) of tumor hypoxia.

1.1.3. Molecular mechanisms of hypoxia

Figure 3 illustrates our current understanding of the molecular events underlying hypoxic responses. Hypoxia-responsive genes are activated by means of hypoxia-inducible factor-1 (HIF-1). HIF-1 is an oxygen-sensitive transcription factor that eventually binds to hypoxia-response elements (HREs), activating a battery of genes to recover oxygen homeostasis. HIF-1 is a heterodimer that consists of the constitutively expressed aryl hydrocarbon receptor nuclear translocator (ARNT or HIF-1β) and the HIF-1α subunit sensitive to oxygen concentration (126,196). The translation of high oxygen levels to decrease HIF-1 activity is driven by the prolyl hydroxylase-domain protein (PHD), hydroxylating the HIF-1α subunit and allowing the interaction with the Von Hippel– Lindau tumor-suppressor protein (pVHL). This complex is recognized by the E3 ubiquitin-protein ligase, which ubiquitinates HIF-1α and labels it for proteasomal degradation (187). Oxygen is the limiting factor for these reactions under normoxic conditions. Under hypoxic conditions, HIF-1α is not hydroxylated and can upregulate its target genes. There is an additional regulation sentinel, the factor inhibiting HIF-1 (FIH). FIH is an oxygen- and iron-dependent hydroxylase operating over HIF, but in a different residue than PHD, inhibiting the interaction of HIF with CBP/ p300, an essential coactivator of HIF (188). As these two hydroxylases have different oxygen sensitivities, it is possible to fine tune the resulting HIF-1 activity to different oxygen levels (179). In addition to oxygen, HIF-1 can also be activated in response to other stimuli-like growth factors, cytokines and some signaling pathways, such as phosphatidylinositol 3-kinases (PI-3k), protein kinase B (Akt)and the Ras-MEK-ERK pathway (168,188). HIF-1 is not the only transcription factor activated by oxygen limitations. Additional factors include cyclic AMP-response element- binding protein (CREB), metal-transcription factor-1 and nuclear factor-kB (NF-kB) (71,80). There are other cellular responses to low oxygen levels, including the unfolded protein response (52) and inhibition of the initial step of mRNA translation (221).

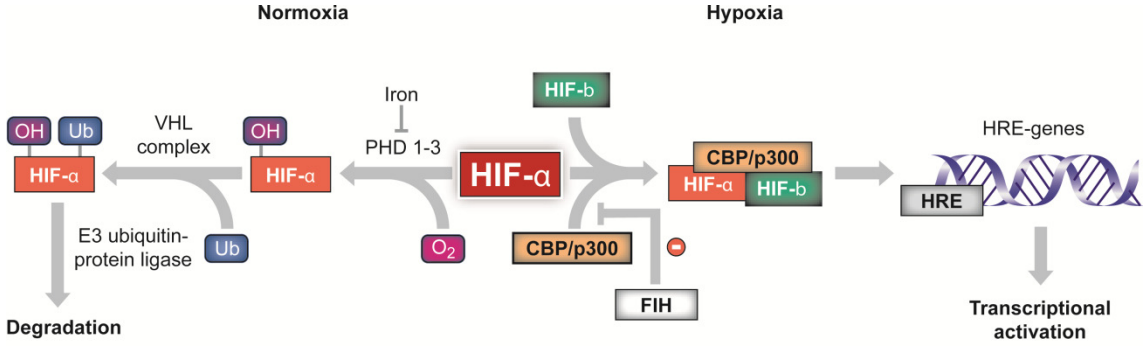

Figure 3. Regulation of hypoxia-inducible factor (HIF) activity by molecular oxygen.
Oxygen (O_2) is the limiting factor for HIF-α hydroxylation. Under normoxic conditions, the HIF-α subunit is hydroxylated by prolyl hydroxylase-domain protein 1–3 (PHD 1–3). The hydroxylated HIF-α is recognized by the Von Hippel–Lindau (VHL) complex and labeled with ubiquitin for proteasomal degradation through the E3 ubiquitin-protein ligase. Under hypoxic conditions, HIF-α is not hydroxylated, forming a complex with aryl hydrocarbon receptor nuclear translocator (ARNT; HIF-β) and CBP/p300 that upregulates the pleiotropic expression of genes containing a hypoxia-responsive element (HRE). FIH, factor inhibiting HIF-1.

Many indications suggest that HIF-1 is the molecule responsible for hypoxia-driven tumor aggressiveness and resistance to therapy. A number of experimental studies and clinical reports have provided a direct correlation between HIF-1α overexpression and cancer progression, invasiveness, resistance to therapy, and poor patient outcome (35,71,112). Nevertheless, the role of HIF-1α in tumor growth and invasiveness may be complemented by other factors, such as the microenvironment, which may even play a determinant role in these processes (21). Molecular imaging approaches are being designed to visualize directly and noninvasively the molecular determinants of hypoxia or related signaling events and their behavior in targeted tumor therapies (193). Currently, the development of new molecular imaging methods to visualize directly and noninvasively hypoxia and hypoxia related pathways is one of the most active areas of research in the molecular imaging community (193).

1.1.4. Metabolic and cellular heterogeneity of hypoxia

Limitations in oxygen levels influence differently various cellular processes and have different impacts in normal and neoplastic cells (Table 2). Although normal cells react to hypoxia through cell cycle arrest, apoptotic or necrotic mechanisms, tumor cells adapt more easily to the hostile environment, developing sophisticated escape mechanisms and becoming resistant to therapies. The differential effects of hypoxia on the vital cellular events of normal and neoplastic cells result in different survival rates, even in spatially very close cellular populations, leading to highly heterogeneous tissue and tumor oxygenation environments.

Table 2. Differential effects induced by hypoxia in normal or tumoral cells.

Normal cells [a]	Tumor cells [b]
Apoptosis by p53-dependente and p53–independent pathways	Adaptation to hostile environment (deprivation of nutrients and oxygen)
Necrotic cell death occurs below a critical energy levels	Develop escape responses to the hostile environment (tumor cell detachment and subsequent adhesion, migration, angiogenesis, tissue remodeling)
Cell cycle arrest, quiescence and differentiation	Increased resistance for cell cycle arrest, differentiation and apoptosis
Impaired cell growth	Increased resistance to different therapies

[a] These effects are also observed in some neoplastic cells. [b] These changes could explain hypoxia associated tumor aggressiveness, metastatic potential and resistance to various therapies (166).

Figure 4 summarizes the effects of different degrees of hypoxia on some crucial metabolic pathways involved in cellular survival. Notably, the boundary pO_2 values limiting the efficacy of the various cellular processes and therapies are different. Although vital events, such as the oxygen consumption by mitochondrial respiration and the loss of apoptotic potential, require extremely severe reductions

with pO_2 below 0.5 mmHg, different therapies become ineffective below 15 mmHg. It should be noted, however, that these boundary values derive from different experimental designs for each process, and that other factors (pH, nutrient levels, etc.) may also modulate oxygen sensitivity, making the resulting panorama even more complex

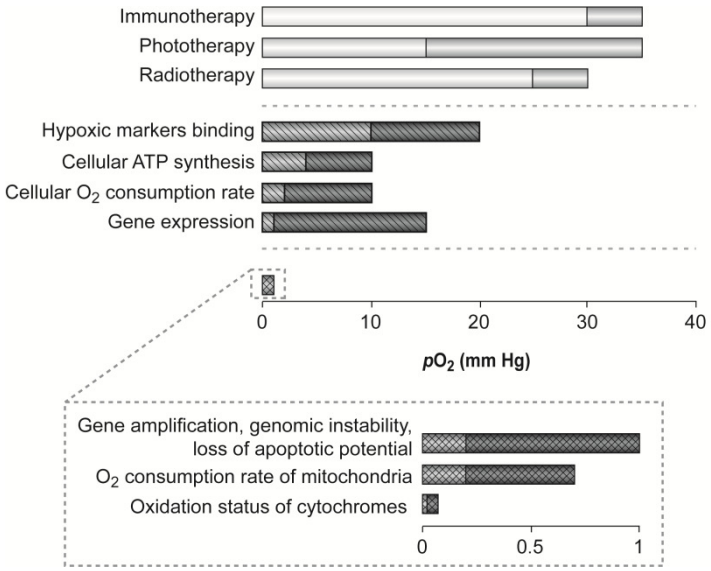

Figure 4. Sensitivity profiles to oxygen depletion (pO_2) in different therapies (☐), cellular functions (▨) and molecular mechanisms (▩).
Darker squares indicate pO_2 intervals eliciting an activity change. Above these levels, therapies are effective and cellular and molecular processes appear to proceed normally. Below these levels, therapies are not effective and the indicated cellular and molecular processes are discontinued.

To summarize, hypoxia is an important prognostic factor having different effects in normal and neoplastic cells, as well as on different cellular and metabolic processes. Beyond any molecular or physiological consideration, hypoxia is believed to induce a selective pressure in neoplastic cells, forcing their adaptation to a hostile environment characterized by oxygen and nutrient deprivation. This environmental pressure has been proposed as the driving force for the natural selection of resistant cells depicting a more malignant and metastatic phenotype (64,79).

1.2. Experimental approaches for the measurement of hypoxia

The implications of appropriate pO_2 measurements in the design of the most adequate therapy or combination of therapies, as well as for the understanding of basic biological events in tumors, are well illustrated in Table 2 and Figure 4. These important processes determine, in part, the requirements of the optimal measuring methodology. As heterogeneity is an important property of the hypoxic phenotype, its detection and resolution in space and time domains becomes, necessarily, a significant issue in the design of the most adequate imaging technology.

Table 3 summarizes the most relevant methodologies used to measure hypoxia, together with their characteristic features. The ideal properties of a hypoxia measurement technique include

noninvasiveness, adequate spatial and temporal resolution, quantitative measurement, no oxygen consumption, adequate range of pO_2 values measured and, if an exogenous agent is required, exhaustive knowledge of its toxicology and pharmacodynamic properties (121). Unfortunately, there is not currently an in vivo method that fulfills satisfactorily all these requirements.

For many years, oxygen electrodes were considered to be the 'gold standard' (133) in hypoxia measurements, supporting the development of several clinical studies (59,78,167). Recent reports, however, suggest that no universal gold standard exists at present (151,196). Nowadays, different methods to measure tissue oxygen levels in situ have been tested, such as O_2 electrodes (67,145,211), PET (56,158,212), single photon emission computed tomography (SPECT) (56,158), immunohistochemistry (114), near-infrared spectroscopy (NIR) (113,212) and phosphorescence (212). Among them, Magnetic Resonance (MR) presents several characteristics that make this technique particularly suitable for this purpose.

Table 3. Main characteristics of various techniques used to assess in vivo hypoxia.

Technique	Mechanism	Temporal resolution	Spatial resolution	Advantages	Disadvantages
O_2 electrodes	Polarographic current generated by the reduction of molecular oxygen	s	µm -mm	Direct measurement of O_2 concentration. Considered as "gold standard". Extensive literature	Invasiveness. Oxygen consuming. No imaging possible. Necrotic areas [a]
Fiber optic Oxy-Lite	Fluorescence quenching by dissolved O_2	s	µm-mm	Direct measurements of pO_2. No oxygen consumption. Simultaneous temperature measurement	Invasiveness. Short half life of probe Point measurement. No imaging possible
Immunohistochemistry (2-Nitroimidazole)	Fluorescence of drugs selectively trapped on hypoxic cells	h	µm	High spatial resolution Highly standardized Only viable hypoxic cells give signal	Non quantitative measurements Averaged hypoxic areas over sampled time Biopsy needed
^{19}F MRS/MRI Perfluorocarbons	Perfluorocarbons' relaxation properties	m	µm -mm	Imaging possible Non consuming oxygen Dynamic studies	Intratumoral injection Necrotic areas [a] Non clinical implementation of ^{19}F-MR
^{1}H MRS	Endogenous ^{1}H metabolites levels, lactate	m	mm-cm	Comprehensive Metabolomic information	Low spatial and temporal resolution Indirect, qualitative, pO2 detection through lactate resonance
^{31}P MRS	Endogenous phosphorilated metabolite levels, ATP, PCr, Pi	m	mm-cm	Comprehensive Bioenergetic information	Very low spatial and temporal resolution Indirect, qualitative, pO2 detection through, Pi, PCr or ATP changes
MRI BOLD	Magnetic susceptibility changes created by oxygenation/deosygenation of Hb	ms – s	Mm	Imaging at high spatial and temporal resolution. Non invasive. No Oxygen consumption	Many factors (blood flow, anemia, etc.) can affect the measurement.
MRI DCE	Dynamic transit of paramagnetic contrast agent	ms-s	mm	Non invasive. Multiple parameters determined:, blood volume, blood flow, mean transit time, capillary permeability	Limited spatial resolution. Strict instrumental requirements (EPI). Model dependent Indirect measurement pO_2
MRI-DWI	Apparent translational diffusion of tissue water	m	µm	Non invasive. High spatial resolution. Very sensitive to tissue anisotropic microstructure, cellularity and edema	Indirect measurement pO_2 High image processing demands (DTI) Multiexponential behaviour ADC
EPR	Variation in EPR resonance width	s – h	µm -mm	Non invasive. No Oxygen Consumption. Dynamic studies	Small range of pO_2 values covered Difficult clinical implementation
PET	PET labeled compounds selectively trapped in hypoxic cells	m – h	mm-cm	Non invasive. High sensitivity. Only viable hypoxic cells give signal	Radioactive compounds. Short half live Small range of pO_2 values covered Low spatial resolution

[a] Necrotic areas : no discriminating between living cells and necrotic tissue

1.2.1. Measurements of hypoxia by Magnetic Resonance Imaging

1.2.1.1. Perfluorocarbons (PFCs)

PFCs are organic molecules in which all hydrogen atoms have been replaced by fluorine atoms, hence providing a strong ^{19}F MR signal (129). PFC compounds were initially developed as artificial blood substitutes and oxygen carriers. However, PFCs display a series of properties that make them very appropriate to be used as MR contrast agents. In particular, they are biologically inert, exhibit minimal toxicity and are commercially available. There are different types of PFC: linear and cyclic. Figure 5a depicts the structures of some of the most commonly used PFCs in oxymetry.

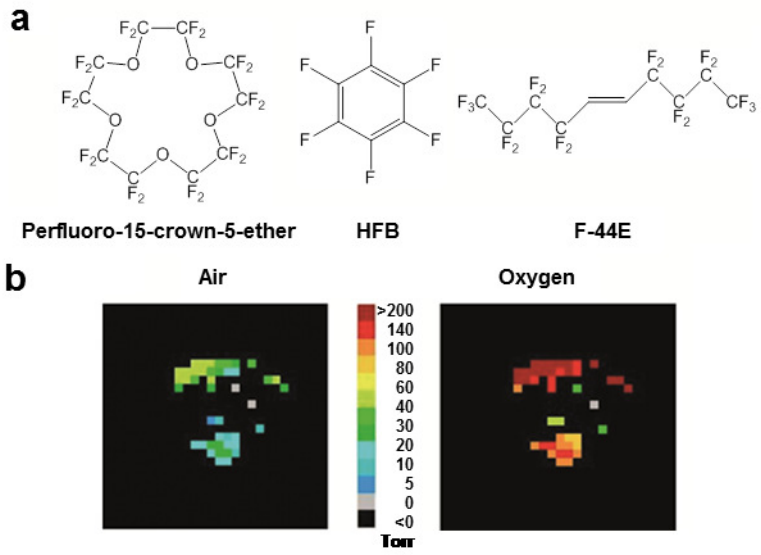

Figure 5. Perfluorocarbons as oximetry probes.
a) Different PFCs used in oximetry: perfluoro-15-crown-5-ether; hexafluorobenzene (HFB) and F-44E. b) Illustrative MRI oximetry of H460 human tumor xenograft (0.57 cm^3) implanted in a nude rat. Fluorocarbon relaxometry using echo planar imaging for dynamic oxygen mapping (FREDOM) was used to acquire pO_2 maps with an in-plane resolution of 1.25mm (5mm thick) in 6.5 min each while the rat breathed air (left) or oxygen (right).

To our knowledge, Parhami and Fung (159) were the first to show that a linear relationship exists between the ^{19}F MR spin-lattice relaxation rate ($R_1=1/T_1$) of PFC and oxygen tension, a circumstance most probably caused by the inherent paramagnetism of the oxygen molecule. Since then, many studies have exploited this phenomenon to measure pO_2 by ^{19}F MR. The same paramagnetic effect has been reported in other molecules, including water (98,110,229). However, in the latter case, many other factors, including metal ions, pH and temperature, also induce changes in water relaxivity in vivo, making the results observed more difficult to interpret exclusively in terms of pO_2 variations. In contrast, R_1 of PFCs is not usually affected by hydrophilic charged species (143) as these hydrophobic molecules do not mix with the surrounding aqueous phases, forming droplets or emulsions that preclude ions from entering the hydrophobic core (197). However, oxygen solubility is greater in PFCs than in water, and so these compounds may even be considered as molecular amplifiers of oxygen tension. Nevertheless, despite the differences in oxygen

solubility between PFCs and the surrounding medium, pO_2 between both phases will become the same after a short (usually seconds) equilibration interval (229). As a consequence, PFCs exhibit high sensitivity to oxygen changes and their detection. Furthermore, at a given magnetic field (B_0) and temperature (T), there is a linear relationship between R_1 and pO_2 of PFCs [$R_1 = a + b\ pO_2$, where *a* is the anoxic relaxation rate and *b* is the relaxation rate caused by the paramagnetic contribution of oxygen (99)]. With this equation, in vivo measurements of R_1 can be transformed easily into pO_2 maps using in vitro calibration curves (123). This method has been standardized by comparing the values obtained with PFCs with those obtained with electrodes (90,122), although discrepancies have also been found (174).

PFCs (pure or in emulsions) have been investigated for the measurement of tissue oxygenation in vivo (129,229). In particular, HFB (Figure 5a) has been used to investigate oxygenation and response to respiratory challenge of different tumor types using a number of different strategies. HFB presents several properties that make it especially suitable for this purpose (high R_1 sensitivity to pO_2, small temperature dependence and low toxicity (120)). Zhao et al. (87) developed a procedure called 'fluorocarbon relaxometry using echo planar imaging for dynamic oxygen mapping' (FREDOM), which enabled the imaging of the oxygen tension in vivo More recently, Jordan et al. (94) used a snapshot inversion recovery pulse sequence, allowing very fast HFB mapping (1.5 min) without sacrificing precision or spatial resolution. Representative pO_2 maps of H460 human non small cell lung carcinoma, implanted subcutaneously into nude rats, are shown in Figure 5b for animals breathing air (left) or oxygen (right) (156).

1.2.1.2. Proton probes analogous to PFC

The utilization of ^{19}F MR oximetry in clinical settings has been delayed, mainly because clinical scanners usually lack ^{19}F MR capability. Thus, the development of ^{1}H MR-based pO_2 probes could represent a critical advance for the routine measurement of tissue oxygenation and the optimization of therapeutic regimes under current clinical conditions.

Recently, Kodibagkar et al. (88) have proposed a proton analog to PFCs, hexamethyldisiloxane (HMDSO, Figure 6), as a novel ^{1}H MR oximetry probe. The HMDSO resonance is located close to 0 ppm, approximately 1 ppm below the methylene fat resonance but sufficiently far away to avoid interferences. HMDSO shares some important properties with PFCs: it is highly hydrophobic and nontoxic, shows high oxygen solubility, is biochemically inert in vivo, and is readily available and relatively inexpensive (91). HMDSO has long half-life (35 h) which may facilitate the study of chronic changes, reducing clearance from the tumor and improving the signal to noise during the measurement. Similarly, the short T_1 value may improve the temporal resolution, allowing faster pulsing rates and favoring the accumulation of R_1 data in hypoxic zones.

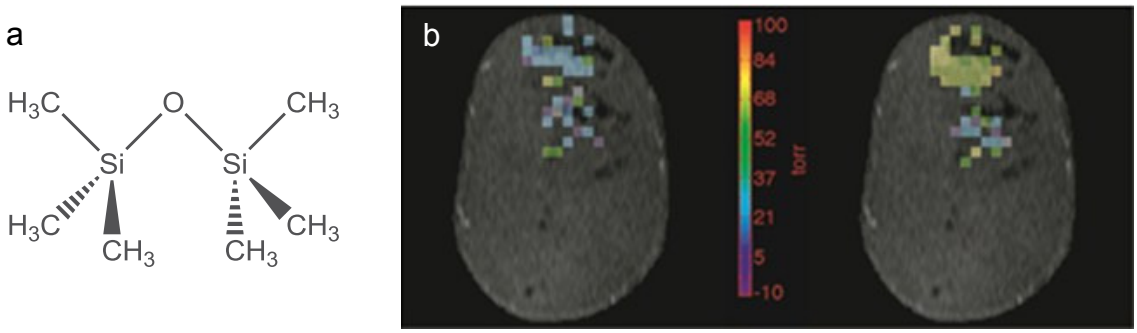

Figure 6. ^{1}H analogs to perfluorocarbons used as oximetry probes.
(a) Chemical structure of hexamethyldisiloxane (HMDSO). (b) Proton imaging of siloxanes to map tissue oxygenation levels (PISTOL), was used to acquire pO_2 maps with an in-plane resolution of 1.25mm (1mm thick) in 3.5 min while the rat breathed air (left) or oxygen (right). Maps are presented superimposed to a T1-weighted image of the tumor.

HMDSO also presents some disadvantages when compared with PFCs, mainly because of the strong background signal in ^{1}H MR, a circumstance not occurring in ^{19}F MR. Kodibagkar et al. (100) implemented, for this purpose, a method named Proton Imaging of Siloxanes to map Tissue Oxygenation Levels (PISTOL). This new approach has been validated by comparison with the well-established HFB-FREDOM approximation described above. Indeed, baseline and modifications in pO_2 values in tumors and thigh muscle are similar for both methods (100), as well as for those previously reported in the literature (88). One of the major advantages of the HMDSO method is that translation to the clinic may be possible in the near future allowing the combination of oximetry information with that derived from other routinely used ^{1}H MR-based methods, such as dynamic contrast enhancement (DCE), translational diffusion measurements and magnetic resonance spectroscopy (MRS).

1.2.1.3. Blood Oxygen Level Dependent (BOLD) contrast

BOLD contrast can be used as a functional MRI technique that affords a measurement of blood oxygenation by using sequences sensitive to changes in T_2*. The method is based on the fact that deoxyhemoglobin is paramagnetic, whereas oxyhemoglobin is diamagnetic. Therefore, changes in deoxyhemoglobin/oxyhemoglobin ratio related to variations in oxygen concentration in blood, will influence the relaxation of water protons (particularly T_2*), enabling blood oxygenation levels to be measured by MRI. Originally, the BOLD approach was developed to investigate cerebral activity, being extended more recently to the assessment of tumor oxygenation in response to hyperoxic gas challenge (141,158). Early BOLD MRI investigation in tumors were performed by Karczmar et al. (93) using 100% O_2 in a R3230AC mammary adenocarcinoma model, followed by the work of Robinson et al. (173) using carbogen in a GH3 prolactinoma model. They both found changes in BOLD signal intensities as large as 50% and 100%, respectively. Several studies have shown that changes in signal intensities of T_2* weighted (T_2*W) images and T_2* values reflect changes in tumor oxygenation, and they have potential value as prognostic

indicators (176). However, a quantitative relationship between the BOLD effect and pO_2 has not been found (15), probably because of the complex relationship between these two parameters (89). Indeed, in addition to oxygenation, the BOLD effect is influenced by other factors different from pO_2, including blood flow, hemoglobin levels, vasculature, etc. These circumstances prompted the use of the acronym 'FLOOD' (flow and oxygenation dependent) to refer to the BOLD experiment as applied to the study of oxygenation in tumors (83).

1.2.1.4. Tissue oxygen level dependent (TOLD) contrast

Recently, tissue oxygenation has been proposed to be measured using the paramagnetic nature of oxygen and the shortening of the tissue water T_1 value during hyperoxic gas breathing (125). Indeed, molecular oxygen has two unpaired electrons and may act as a paramagnetic contrast agent, shortening the water T_1 value, thus reflecting tissue oxygenation rather than blood oxygenation.

A number of clinical studies have been performed to assess the variations in R_1 and R_2* in response to carbogen or pure oxygen breathing in different organs (spleen, liver, renal cortex) and normal tissues (muscle, subcutaneous fat) (146,147). Significant increases in R_1 were found in all cases, whereas R_2* only showed significant changes with carbogen, but not under pure oxygen breathing. The magnitude of these responses was found to be organ and tissue dependent. Changes in tumor's R_1 values in response to hyperoxic gas breathing were clinically assayed in various types of cancer (ovarian adenocarcinoma, colon carcinoma, cervix squamous carcinoma) (148). The results were compared with those obtained with DCE MRI, finding regions of positive correlation (high or low perfusion corresponding to good or bad oxygenation) and also zones of mismatch (areas of moderate perfusion and low oxygenation). The quantitative relationship of these variations with changes in pO_2 merits, however, further investigation.

1.2.2. Measurement of hypoxia by MRS

Both ^{1}H and ^{31}P MRS in vivo spectra have provided only an indirect assessment of the tissue oxygen tension with limited resolution (millimeters in animal scanners and centimeters in currently available clinical human scanners). Oxygen limitations in tumors typically lead to increases in the lactate and total choline resonances detected by ^{1}H MRS (107) or increases in the phosphomonoester peak and inorganic phosphate/phosphocreatine (Pi/PCr) ratios observed by ^{31}P MRS (30,111,142). Thus, it would become considerably useful to introduce an external agent, directly sensitive to hypoxia, detectable by MRS.

1.2.2.1. Nitroimidazoles

Nitroimidazolyl derivatives have been used extensively in South America since the 1970s as therapeutic agents against *Trypanosome Cruzi*, the protozoan causing Chagas' disease. Since then, these compounds have found several applications, including antibacterial and antiprotozoal drugs (nifurtimox, metronidazole)

(44), cytotoxic molecules against hypoxic cells (95,218), radiosensitizers and chemopotentiation drugs in adjuvant therapies (44,218) and, more recently, hypoxia markers using ^{19}F MR (95), PET (56,86,102,103), SPECT (86) and immunohistochemistry (20).

To our knowledge, Varghese et al. (200) were first to report that ^{14}C-labeled misonidazole (^{14}C-MISO) was selectively trapped in hypoxic cells. Subsequent studies associated this with the enzymatic reduction of the nitro group (218). The most widely accepted metabolism of nitroimidazole derivatives under aerobic and anaerobic conditions is briefly summarized in Scheme 1. In both cases, the reaction begins with transformation of the parental compound into an anion radical through the addition of one electron by the nitro group. Under aerobic conditions, the anion reacts with molecular oxygen, producing a superoxide anion and the original compound, producing a futile cycle. The superoxide anion is transformed by superoxide dismutase (SOD) to hydrogen peroxide, leading to a series of reactive oxygen species responsible for nitroimidazole toxicity in normal, i.e. aerobic, tissue (26). Otherwise, under hypoxic conditions, the anion radical can be further reduced by nitroreductases into a nitroso derivative. Additional reductions will transform the nitroso metabolite subsequently into hydroxylamine and finally in amine derivatives. These bind easily to cellular components, forming covalent bonds with sulfhydryl groups (such as those of reduced glutathione), thus becoming selectively trapped in hypoxic cells since binding to normoxic cells does not occur to the same extent. The chemical reduction of hydroxylamine derivatives and the subsequent chemical transformations have been extensively investigated in vitro, but few clues exist into the mechanisms operating in vivo (23,203).

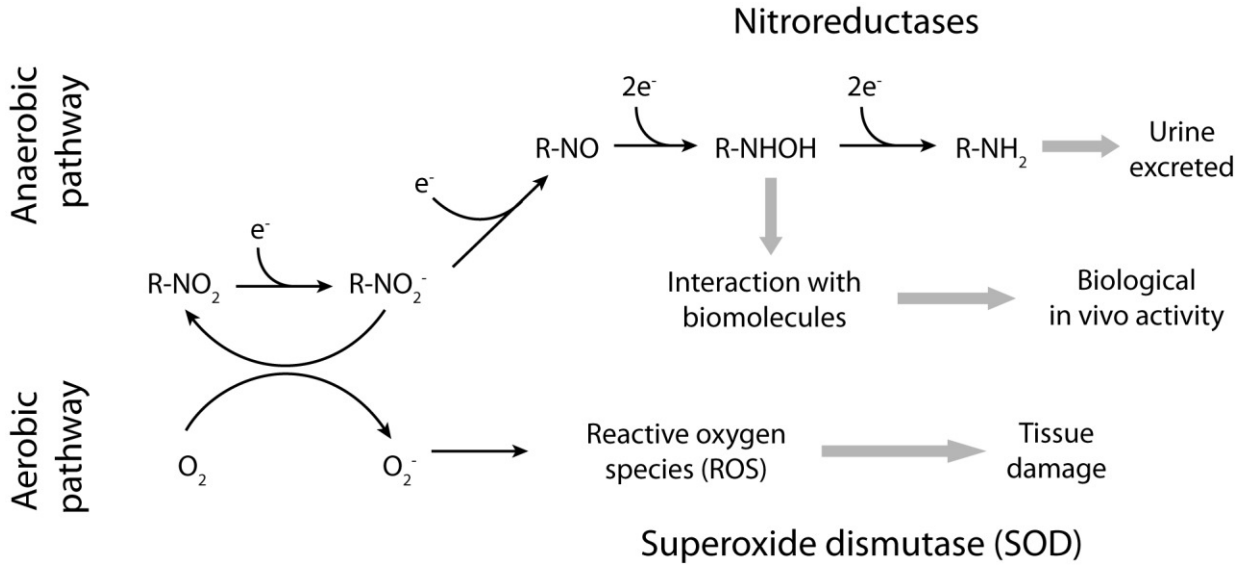

Scheme 1. Bioreductive transformations of nitroimidazole derivatives under anaerobic or aerobic conditions in vivo.

Notably, an important consequence of its in vivo metabolism is that nitroimidazole-based methods only account for viable hypoxic cells, i.e. those able to reduce the nitro moiety, in contrast with other techniques

that measure directly the pO_2. It is important to note that direct relationships between oxygen concentration and nitroimidazole reduction have been reported previously both in vitro (3,91) and in vivo (116). Nitroimidazole markers of hypoxia are normally used in combination with different detection techniques, such as MRS, MRI, PET (F-MISO and copper diacetyl-bis-N(4)-methylthiosemicarbazone (Cu-ATSM)) (114,158), SPECT (iodinated azomycin arabinoside) (41) and immunohistochemistry (Pimonidazole and EF5) (51,97), thus adding the advantages and disadvantages of the detection method employed to those of the corresponding biomarker molecule.

The interpretation of the results from hypoxia measurements using nitroimidazole-based drugs remains complex as it involves three simultaneous processes with their characteristic rate constants (128): (i) marker bioreduction and binding in hypoxic cells; (ii) excretion of the marker (and eventually its products); and (iii) if radioisotopes are used, their lifetimes. Accordingly, the amount of nitroimidazole derivative observed depends on how well it has reached and left the target tissue, as well as on the O_2 concentration in the tissue, which determines, together with the redox properties of the compound, the amount of probe that remains trapped within the cellular structures. The first aspect depends on the blood flow, microvascular perfusion and marker lipophilicity, while the second one depends on the intrinsic redox properties of the nitroimidazole and the local oxygen tension. If the nitroimidazole derivative is labeled with short-lived radioisotopes, the signal intensity will also decrease with time because of radioactive decay. The balance of these different processes determines the optimal time point to be used in the measurement.

A significant limitation is that nitroimidazole-based markers often target highly hypoxic cells, such as those with pO_2 below 1 mmHg. Cells with higher oxygen concentrations, but still hypoxic, may not be detected, and some studies have shown that these cells with intermediate hypoxia levels are also important in tumor development and treatment failure (220).

Attempts have been made to design rationally an optimized nitroimidazole molecule fulfilling all desired properties focusing on modifying lipophilicity, reduction potential and reactivity. To this end, the structure for most nitroimidazole-based hypoxia markers may be divided into two parts: the nitro moiety and the lateral chain. The former is linked to an aromatic ring (often imidazole) and is responsible for electron affinity, i.e. bioreduction, as defined by the reduction potential. The lateral chain is responsible for biodistribution, tissue penetration, elimination rate, etc. (185), carrying, in most cases, the 'reporter atom' (^{19}F, ^{18}F, $^{125/123}I$, ^{99m}Tc). Thus, the general properties of these molecules may be fine tuned for specific purposes by modifying appropriately either the imidazole ring or the lateral chain. The improvements to be achieved may include a more adequate partition coefficient, adequate solubility in aqueous medium, stability, more feasible synthesis, improved lipophilicity, etc. The most common nitroimidazole derivatives used as hypoxia markers are shown in Figure 7.

Several studies have been performed to compare the measurements obtained with nitroimidazole-based markers and other techniques with different results. Some reported a direct relationship between pO_2 measured by EPR and nitroimidazole retention (116). On the other hand, others found no correlation comparing results obtained with nitroimidazole derivative markers and Eppendorf electrodes or ^{19}F MR methods (5,51,174). A possible explanation is that all of these techniques do not discriminate between necrotic or living tissues, whereas nitromidazoles bind exclusively to living cells. Another source of discrepancy is related to the different measurement times, as indicated in Table 3. Whereas polarographic electrodes or PFC-based measurements provide pO_2 measurements limited to a single time point, nitroimidazole-based markers measure hypoxia through adducts accumulated in the hypoxic cell or tissue during the incubation time, thus hindering an appropriate direct comparison.

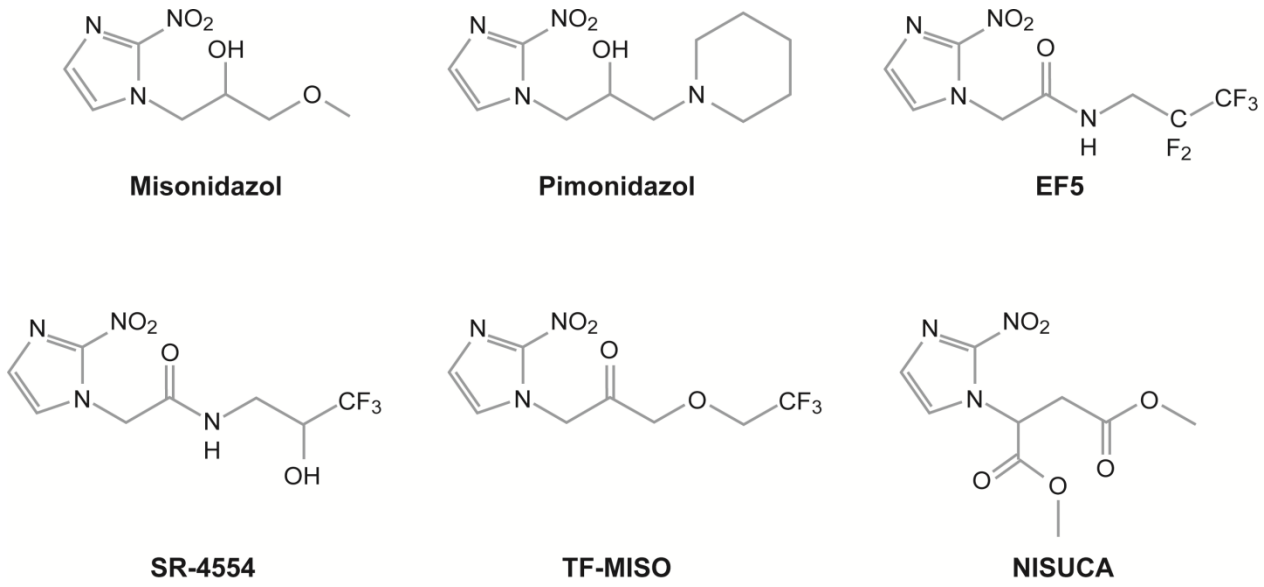

Figure 7. Nitroimidazole derivatives currently used as molecular probes for hypoxia.
Misonidazole (MISO) derivatives with ^{18}F are used as positron emission tomography (PET) probes. Pimonidazole is used as an histochemical probe. EF5, SR-4554 and TF-MISO are ^{19}F MR indicators. NISUCA is a novel ^{1}H MRS probe developed and implemented in this thesis (155).

A variety of approaches have been implemented using nitroimidazole based drugs as ^{19}F MR oximetry probes. Early work carried out by Raleigh et al. (170) using CCI-103F showed the *ex vivo* detectability of bound derivatives in tumor and liver by ^{19}F MR. Soon after, the in vivo implementation of CCI-103F and Ro 07-0741 were reported (127) and the ex vivo concentration of bounded markers in subcutaneous tumors (R3327 H NS R3327 AT prostatic adenocarcinomas and walker 256 carcinoma) or in liver were quantified using ^{19}F MR (171).

More recently, two fluorinated nitroimidazole derivatives, SR-4554 and TF-MISO (Figure 7), have been used to measure hypoxia in vivo. The former has been studied extensively both in vitro (3) and in vivo with different tumor types (4), showing low toxicity, high metabolic stability, favorable pharmacokinetics and

high sensitivity for detection by MRS (2). Authors used a new parameter, named the ^{19}F retention index (^{19}F RI), indicative of tumor hypoxic fraction. This variable was defined as the ratio of the SR-4554 signal intensity, measured by ^{19}F MRS, 45 min and 6 h after injection of the marker (4). It is assumed that the signal at 45 min reflects the total parent compound, whereas the signal at 6 h detects the reduced, and therefore retained, compound. This index shows a good correlation with previously reported radiobiological hypoxic fractions of four murine tumors (EMT6, SCCVII, KHT and RIF-1) (4). A close relationship of ^{19}F RI and polarographic electrode measurements in rats bearing P22 carcinosarcoma has been reported (183). On these grounds, SR-4554 entered recent Phase I clinical trials (184). The pharmacokinetic and toxicity profiles appear to be favorable for use as a hypoxia marker. More recently, a mean retention index of 13.6 in human neoplasms has been reported, compared to the retention index of 4.1 found in plasma samples obtained simultaneously with the spectroscopic measurement, revealing the presence of hypoxia in those tumors (108).

Procissi et al. (169) proposed 2-Nitro-α-[(2,2,2-trifluoroethoxy)methyl]-imidazole-1-ethanol (TF-MISO) as a plausible ^{19}F MR nitroimidazole-based reporter. They observed that cellular drug uptake increased with concentration and the time of incubation in anoxic conditions (compared to normoxia). The TF-MISO resonance linewidth increased with time after injection in murine tumors and T_1 in vivo became much shorter than in a phantom. These spectral changes were proposed to reveal the presence of the bound adduct produced during the hypoxic challenge in vivo. A positive correlation was found in vivo between the corresponding retention index and the tumor volume (qualitatively related to tumor hypoxia). Finally, multivoxel spectroscopy has been achieved in tumors in vivo, showing that TF-MISO is visible under these conditions. Based on spectroscopic measurements, pharmacokinetic parameters and a biexponential model, the authors calculated the hypoxic fraction of the tumor and compared the results with literature values, finding similar results in MCa tumors. Although this methodology is far from being clinically applicable, it represents an important advance, as it proves for the first time, that a nitroimidazole-based drug may be spatially resolved by multivoxel spectroscopy in vivo.

1.2.3. Measurement of hypoxia by EPR

Molecular oxygen is paramagnetic, making EPR a theoretically optimal technique for direct, sensitive and noninvasive tissue oximetry. Unfortunately, the direct detection of dissolved oxygen in fluids is not possible because of the large broadening of its spectral lines. Therefore, indirect methods had to be developed. These methods rely on the administration of a paramagnetic probe, the EPR properties of which are altered by the surrounding paramagnetic oxygen, most commonly through the modification of its electron relaxation processes. The most frequently implemented method uses oxygen-induced T_2 shortening and concomitant broadening of the principal hyperfine line of the EPR spectra from the probe. Optimal paramagnetic probes useful for EPR oximetry should have few, narrow EPR lines, good stability in biological

media, no toxicity and a linear dependence of R_2 on oxygen concentration. Indeed, a direct relationship between the linewidth and percentage oxygen concentration can be found in vitro, and this calibration curve is used for in vivo determinations (94).

There are two classes of paramagnetic probe currently used for in vivo oximetry: water-soluble and insoluble. The former include mainly the nitroxides and triaryl methyl radicals. The latter comprise lithium phthalocyanine and lithium naphthalocyanine (57). Because most stable molecules have all their electrons paired, the EPR approach is less extended than MR methods. However, this limitation provides the EPR technique with large specificity. Particularly, insoluble paramagnetic materials, once implanted, provide noninvasively repeated and accurate measurements of pO_2 at the same site. Currently, considerable efforts are being dedicated to develop clinical applications for EPR oximetry. However, some issues still need to be overcome in order to convert it into a routine modality for the assessment of tissue oxygenation. These include, among others, safety and patient comfort for clinical studies and gaining of a consensus on the quantitative value of the measurements (194), In addition, EPR imaging technology has been developed and used to map oxygenation in vivo (212).

2. OBJECTIVES

The main objective of this thesis is to develop and implement new methodologies to assess tumor hypoxia in vivo using MR methods. Two main approaches were developed here for this purpose; 1) Use of exogenous contrast agents and 2) Use of endogenous tissue contrast.

1. Use of exogenous contrast agents

To develop and implement the use of classical and novel nitroimidazole derivatives as ^{1}H MRS contrast agents responsive to hypoxia.

a. To investigate the reduction mechanism of Nitroimidazole derivatives in cell-free systems and disclose the main determinants governing their bioreduction.
b. To investigate the reduction rate of these 2-nitroimidazolil probes and the influence of the different effectors conditioning it in cultures of C6 glioblastoma cells.
c. To investigate the possibility of implementing in vivo this approach using implanted C6 glioblastoma tumors, the oxigenation status of which is manipulated by modifying the oxygen content of the gas breathed by the animals and to examine the possibility to obtain hypoxia maps using this technology.

2. Use of endogenous tissue contrast

To combine BOLD and TOLD measurements to assess the response of tumoral pO_2 to carbogen breathing based on differences in signal intensity in T_1- and T_2*-weighted images.

a. To test this method using two rat prostate tumor types, noted for differential growth rates, vascular development and oxygenation.
b. To assess the origin of the observed changes in T_1- and T_2*- weighted images by analyzing changes in tumoral relaxation rates (R_1 and R_2*) in response to carbogen breathing.

3. MATERIALS & METHODS

3.1. Synthesis and characterization of Imidazole Derivatives

3.1.1. Analytical determinations

Melting points were obtained on a microscope hot stage and are uncorrected. Elemental analyses were performed with Perkin-Elmer 240 apparatus. Mass Spectroscopy was carried out in a GC/MS Schimadzu QP-5000 equipment at 70 eV. For HRMS data, VG AutoSpec instrument was used. IR spectra were performed on a Philips PU-9700 and a Bruker vector 22 spectrophotometers. MR acquisitions were recorded with a Bruker DRX-400 (9.4 T). ^{1}H and ^{13}C chemical shifts (δ) in $CDCl_3$ are given from internal TMS and in D_2O from internal TSP. ^{13}C chemical shifts in D_2O are given from external DMSO-*d*6 with an accuracy of ± 0.01 for ^{1}H and ± 0.1 ppm for ^{13}C. The residual water signal in ^{1}H MR spectra in D_2O solution was suppressed when necessary using a 1 s (low power, 0.5 W) presaturating pulse applied with the decoupler. ^{1}H–^{1}H coupling constants (*J*) are accurate to ±0.2 Hz for ^{1}H MR spectra. Thin Layer Chromatography was performed on DC-Aulofolien/Kieselgel 60 F245 (Merck) and column chromatography through silica gel Merck 60 (230–400 mesh). D_2O (99.9 % D) was purchased from Apollo Scientific (Stockport, Great Britain). The rest of the products and anhydrous solvents were obtained from Aldrich of the highest purity available.

Cyclic voltammetry measurements were carried out using an ECO Chemie Autolab PGSTAT 12 potentiostat using the software package GPES 4.7 (General Purpose Electrochemical System). A Metrohm 6.0805.010 conventional glassy carbon electrode (3 mm o.d.) as the working electrode, a BAS MF-2063 Ag/AgCl/3 M KCl as the reference electrode and auxiliary electrode consisting of a Pt wire, which were directly immersed in the solution. A 10-mL electrochemical cell from BAS (model VC-2) was also used. $E_{1/2}$ values were taken as the average of the anodic and cathodic peak potentials. The scan rate used was 100 mV s^{-1}.

3.1.2. Synthesis of NISUCA

The preparation of NISUCA and its precursors is illustrated in Scheme 2 (155).

*Dimethyl 2-Nitro-1H-imidazol-1-ylbut-2-enedioates **2** and **3.***

A solution of dimethyl acetylenedicarboxylate (1.1 eq.) and 2-nitroimidazole (1 eq.) in MeCN (40 mL) was stirred at 65 °C for 3 days. After cooling to room temperature, the mixture was filtered and the solvent was evaporated in vacuo. Purification of the residual oil by column chromatography (silica gel, CH_2Cl_2–EtOH, 100:0 to 95:5) allowed the separation of the isomers **2** and **3**.

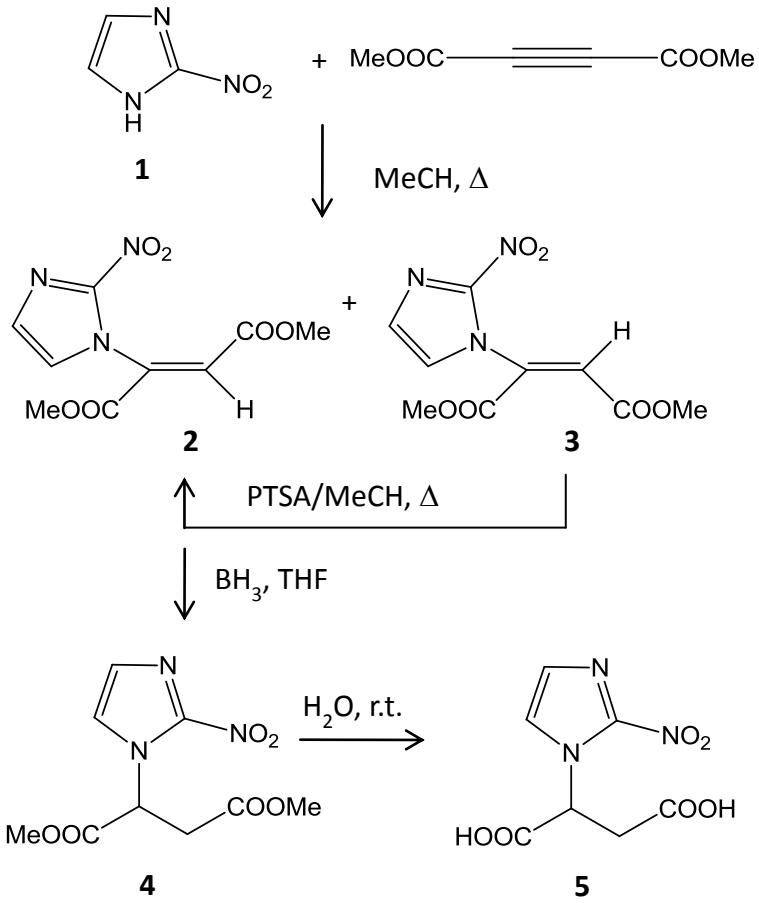

Scheme 2. Synthesis of NISUCA by termal addition of 2-nitroimidazole to dimethyl acetylenedicarboxylate.

Dimethyl (Z)-2-(2-Nitro-1H-imidazol-1-yl)but-2-enedioate (**2**)

White solid; yield: 61 %; mp 106–108 °C (EtOAc). IR (ATR): 1733, 1717 cm^{-1}. ^{1}H MRS (400 MHz, $CDCl_3$): δ = 7.27 (d, J = 1.2 Hz, 1 H), 7.16 (s, 1 H), 7.06 (d, J = 1.2 Hz, 1 H), 3.86 (s, 3 H), 3.70 (s, 3 H). ^{13}C MRS (100 MHz, $CDCl_3$): δ = 162.1, 161.2, 135.8, 129.0, 126.1, 125.6, 53.9, 52.7. Anal. calculated for $C_9H_9N_3O_6$: C, 42.33; H, 3.52; N, 16.46; found: C, 41.97; H, 3.50; N, 16.31.

Dimethyl (E)-2-(2-Nitro-1H-imidazol-1-yl)but-2-enedioate (**3**)

Yellow oil; yield: 17 %. IR (ATR): 1732, 1537 cm^{-1}. ^{1}H MRS (400 MHz, $CDCl_3$): δ = 7.20 (d, J = 1.2 Hz, 1 H), 7.09 (d, J = 1.2 Hz, 1 H), 6.52 (s, 1 H), 3.85 (s, 3 H), 3.74 (s, 3 H). ^{13}C MRS (100 MHz, $CDCl_3$): δ = 163.2, 160.2, 133.3, 129.3, 127.7, 126.1, 53.5, 52.9. HRMS (EI): m/z [M^+ – 31 (OMe)]. HRMS calculated for $C_8H_6N_3O_5$: 224.0307; found: 224.0304.

Isomerization of E-isomer **3** to Z-isomer **2**

A solution of compound **3** (1 eq.) and p-toluenesulfonic acid (0.33 eq.) in MeCN was heated at 80 °C for 48 h. After cooling the solvent was evaporated in vacuo and the reaction crude was purified by

column chromatography (silica gel, CH_2Cl_2–EtOH, 100:0 to 80:20) to give the corresponding compound.

Preparation of dimethyl 2-(2-Nitro-1H-imidazol-1-yl)succinate (**4**) NISUCA

To a solution of **2** (1 eq.) in anhydrous THF at 0 °C was added dropwise 1 M BH_3·THF (1.15 eq.). The mixture was stirred under N_2 for 1 h and kept at 10 °C for 8 h. Subsequently, the crude mixture was hydrolyzed in acidic medium (10 % HCl) at 0 °C and extracted with EtOAc. The combined organic layers were dried (Na_2SO_4) and the solvent was evaporated in vacuo. The residual oil was purified by column chromatography (silica gel, CH_2Cl_2–EtOH, 100:0 to 80:20).

Yellow oil; yield: 80 %. IR (ATR): 1737 cm^{-1}. ^{1}H MRS (400 MHz, $CDCl_3$): δ = 7.27 (d, J = 1.2 Hz, 1 H), 7.16 (d, J = 1.2 Hz, 1 H), 5.90 (dd, J = 8.8, 4.4 Hz, 1 H), 3.77 (s, 3 H), 3.69 (s, 3 H), 3.31 (m, 2 H). ^{13}C MRS (100 MHz, $CDCl_3$): δ = 169.8, 167.1, 128.3, 126.1, 58.2, 53.4, 52.4, 36.4. HRMS (EI): m/z [M^+ – 46]. HRMS calculated for $C_9H_{11}N_2O_4$: 211.0719; found: 211.0714.

(±)-2-(2-Nitro-1H-imidazol-1-yl)succinic Acid (**5**)

A solution of ester **4** (150 mg, 0.58 mmol) in distilled H_2O was stirred at room temperature for 30 d. The solvent was concentrated in vacuo and the hygroscopic residue was dried under reduced pressure (16 mbar) to give **5** as a white solid.

Yield: 53 mg (40 %). ^{1}H MRS (400 MHz, D_2O): δ = 6.47 (d, J = 2.8 Hz, 1 H), 6.42 (d, J = 2.8 Hz, 1 H), 4.98 (dd, J = 8.8, 5.4 Hz, 1 H), 3.04 (2 m, 2 H)

3.1.3. Synthesis of NIMAC

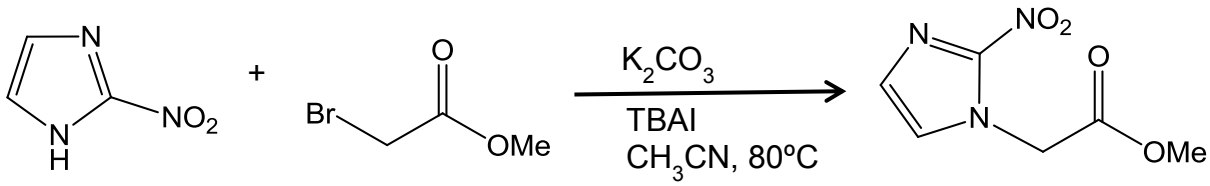

The preparation of NIMAC is illustrated in Scheme 3:

Scheme 3. Synthesis of NIMAC by addition of 2-nitroimidazole to methyl bromoacetate.

*Methyl 2-(2-nitro-1H-imidazol-1-yl)acetate (**6**) NIMAC*

2-Nitroimidazole **1** (1 eq.) was added to a mixture of methyl bromoacetate (1 eq.), potassium carbonate (1.5 eq.), and TBAI (0.02 eq.) in acetonitrile. The mixture was heated to 80 ºC and stirred vigorously at this temperature for 40 min. After cooling to room temperature, the inorganic salts were removed by vacuum filtration and washed with acetonitrile. The filtrate and washings were

1 **6**

combined and the solvents were evaporated in vacuo to give a residue that was recrystallized from ethyl acetate to yield methyl 2-(2-nitro-1H-imidazol-1-yl)acetate **6** (161).

Yield: 80%. Mp, 95-96 °C. ^{1}H MRS (400 MHz, D_2O): δ = 7.11 (s, 1H), 7.05 (s, 1H), 5.09 (s, 2H), 3.77 (s, 3H).

3.2. Kinetics of the enzymatic reduction of nitromidazoles in vitro as detected by ^{1}H MRS.

3.2.1. Experimental Design

We investigated by high resolution ^{1}H MRS the kinetics of reduction of nitromidazole derivatives in vitro using cell free systems in the presence and absence of either NADPH:cytochrome P450 reductase (P450ase, E.C. 1.6.2.4) or glutathione reductase (GR, E.C. 1.8.1.7). Basically we monitored the kinetics of reduction of NISUCA, NIMAC, Misonidazole and Pimonidazole under different oxygen tensions, reactant and product concentrations and the in the presence or absence of either or both of the enzymes involved. We performed three types of experiments. First, we investigated the stability of reactants and products and the potential contribution of non enzymatic transformations during the reaction time by performing a series of incubations with cocktails containing individual substrates or products or mixtures of them, in the presence and absence of P450ase (Table 4). Second, we performed time course studies following the progress of the reaction under different substrates and effectors concentrations. Finally, we determined the apparent K_m (K_m') and apparent V_{max} (V_{max}') values to be able to interpret easier the events occurring in vivo. The following general red-ox reaction was investigated:

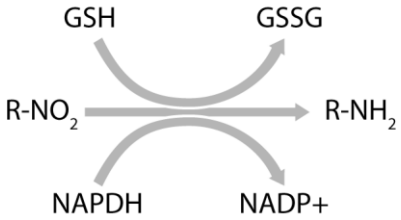

Table 4 summarizes the incubation conditions employed to assess the stability and relative contribution of the different reactants and products to the overall process, using Misonidazole as a representative molecule. We performed these experiments in the presence and absence of P450ase, to assess the potential contribution of enzyme catalyzed and uncatalyzed processes. In these measurements we monitored the corresponding resonance intensities (Table 5) during 24h. We used reaction mixtures containing phosphate buffer (75 mM, pH= 7.7, 37 °C, 10% D_2O), nitroimidazole derivative (5 mM), NADPH or $NADP^+$ (15 mM), GSH (10 mM) or GSSG (5 mM) and P450ase (0.2 U/ml) where appropriate.

Table 4. Stability of substrates and products involved in misonidazole reduction, in the presence and absence of P450ase.

Incubation Condition	NADPH 15 mM	$NADP^+$ 15 mM	GSH 10 mM	GSSG 5 mM	MISO 5 mM	P450ase 0.2 U/mL	Information obtained
1a	+	-	-	-	+	+	Stability of NADPH
1b	+	-	-	-	+	-	
2a	-	+	-	-	+	+	Stability of NADP
2b	-	+	-	-	+	-	
3a	-	-	+	-	+	+	Stability of GSH
3b	-	-	+	-	+	-	
4a	-	-	-	+	+	+	Stability of GSSG
4b	-	-	-	+	+	-	
5a	+	-	+	-	+	+	Stability of GSH in the presence of NADPH
5b	+	-	+	-	+	-	
6a	+	-	-	+	+	+	Stability of GSSG in the presence of NADPH
6b	+	-	-	+	+	-	
7a	-	+	+	-	+	+	Stability of GSH in the presence of NADP
7b	-	+	+	-	+	-	
8a	-	+	-	+	+	+	Stability of GSSG in the presence of NADPH
8b	-	+	-	+	+	-	

+ indicates presence of the corresponding reagent or product at the specified concentration
- indicates the absence of the corresponding reactant or product.

Table 5. ^{1}H chemical shifts and coupling constants of relevant protons from reactants and products involved in nitroimidazole reduction relevant to the kinetic analysis.

	Chemical Shift (ppm)	
Compound [a]	Ha [b]	Hb [b]
NISUCA	7.64 (d, J= 1.2 Hz, 1 H) [res #N1]	7.29 (d, J= 1.2 Hz, 1 H) [res #N2]
MISO analog	7.48 (d, J=0.9 Hz, 1 H) [res #M1]	7.22 (d, J=0.9 Hz, 1 H) [res #M2]
Pimonidazole	7.50 (d, J=1.1 Hz, 1 H) [res #P1]	7.24 (d, J=1.1 Hz, 1 H) [res #P2]
NIMAC	7.50 (d, J=1.2 Hz, 1 H) [res #NM1]	7.28 (d, J=1.2 Hz, 1 H) [res #NM2]
GSH	3.13-2.80 (m, 2 H) [res #GSH1] Cysteine, C β	3.78 (t, J=6.3 Hz, 1 H) [res #GSH2] Glutamic, C α
GSSG	3.47-2.73 (m, 4 H) [res #GSSG1] Cysteine, C β	3.78 (t, J=6.3 Hz, 2 H) [res #GSSG2] Glutamate, C α
NADPH [b]	6.95 (s, 1 H) [res #NADPH1] Nicotinamadie, N2	6.00 (dd, J= 8.2, 1.3 Hz, 1 H) [res #NADPH2] Nicotinamide, N6
NADP+ [b]	8.415 (s, 1 H) [res #NADP+1] Adenosine, A8	6.06 (d, J=5.5 Hz, 1 H) [res #NADP+2] Nicotinamide, N1'

[a] See Figure 8 for chemical structures and numbering
[b] Resonance numbers in square brackets are those indicated in the spectra of Figures 10, 12, 14 and 16.

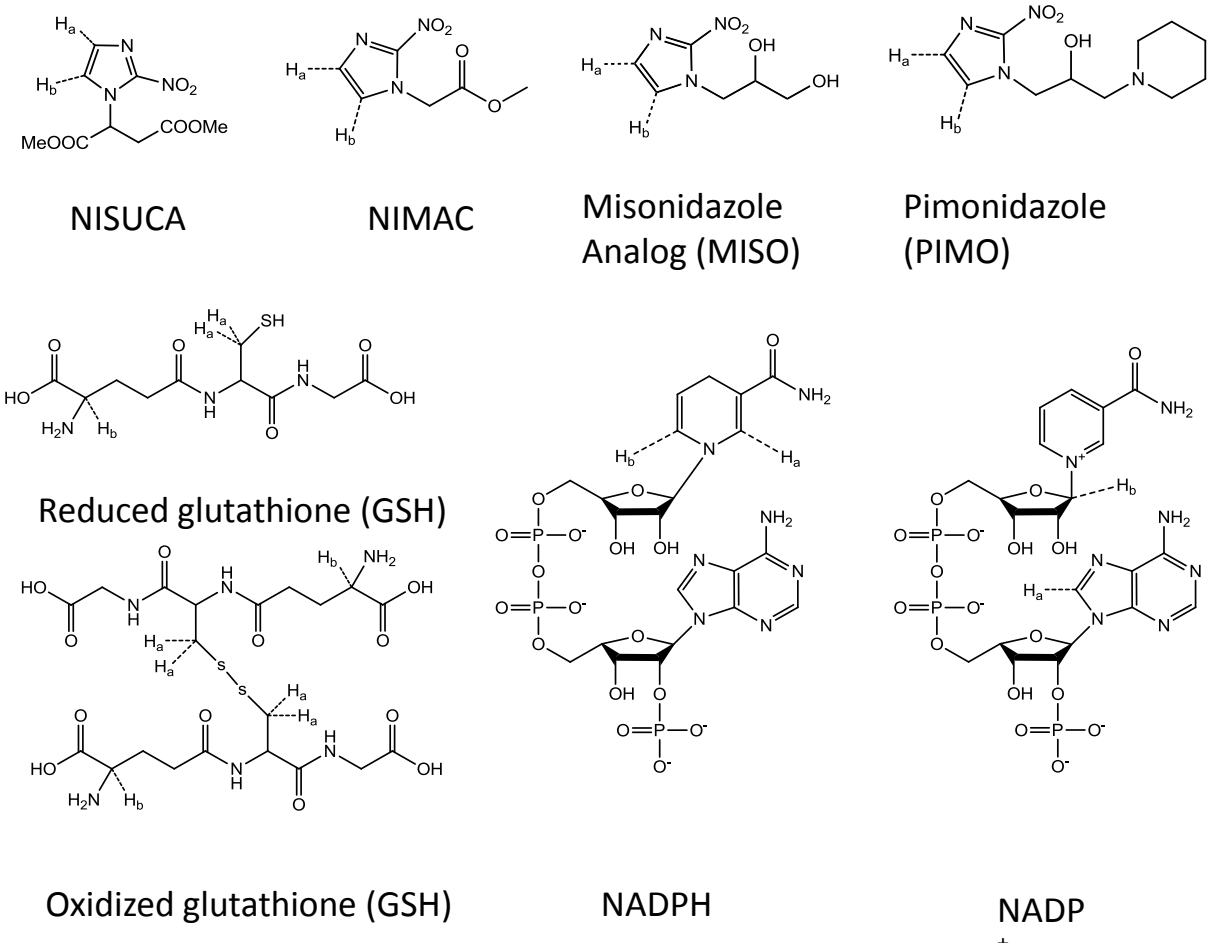

Figure 8. Chemical structures of reactants and products and the corresponding specific protons used to follow the kinetics of nitroimidazole reduction.
Chemical shifts and homonuclear coupling constants are those of Table 5.

We performed time course experiments to investigate the evolution of reactants and products using phosphate buffered (75 mM, pH= 7.7, 37 ^{o}C, 10 % D_2O) reaction mixtures containing the different hypoxia markers (5 mM), NADPH (15 mM), reduced glutathione (10 mM), P450ase (0.2 U/ml) and glutathione reductase (0.4 U/ml) where indicated.

The impact of the initial hypoxia marker concentration in the reduction rate was evaluated by using different initial concentrations of MISO and NIMAC, varying between 1 to 20 mM. Samples were composed of phosphate buffer (75 mM, pH= 7.7, 37 ^{o}C, 10 % D_2O), NADPH (15 mM), GSH (10 mM) and P-450ase (0.2 U/ml) and were treated as previously described, both in normoxic and anoxic conditions. Reaction was followed during two hours after the enzyme addition. A similar cohort of experiments was performed to obtain insight into the role of GSH in the reduction rate. In this case, samples were prepared analogously to the aforementioned conditions with the hypoxia marker concentration maintained at 5 mM and the GSH concentration varied in a 0- 20 mM range.

3.2.2. High Resolution ^{1}H MRS

All reaction cocktails were prepared in 5 mm MR tubes (WILMAD, NJ, US) using TSP (1 mM) as internal reference and the tubes placed in 11.7T (500.13 MHz) Bruker AVANCE wide-bore (9.9 cm bore) spectrometer for high resolution ^{1}H MRS. Acquisition conditions were: π/2 pulse, 32K data, 6 s total cycle time, 128 acquisitions. In the stability experiments, spectra were acquired immediately after sample preparation and 24 h after, comparing both. In the time course studies under normoxic conditions, tubes were left open to equilibrate with the ambient environment during the complete MR acquisition. Anoxic conditions were induced by sealing the MR tube with a rubber septum and bubbling pure nitrogen for 30 minutes. The enzymatic reaction was triggered then where appropriate by the addition of NADPH:cytochrome P-450 reductase (0.2 U/ml), the tube was quickly placed in the magnet and spectra were acquired during the next twelve hours.

Figure 8 shows the structures of the main reactants and products involved in the reduction of nitroimidazole derivatives and allows to identify specifically the chemical shifts (δ) and multiplicities of the different resonances used for the analysis (see Table 5).

Resonance assignments were made based on the chemical shifts and multiplicities of the different protons summarized in Table 5 and Figure 8. Concentrations were calculated based on the known TSP signal integral for each time point. The spectra obtained were analyzed using MestReNova software (Mestrelab Research S.L., Santiago de Compostela, Spain).

3.2.3. Kinetic Analysis

We assumed the reactions followed first order kinetics. Natural logarithms of the estimated concentrations were represented as a function of time after enzyme addition and the rate constants fitted by linear regression from the slope of appearance or disappearance of the corresponding product or reactant. For stoichiometry purposes, the net balance in reactant or product concentrations (Δ[ ]) was calculated as the difference between the initial and final concentrations. Fractional changes (% Change) in the concentration of reactants (R) or products (P), as referred to the change concentration of the hypoxic marker (HM) were calculated using the equation:

$$\%\ Change = \frac{\Delta[R\ or\ P]_x}{\Delta[HM]} \times 100 \qquad [1]$$

3.3. Cellular studies of nitroimidazole bioreduction

We investigated the biological reduction of nitromidazole compounds under different oxygen tensions and redox states using cultures of glioblastoma C6 cells.

3.3.1. Influence of the oxygen tension.

C6 cells (ATCC/LGC Promochem, Barcelona, Spain) were grown to confluence (10-cm Petri dishes, 37 ^{o}C, 5 % CO_2/95 % O_2) in Dulbecco's Modified Eagle's Medium (DMEM) supplemented with 5 % fetal bovine serum (FBS), 100 µg/mL streptomycin, 25 µg/mL gentamycin, 100 U/mL penicillin and 1 % fungizone. Prior to the experiment, cells were pre-incubated for 24h under the same oxygen concentrations used during the experiment. The medium was then replaced by DMEM containing the nitroimidazolyl derivatives (2.5 mM) and cells were incubated under the different oxygen tensions (0 %, 1 %, and 21 %) for increasing times (3, 6 and 12 hours). Incubations in normoxic and hypoxic condition (21 % and 1 % O_2 respectively) were carried out in an incubator where the ambient oxygen tension could be manipulated (Thermo Forma Series II Water Jacketed CO_2 Incubator). Anoxic conditions (0 % O_2) were achieved by adding deferroxamine (100 µM) to the incubation medium. At the end of the incubation, cells were frozen using liquid nitrogen, harvested and analyzed by high resolution magic angle spinning (HR-MAS). Each incubation condition was replicated three times.

3.3.2. Influence of the redox state.

C6 cells were grown to 90% confluence in DMEM medium as previously described. DMEM was then replaced by DMEM without glucose, L-glutamine, phenol red, sodium pyruvate and sodium bicarbonate (Sigma, D5030), but containing 2.5 mM Misonidazole analog and i) 5 mM glucose (condition 1); ii) 5 mM glucose and 10 mM lactate (condition 2); iii) 5 mM glucose and 10 mM pyruvate (condition 3) and iv) 5 mM glucose and 2 mM cysteine (condition 4). At the end of the incubation period (24 h), cells were frozen using liquid nitrogen, harvested and pellets were studied with HRMAS. Perchloric acid extracts of the individual cells pellets were prepared, neutralized with KOH, lyophilized, and resuspended in H_2O, as previously described (34,40). Extracts were analyzed for glucose and total glutathione concentrations. Each condition was replicated three times.

3.3.3. Metabolite measurements

Metabolites were determined in the perchloric acid extracts of the cellular pellets. Glucose concentration was measured spectrophotometrically (340 nm, 37 °C) by using conventional enzymatic end point methods coupled to NAD(P)H production or consumption (18). Briefly, glucose was determined by an end point assay coupled to the NADPH production, using hexokinase and glucose-6-phosphate dehydrogenase.

Total gluathione was measured spectrophotometrically using an enzymatic cycling method (412 nm, 37 °C). Briefly, it was determined through a kinetic assay in which catalytic amounts (nmoles) of GSH cause a continuous reduction of DTNB to TNB and the oxidized glutathione (GSSG) formed is recycled by glutathione reductase and NADPH. The GSSG present will also react to give a positive value in this

reaction (9). Spectrophotometric measurements were performed in 96-well polypropylene plates using a vertical spectrophotometer (Spectramax TM 340 PC, Molecular Devices, Sunnyvale, CA).

3.3.4. High resolution magic angle spinning (HR-MAS)

MR acquisitions were performed in an 11.7T (500.13 MHz) Bruker AVANCE wide-bore spectrometer equipped with a triple-nuclei (^{1}H, ^{13}C, and ^{31}P) HR-MAS probe. Cell pellets were harvested and placed in a 50 µl Zirconium Oxide rotor (Bruker Biospin, Rheinstetten, Germany) adding 30 µl of D_2O and 1 mM of TSP as an internal reference. The filled rotor was then transferred to the HR-MAS probe where sample was spun at 5 kHz, 4 ºC. 1D ^{1}H HR-MAS spectra were acquired using Carr-Purcell-Meiboom-Gill (CPMG) sequence with 2 s water presaturation, 1 ms echo time (τ) and 144 ms total spin–spin relaxation delay (2nτ), 32786 data points, 10 KHz spectral width and 512 scans (172).

3.3.5. Spectral analysis

The spectra obtained were analyzed using MestReNova software (Mestrelab Research S.L., Santiago de Compostela, Spain). Hypoxic marker signals were normalized to the total choline signal (δ = 3.2 ppm).

3.4. In vivo studies of nitroimidazole reduction

We further investigated the potential of nitroimidazole derivatives to be used in vivo as hypoxia markers using ^{1}H MRS.

3.4.1. Tumor model

The experimental protocols used in these studies were approved by the appropriate institutional review committees and met the guidelines of the appropriate government agency; all efforts were made to minimize animal suffering. Animals were housed in a humidity- and temperature-controlled room on a 12h light/dark cycle, receiving water and food *ad libitum*. The C6 glioma model was implemented essentially as described previously (58). C6 cells were grown to confluence (10-cm Petri dishes, 37 ^{o}C, 5% CO_2/95% O_2) in DMEM supplemented with 5% FBS, 100 µg/mL streptomycin, 25 µg/mL gentamycin, 100 units/mL penicillin and 1 % fungizone, harvested and kept on ice until injection. Nude mice (NU/NU, 20-25 g), were implanted subcutaneously with C6 cells (approx. 10^{6}) in flanks. Tumors were allowed to grow up to 1 cm diameter and then studied by MR.

3.4.2. In vivo Magnetic Resonance

MRI and MRS studies were performed *in vivo* during tumor development, using a 7.0 T Bruker Pharmascan system equipped with a gradient insert of 90 mm diameter (maximum intensity of 360

mT/m). A ^{1}H rat brain receive-only surface coil (circularly polarized) with integrated combiner and preamplifier, no tune/no match (T11257V1) in combination with the actively detuned transmit-only resonator (T11070V1) (Bruker BioSpin MRI GmbH, Rimpar, Germany) was employed. Data were acquired with a Hewlett-Packard console running Paravision software (Bruker Medical GmbH, Ettlingen, Germany) operating on a Linux platform. Animals were anesthetized by inhalation with 2-3 % of isofluorane in an induction chamber (1 L min^{-1}) and maintained with 2 % of isofluorane in different gases, at the same flow, through a nose mask. Three different isofluorane carriers were employed for volume selected spectroscopic measurements: 100 % oxygen (n=6), air (n=7) or a mixture of 10 % O_2 and 90 % N_2 (n= 7). In the case of spectroscopic imaging (MRSI), 100 % oxygen (n=2) and air (n=2) were used. Animals were taped down into the holder to minimize breathing-related motion, and then placed in a heated probe, which kept the core body temperature at 37^{o}C. The physiological state of the animal was monitored throughout the experiment with a Biotrig physiological monitor (Bruker Medical), using the respiratory rate and body temperature. This setup was then positioned in the isocenter of the magnet.

Anatomical T_2 weighted (T_2W) spin-echo images were acquired using Rapid Acquisition Relaxation Enhancement (RARE) sequences (75,76) and the following parameters: repetition time (TR) = 3000 ms, echo time (TE) = 60 ms, RARE factor = 8, 3 averages, field of view (FOV) = 38 x 38 mm, acquisition matrix (Mtx) = 256 × 256; 148 × 148 µm^2 in plane resolution, slice thickness = 1 mm and 16 slices. In vivo ^{1}H MR single voxel spectra were obtained using a Point Resolved SpectroScopy (PRESS) sequence with a Variable Pulse Power and Optimized Relaxation Delays (VAPOR) (43) module to suppress water signal intensity. Briefly, a voxel of 5x5x5 mm^3 was placed inside the tumor by using T_2W images as localization. First- and second-order shims were automatically adjusted with FASTMAP application in a sufficiently large voxel (6x6x6 mm^3). The spectrum was acquired with the following parameters: TR = 3000 ms, TE = 35 ms, number of scans = 128, total acquisition time = 6 min 48 s.

After the basal spectrum, the animal was removed from the magnet but maintained in the same position in the holder. An aqueous solution of the oxygen reporter MISO (1M) and TSP (2M) was intratumoraly injected (50 µL) using a gas tight syringe with a custom-made fine sharp needle (26G #7803–04; Hamilton, Reno, NV). Anatomical images and spectroscopy acquisitions as described previously were repeated. The evolution of the injected reporters was monitored during at least one hour using ^{1}H MRS. The first spectrum (reference) was obtained 20 minutes after the injection. At the end of the experiment, animals were sacrificed.

For in vivo MRSI, the multivoxel acquisition protocol was similar to previously described. Briefly, animals were located in the magnet holder and anatomical T_2W spin-echo images were acquired using RARE as explained above. The B_0 field distribution in a large voxel (40x40x40 mm^3) containing

the whole tumor was acquired (FieldMap) and used for the shim adjustment. Briefly, the tumor was localized with a coronal T_2W sequence, and first- and second-order shims adjusted with MAPSHIM application in a sufficiently large voxel containing tumor and healthy tissue. MRSI was performed in two spatial dimensions, exciting a PRESS selected volume of 8 × 8 × 4 mm. Acquisition parameters were: FOV = 32 × 32 mm, MRSI matrix = 8 × 8 zero-filled to 32 × 32, TR = 1500 ms, TE = 19.3 ms and 500 transients acquired during 12.6 min. Water suppression was performed with a VAPOR sequence. After basal spectrum, the animal was removed and injected as previously described. The animal was then introduced again in the magnet and the process repeated. The evolution of the injected reporters was monitored during at least two hours after injection. The first MRSI study (used as reference in map calculations) was obtained 30 minutes after the injection. At the end of the experiment, animals were sacrificed.

3.4.3. Data analysis

Metabolites from the in vivo MRS acquisition were quantified by measuring the area of the peaks with the software MestReNova (Mestrelab Research S.L., Santiago de Compostela, Spain) for single voxel spectroscopy. Spectroscopic images were reconstructed and quantified by using 3DiCSI 1.9.9 software (Hatch Center for MR Research, Columbia University, New York, NY). Statistical calculations were performed by using GraphPad Prism (GraphPad Software, Inc. La Jolla, USA). Chemical shift for each resonance is referred to the protons signal of the methyl group of the total creatine at 3.02 ppm. The integral of MISO's protons marked as H_a and H_b (Table 5), TSP (0 ppm) and lipids (1.5-0.7 ppm) signals were measured at each time after drug administration. The percentage of TSP and hypoxia marker relative to lipid signal was calculated using the following equation:

$$\%Compound = \frac{Area\ compound}{Area\ lipid} x100 \qquad [2]$$

For single voxel experiment, these values were represented against time and the trendline in each case was calculated by least-square non-linear regression (GraphPad Software, Inc. La Jolla, USA). Only those regressions with $r^2 > 0.8$ were accepted for further analysis. The percentage of the hypoxic marker and TSP signals remaining at the end of the experiment was calculated by the ratio of the signal obtained 60 and 20 min (reference) after the injection of the compounds.

In the case of MRSI, only those voxels with signal to noise ratio (SNR) equal or bigger than 2 were taken into account. The values compared where those obtained 70 and 30 min after the intratumoral injection. Parametric color-based maps were generated by using Matlab (2008a, The Mathaworks Inc., Natick, Massachusetts, US) based home made software.

3.4.4. Statistical analysis

Statistical significance was assessed using student's t- test and analysis of variance (ANOVA). The assumption is that inhaled gas is the independent variable while the percentage of the hypoxic marker and TSP signals remaining at the end of the experiment are the dependent variables.

3.5. DOCENT

We also propose here a new methodology to assess tumoral response to hyperoxic gas breathing without the need to administer exogenous probes. These experiments were performed in the Sowthwestern Medical center of the University of Texas at Dallas during a short term visit associated to my predoctoral fellowship.

3.5.1. Tumor model

The experimental protocols used in these studies were approved by the appropriate institutional review committees and met the guidelines of the appropriate government agency; all efforts were made to minimize animal suffering. Animals were housed in a humidity- and temperature-controlled room on a 12-h light/dark cycle, receiving water and food *ad libitum*. Two sublines of the Dunning prostate R3327 adenocarcinoma were selected: HI, a moderately well-differentiated subline, hormone-insensitive and relatively slow growing with a tumor volume doubling time (VDT) of 9 days; and AT1, a faster growing, poorly-differentiated subline with a VDT of 4.4 days (85). Pieces of freshly excised donor tumor tissue were implanted subcutaneously in the thigh of adult male Copenhagen rats (~250 g, Harlan, Indianapolis, IN), as described in detail previously (70). Tumors were investigated by MRI when small (<3 cm^3) or large (>3 cm^3). Seventeen HI tumors, including 8 smaller (size range 0.7 – 2.6 cm^3) and 9 larger (range 3.6 – 7 cm^3), and 16 AT1 tumors, including 9 smaller (range 0.75 – 2.2 cm^3) and 7 larger (range 3.1 – 5.8 cm^3) were examined. Prior experience allows tumors to be classified according to the expected level of baseline hypoxia, response to hyperoxic gas breathing and tumor growth delay in response to irradiation (25,227). Specifically, Type 1 tumors are hypoxic, do not respond to hyperoxic gas breathing and respond poorly to irradiation, as exemplified by larger Dunning prostate R3327-AT1 tumors. Type 2 tumors exhibit baseline hypoxia, but are responsive to hyperoxic gas breathing with enhanced radiation response (*e.g.*, larger HI tumors and smaller AT1 tumors) and Type 3 tumors show minimal baseline hypoxia and are inherently responsive to radiation (*e.g.*, smaller HI).

3.5.2. In vivo Magnetic Resonance Imaging

MRI experiments were performed using a Varian Unity Inova® 4.7 T horizontal bore system (Palo Alto, CA) equipped with actively shielded gradients (150mT/m). Each rat was maintained under general gaseous anesthesia (1.5 % isoflurane in air, 1 L/min). The rat body temperature was maintained using a warm water blanket. The tumor was placed inside a size-matched single-turn ^{1}H volume coil. Imaging protocol is summarized in Figure 9. Briefly, following shimming on tissue water signal to a typical linewidth of 50 Hz, a Spin Echo Multiple Slice (SEMS) sequence was applied to acquire T_1 maps under air breathing (baseline) with the TR arrayed as 9 values from 100 ms to 3500 ms, TE = 20 ms, FOV = 40 × 40 mm, Mtx= 64 × 64, slice thickness = 1.5 mm and 3 slices separated by 1 mm space in 10.5 min. Baseline T_2* maps were obtained with a Gradient Echo Multiple Slice (GEMS) sequence using TR = 195 ms, TE arrayed as 7 values from 7 ms and spacing 6 ms and the same spatial resolution as for T_1 maps in 3 min. Slice positioning and geometry were maintained through all the subsequent experiments. Then a series of 5 T_1 weighted images (T_1W), with TR = 30 ms, TE = 5 ms, Mtx = 128 x 128, slice thickness= 1.5 mm, flip angle (α) = 45°, acquisition time = 3 s, and T_2* weighted images (T_2*W), with TR = 150 ms, TE = 20 ms, Mtx = 128 x 128, slice thickness= 1.5 mm, α = 20°, acquisition time = 19 s, spoiled gradient-echo images were acquired in an interleaved fashion, as baseline. At this point, the breathing gas was changed to carbogen (1 L/min) and a series of 20 interleaved T_1W and T_2*W images were acquired over 10 min. Finally, T_1 and T_2* values were measured again during carbogen inhalation.

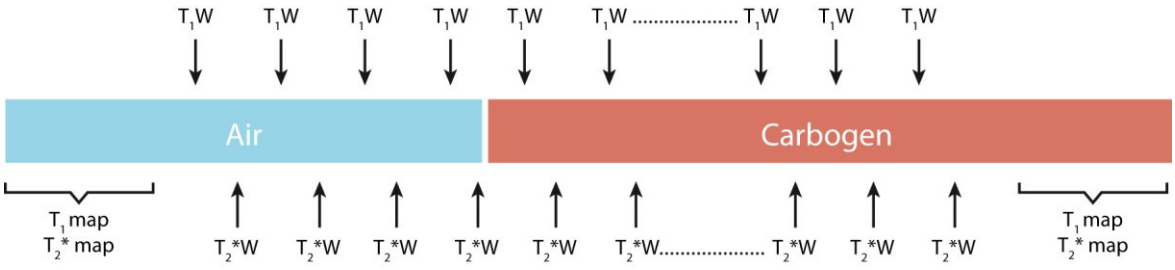

Figure 9. Scheme of gas breathing sequence and image acquisition protocol for BOLD /TOLD experiment. Sequence acquisition times were as follow, T_1 map = 10.5 min, T_2* map= 3 min, T_1 weighted (T_1W) = 3s and T_2* weighted (T_2*W) = 19 s.

3.5.3. Data analysis

Data analysis was performed using IDL-based software. Briefly, signal intensity (SI) in the initial five T_1W or T_2*W images (during air breathing) was averaged to obtain mean baseline images. Normalized image SI values were then calculated on a voxel-by-voxel basis by following the expression:

$$\Delta SI(\%)_{i,m,n} = \frac{SI_{i,m,n}}{(\sum_{i=1}^{5} SI_{i,m,n}/5)} * 100 - 100 \quad [3]$$

where *i* is the image number, *m* and *n* are the image matrix, and *SI* is the voxel intensity. T_1 values for a given voxel were obtained by fitting the signal intensities corresponding to nine delay values to a three-parameter least squares curve, using a Levenberg-Marquardt algorithm. T_2* values for a given voxel were obtained by fitting an exponential model of signal decay curve. Common voxels (typically, 1300 to 2500 depending on tumor size) were compared under carbogen and air breathing and differences calculated:

$$\Delta R_1 = (R_{1\,CB} - R_{1\,Air}) \;\&\; \Delta R_2* = (R_2*_{CB} - R_2*_{Air}) \quad [4]$$

3.5.4. Statistical analysis

Statistical significance of changes in SI in T_1W and T_2*W images and relaxation rates was assessed using GraphPad Prism (GraphPad Software, Inc. La Jolla, CA) or Statview (SAS Inc., Carey, NC) software with one way ANOVA and Fisher's Protected Least Significant Difference (PLSD) or Student's t-tests. Data are presented as mean ± standard error (SE).

4. RESULTS

4.1. Reduction of Nitroimidazolyl derivatives as detected by MRS

4.1.1. Synthesis and characterization of new 2-nitroimidazolyl derivatives as hypoxia markers

The synthetic route to dimethyl 2-(2-Nitro-1*H*-imidazol-1-yl)succinate **4** (NISUCA) is depicted in Scheme 2. Briefly, 2-nitro-1H-imidazole (**1**) reacted with a slightly excess of dimethyl acetylenedicarboxylate in acetonitrile (MeCN) at 80 °C, giving Z/E-isomers **2** (61%) and **3** (17%). The structures of **2** and **3** were well characterized by spectroscopic methods and confirmed by X-ray diffraction analysis (164). Subsequent attempts to reduce of the double bond of compounds **2** and **3** using palladium on carbon and ammonium formate or Wilkinson catalyst were unsuccessful and the starting materials recovered. Compound **4** was only isolated, in 80% yield, by selective reduction of **2** with borane in tetrahydrofuran at 0 °C. No evolution of **3** was observed, and compound **2** was exclusively reduced. Isomerization of compound **3** to **2** was achieved by refluxing **3** with 4-toluenesulfonic acid in MeCN. Hydrolysis of **4** was carried out under neutral, acidic, or alkaline media. Retro-Michael reaction products were isolated under basic conditions whereas, in acidic medium, degradation products of the compound **4** were observed. Finally, compound **5** was only obtained by stirring **4** in water at room temperature for more than 30 days, but not as a totally pure sample.

It is well known that 2-nitroimidazolyl derivatives are sensitive to low oxygen concentrations due to their selective reduction and subsequent trapping in hypoxic regions. This property is dependent of the redox potential. Thus, the first step to know whether compound **4** could be used as hypoxia marker was to determine its redox potential. Compound **1** was used as a reference. Table 6 summarizes the redox potential ($E_{1/2}$) of compounds **1** and **4** obtained using cyclic voltammetry. $E_{1/2}$ is defined as

$$E_{1/2} = \frac{E_{cp}+E_{ap}}{2} \qquad [5]$$

where E_{cp} is E of cathodic peak and, E_{ap} is E of anodic peak.

Table 6. Redox potential of 2-Nitroimidazole compounds and NISUCA.

Compound/Medium	DMF, $Bu_4N^+BF_4^-$		Phosphate buffer 0.1 M, pH = 7.2	
	E_{cp} [a] (V)	$E_{1/2}$ [a] (V)	E_{cp} [b] (V)	$E_{1/2}$ [b] (V)
2-Nitroimidazole (1)	-0.872 -1.973	- -1.900	-0.698 -1.287	- -
NISUCA (4)	-0.989 -1.953	-0.934 -1.888	-0.615 -1.138	-0.551 -

Cyclic voltammograms (CV) of all compounds were carried out (6 mM solutions) in two different media. The scan rate was 100 mV s^{-1}. CV analysis was supported using a glassy carbon electrode (GCE), Ag/AgCl, Cl^-/3 M KCl, and platinum as reference and auxiliary electrodes, respectively.

[a] Aprotic media: Dimethylformamide (DMF), 0.1 M $Bu_4N^+BF_4^-$.

[b] Protic media: phosphate buffer pH 7.2.

As indicated in Table 6, the reduction potential of the nitro group of molecules **1** and **4** was medium dependent. We aimed to study the formation of the nitro radical anion in a medium where it was kinetically stable (aprotic solvents). Cyclic voltammetry of **4** in aprotic solvent represented two reversible reduction peaks, one of them at less negative potential, $E_{1/2}$ = –0.934 V, probably corresponding to the formation of the nitro radical anion (reversible according to CV). Irreversible reduction at –0.872 V was observed for the 2-nitroimidazole **1** containing active hydrogens. In order to determine values for the redox potentials in a pH range simulating biological conditions, we investigated additionally the corresponding potentials in protic medium, such as phosphate buffer (pH 7.2), Compound **4** exhibited $E_{1/2}$ = –0.551V.

4.1.2. Enzymatic reduction in a cell free system

To investigate the mechanism of nitroimidazole reduction, and the main determinants affecting the reduction rate, we choose the NADPH:cytochrome P450 reductase as in vitro enzymatic system. Several studies have shown that this is the main enzyme involved in the in vivo reduction of 2-nitroimidazoles but the mechanism remained elusive yet (3,91,216) .

First, we assessed the stability of the reactants and products to non enzymatic catalysis under the same conditions used later for the enzymatic analysis. In the absence of enzyme, NADPH showed a spontaneous disappearance without concomitant $NADP^+$ generation, either when present alone or in a mixture with other compounds. Reduced glutathione (GSH) was stable when alone, but it depicted a small spontaneous reduction in presence of NADPH. $NADP^+$ and GSSG were stable both alone and in presence of other compounds. The enzymatic system had no effect on the stability on these compounds. To avoid contamination from the spontaneous reactions, NADPH and GSH consumptions were measured through the production of $NAPD^+$ and GSSG since these compounds were unaffected in the absence of P450ase.

In order to characterize the main determinants of nitroimidazole reduction, representative reactions of Misonidazole (MISO) with P450ase were investigated under different conditions. A summary of the results is depicted in Table 7. MISO was not reduced spontaneously under any of the investigated conditions (Table 7, conditions **b**). Therefore, the enzymatic system is a necessary requirement for this reaction to take place (Table 7, conditions **a**). The reduction only took place when NADPH was present in the medium (Table 7, conditions 1a, 5a and 6a). GSH alone was not able to reduce MISO (Table 7, condition 3a), but when added to NADPH, increased drastically the MISO reduction rate (Table 7, condition 6a), as compared to that found with NADPH alone (Table 7, condition 1a). NADP+ nor GSSG, alone (Table 7, conditions 2a and 4a) or in combination with other compounds (Table 7, conditions 6a, 7a and 8a), depicted any additional affect in the MISO reduction rate.

Table 7. Principal determinants of MISO reduction.

Condition	NADPH	$NADP^+$	GSH	GSSG	Enzyme	MISO reduction rate	Subsidiary reactions
1a	+	-	-	-	+	Slow	Fast NADPH disappearance
1b	+	-	-	-	-	No reaction	**Slow NADPH disappearance**
2a	-	+	-	-	+	No reaction	
2b	-	+	-	-	-	No reaction	
3a	-	-	+	-	+	No reaction	**Slow GSH disappearance**
3b	-	-	+	-	-	No reaction	**Slow GSH disappearance**
4a	-	-	-	+	+	No reaction	
4b	-	-	-	+	-	No reaction	
5a	+	-	+	-	+	Fast	**Fast NADPH disappearance. Fast GSH disappearance**
5b	+	-	+	-	-	No reaction	**Slow NADPH disappearance**
6a	+	-	-	+	+	Slow	**Fast NADPH disappearance**
6b	+	-	-	+	-	No reaction	**Slow NADPH disappearance**
7a	-	+	+	-	+	No reaction	
7b	-	+	+	-	-	No reaction	
8a	-	+	-	+	+	No reaction	
8b	-	+	-	+	-	No reaction	

The reactions were followed by ^{1}H MR as indicated in Methods. Phosphate buffered (75 mM, pH= 7.7, 37^{o}C, 10% D_2O) reaction mixtures containing MISO (5 mM), NADPH (15 mM), $NADP^+$ (15 mM), GSH (10 mM), GSSG (5mM) and NADPH:cytochrome P-450 reductase (0.2 U/ ml) where appropriate, were prepared in 5 mm MR tubes using TSP (1 mM) as an internal reference.

To gain insight into the mechanism of reduction of the different hypoxic markers, we tested four nitroimidazolyl derivatives (Figure 8), both commercially available (MISO analog and PIMO) and synthesized in our lab (NIMAC and NISUCA). Briefly, we used buffered aqueous reaction mixtures (75 mM phosphate buffer, pH= 7.7, 22 ^{o}C), containing NADPH (15 mM), TSP (1 mM), D_2O (10%), GSH (10 mM, where indicated), P450ase (0.2 U/ml, where indicated), GR (1 U/ml, where indicated), and the corresponding nitroimidazole derivative (5 mM). Experiments were performed under four characteristic environments: normoxia; anoxia; normoxia plus GSH and anoxia plus GSH. The reactions were triggered by the addition of the enzymatic system to the MR tube containing the appropriate reactants. The time course of the reaction was followed by ^{1}H MRS, thus allowing monitoring simultaneously the time evolution of the different metabolites observed. Figure 10a illustrates at increasing time points, the reduction of MISO in presence of NADPH and GSH under normoxic conditions. MISO (orange), NADPH (red) and GSH's (purple) resonances could be clearly detected at the beginning of the experiment (Figure 10a, time 10 min, lower spectra). These resonances decreased with increasing time (Figure 10a, upper spectra), while NADP+ (blue) and GSSG (green) resonances increased.

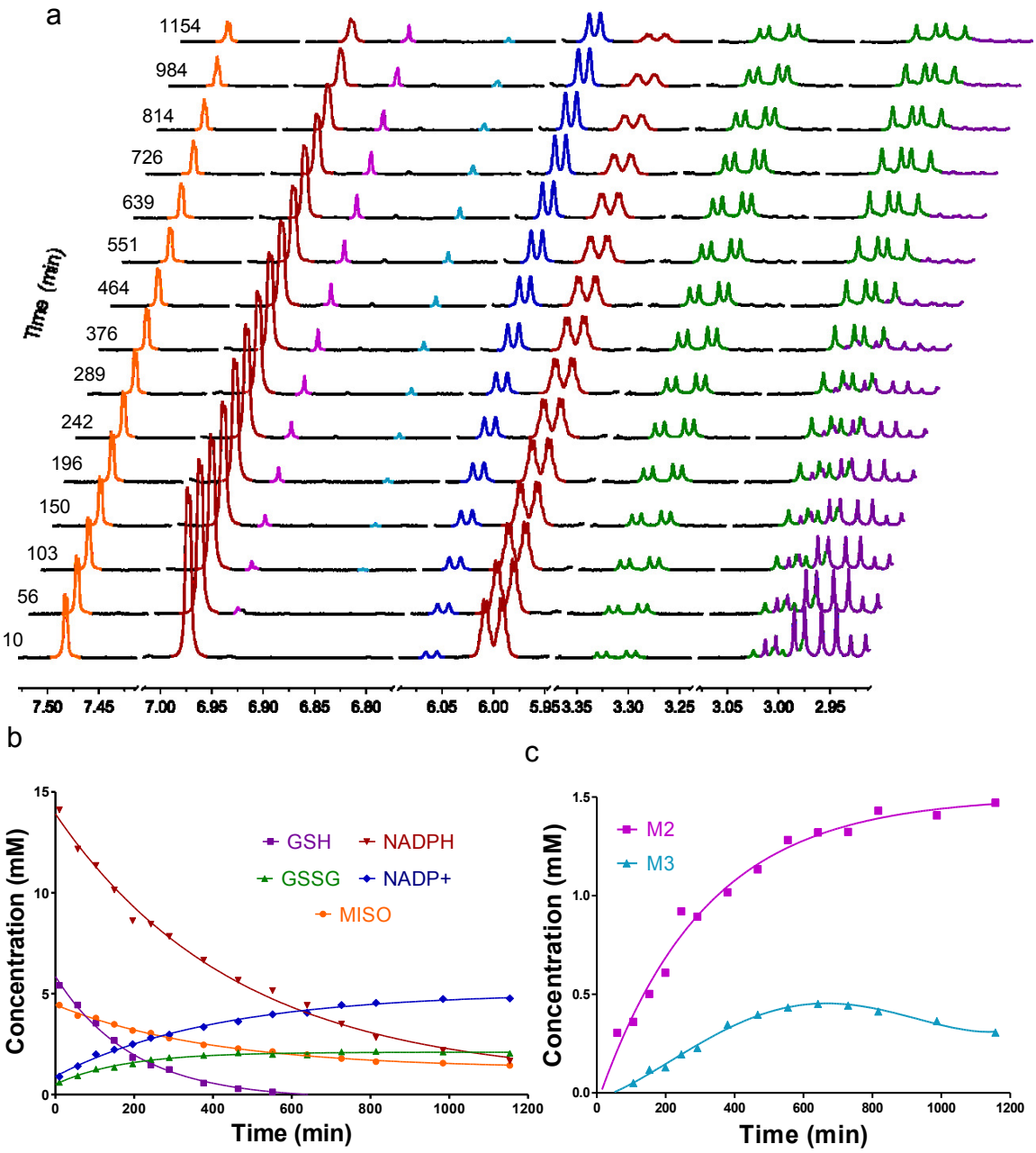

Figure 10. Kinetics of MISO reduction by P450ase under aerobic conditions in the presence of GSH.
a) Relevant regions of the ^{1}H MR spectra of the reaction mixture at increasing times. b) Monoexponential decays of MISO, NADPH and GSH and monoexponential increase of $NADP^{+}$ and GSSG concentrations with time after the addition of P450ase. c) Changes with time of the newly generated resonances M2 and M3. MISO (orange), NADPH (red), GSH (purple), $NADP^{+}$ (blue) and GSSG (green).

The observed changes in concentration were fitted to a monoexponential function, (Figure 10b), and the apparent reaction rate constants determined as indicated in Methods. The MISO reduction rate constant was greatly increased in the presence of GSH, becoming 29 and 20 times faster in normoxia and anoxia, respectively (Figure 11a). Notably, molecular oxygen had a drastically smaller impact in the reduction rate of MISO, increasing the reduction rate 2 times only in anoxia with respect to

normoxia, (Figure 11a, insert). Overall, there is a tendency towards a faster reduction rate in anoxia than in normoxia. GSH also increased the production rate of $NADP^+$, but not as much as with MISO (Figure 11b). It is worth mentioning that there was a mismatch between the reaction rates of the redox pair GSH/GSSG (Figure 11b). 75% of reduced glutathione is recovered as the oxidized counterpart at the end of the reaction, being the reduction rate of GSH twice faster than the formation rate of GSSG under normoxic conditions. It is also important to note that some new resonances appear as singlets around 7 ppm (Figure 10a, M2 and M3). Their time course is complex, following an exponential growth (M2, Figure 10c) or a biphasic response with initial increases followed a decrease (M3, Figure 10c). These new signals appear only when GSH is present in the reaction mixture.

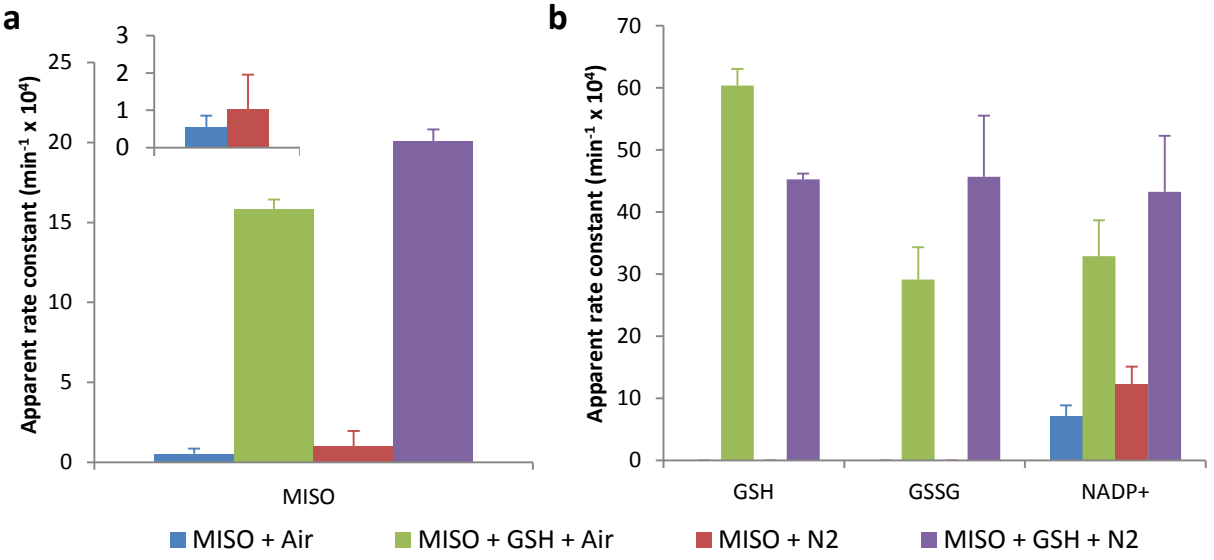

Figure 11. Apparent rate constants for the reduction of MISO under different conditions.
a) Apparent rate constants for the reduction of MISO. b) Apparent rate constants for GSH consumption and GSSG or $NAPD^+$ production. Normoxia (blue), normoxia + GSH (green), anoxia (red) and anoxia + GSH (purple).

Similarly to MISO, PIMO (gray), NADPH (red) and GSH's (purple) resonances decreased with time after the addition of the enzyme (Figure 12a), whereas $NADP^+$ (blue) and GSSG's (green) resonances increased. Changes in concentration with time were fitted to a monoexponential equation (Figure 12b) and rate constants derived. There was a cohort of new resonances appearing in the 6.90-7.05 ppm interval (P2-P5, Figure 12a). Some of them reached a maximum at different times and then began to decrease (P3-P5, Figure 12c) whereas others followed an exponential growth along the entire reaction time (P2, Figure 12b). It should be highlighted here that these signals appeared only when GSH was present in the medium and that they do not originate from any of the well known components of the reaction mixture. GSH induced a marked increment in PIMO's reduction rate, 100 times in normoxia and 60 times in anoxia, as compared with the rates obtained with NADPH alone (Figure 13a). Notably, there was little difference when carrying the reaction in presence or in the

absence of oxygen (Figure 13a, insert). As previously observed, GSH increased the rate of $NADP^+$ generation, but not as much as during the reduction of MISO. There was a mismatch between the rate constants of disappearance of GSH and appearance of GSSG, the rate of disappearance of GSH being 24 and 13 times faster than the rate of appearance of GSSG under normoxic or anoxic conditions, respectively (Figure 13b).

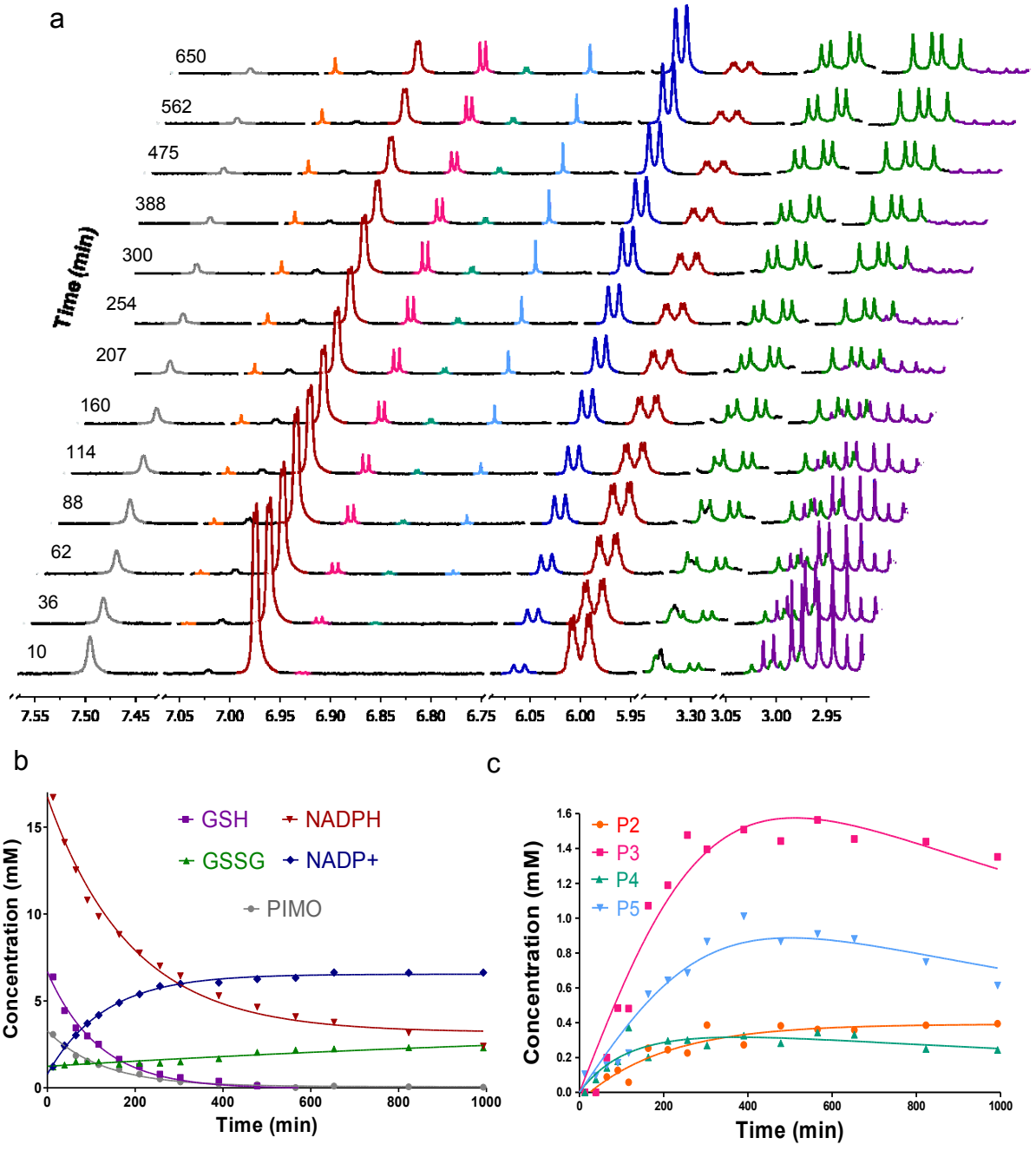

Figure 12. Reduction of Pimonidazole with P450ase under aerobic conditions in the presence of GSH.
a) Relevant regions of ^1H MR spectra from the reaction mixture at increasing times. b) Monoexponential decreases of PIMO, NADPH and GSH and monoexponential increases of $NADP^+$ and GSSG after addition of the enzyme. c) Changes with time of the newly generated resonances P2, P3, P4 and P5 originated during the reaction. PIMO (gray), NADPH (red), GSH (purple), NADP+ (blue) and GSSG (green).

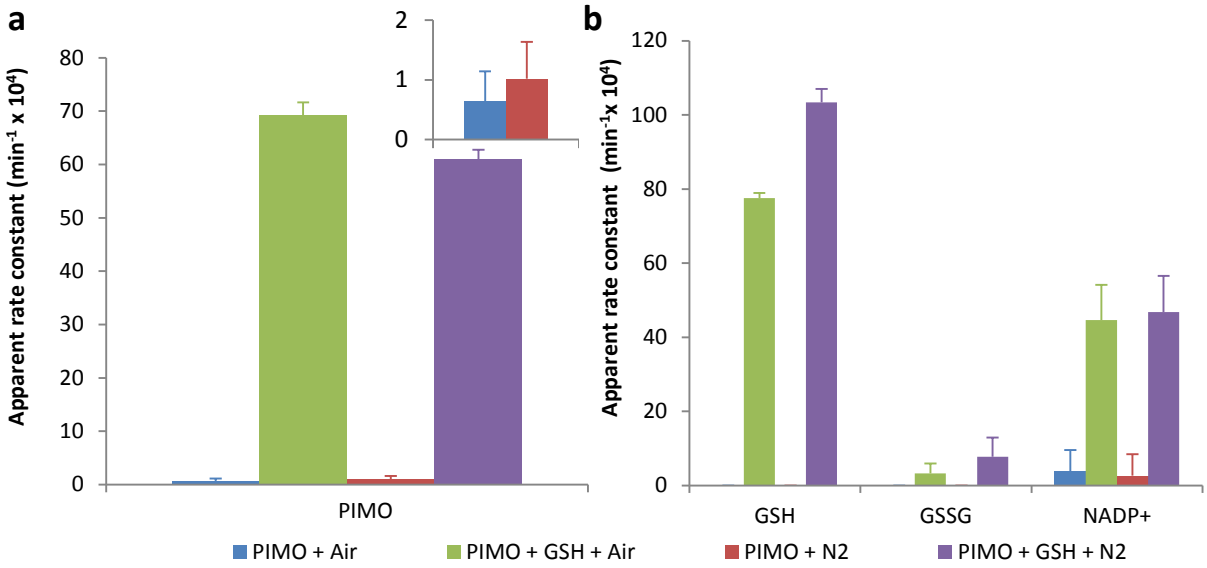

Figure 13. Apparent rate constants for the reduction of PIMO under different conditions.
a) Apparent rate constants for the reduction of PIMO. b) Apparent rate constants for GSH consumption and GSSG or $NAPD^+$ production. Normoxia (blue), normoxia + GSH (green), anoxia (red) and anoxia + GSH (purple).

In the case of the nitroimidazole derivative NIMAC, synthesized in our labs, its resonances (gold, orange?) as well as those of NADPH's (red) and GSH's (purple) decreased with time whereas those of NADP+ (blue) and GSSG (green) increased (Figure 14a). We fitted the changes in concentration after enzyme addition to a first order kinetic model (Figure 14b), determining the corresponding apparent rate constants for the different molecules observed. In contrast to previously tested hypoxia markers, a new pair of doublets appeared close to NIMAC original resonances (Figure 14a, orange squares and 14c orange), following an exponential growth. These doublets are present both in absence and presence of GSH, although in the presence of GSH their production remained smaller. Similarly to the previous nitroimidazoles, a new group of resonances in the 6.7-7.0 interval ppm appeared only when GSH was present (Figure 14a & c, NM2-NM6). They followed complex kinetics, some increasing very early in the experiment; achieving a maximum at different times during the reaction course and finally decreasing towards the end (NM4 and NM6, Figure 14a & c). Others appeared later in the time course of the reaction and grew then exponentially until the end (NM3 and NM5, Figure 14a & c).

GSH increased the reduction rate of NIMAC between 3 (normoxia) and 6 (anoxia) times as compared to NADPH alone (Figure 15a). These increases were not as prominent as those found in the other commercial hypoxia markers investigated. This could be explained because of the higher NIMAC reduction rate when GSH was not present in the medium, approximately 20 times faster when compared to MISO or PIMO. The presence of oxygen resulted in opposite effects in the reduction

rate of NIMAC than those previously described. Its absence decreased 30% the rate constant for NIMAC reduction when no GSH was present (Figure 15a insert). In contrast, anoxic conditions increased by 20% the reduction rate of NIMAC with respect to normoxia, when GSH was present (Figure 15a). Similarly to the other commercial hypoxia markers, $NADP^+$ generation (and NADPH consumption) was exacerbated in presence of GSH (Figure 15b). There was also a mismatch between GSH consumption and GSSG production, becoming 7 and 3 times faster in normoxia and anoxia conditions respectively (Figure 15b).

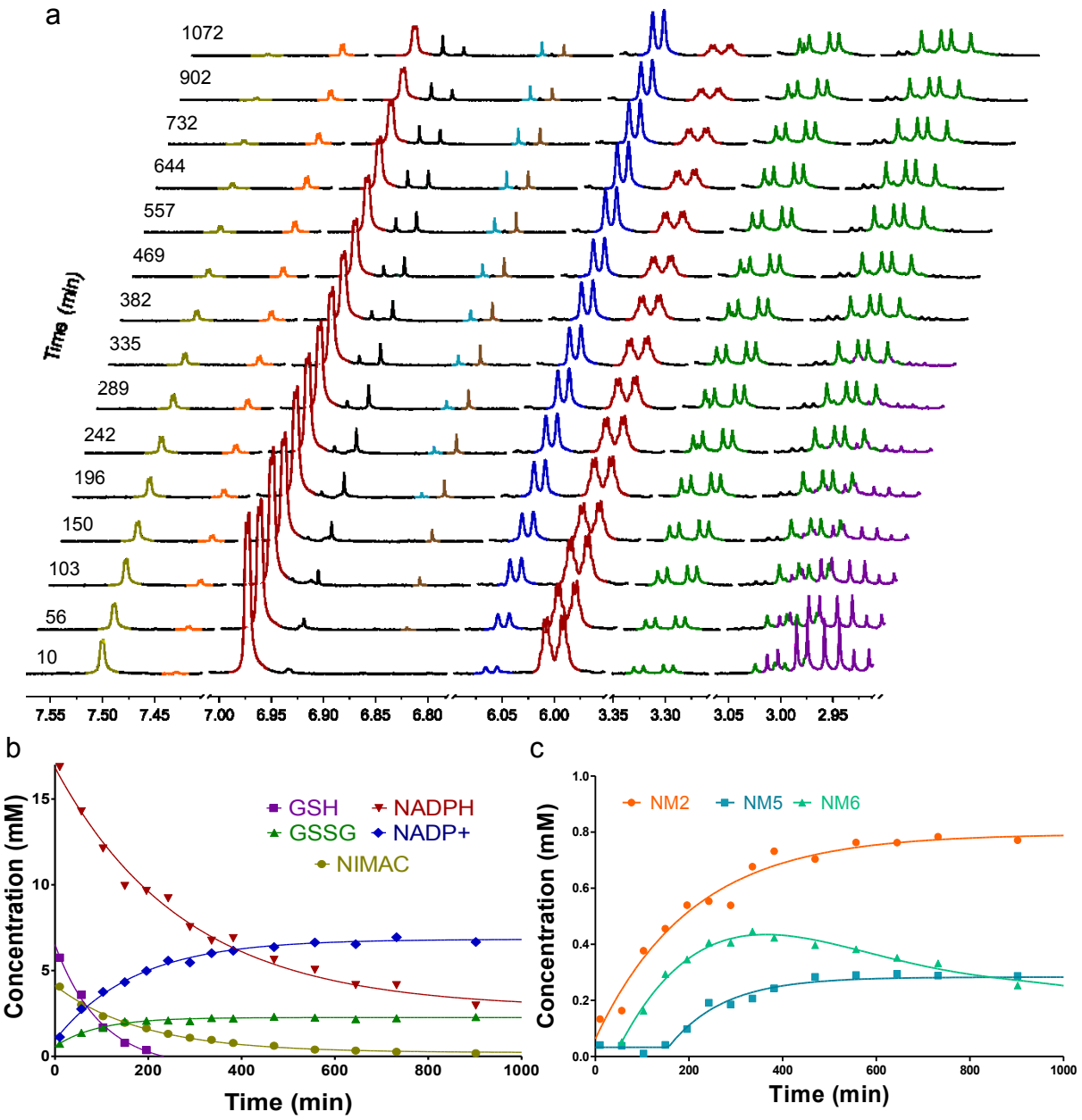

Figure 14. Reduction of NIMAC with P450ase under aerobic conditions in the presence of GSH.
a) Relevant regions of the ^{1}H MR spectra of the reaction mixture at increasing times, b) Monoexponential decays of NIMAC, NADPH and GSH and monoexponential increase of $NADP^+$ and GSSG concentration after the addition of the enzyme, c) Changes with time of the newly generated resonances (NM2, NM5, NM6). Assignments are proposed based on theoretical calculations of the chemical shift of the possible reaction products. NIMAC (orange), NADPH (red), GSH (purple), NADP+ (blue) and GSSG (green).

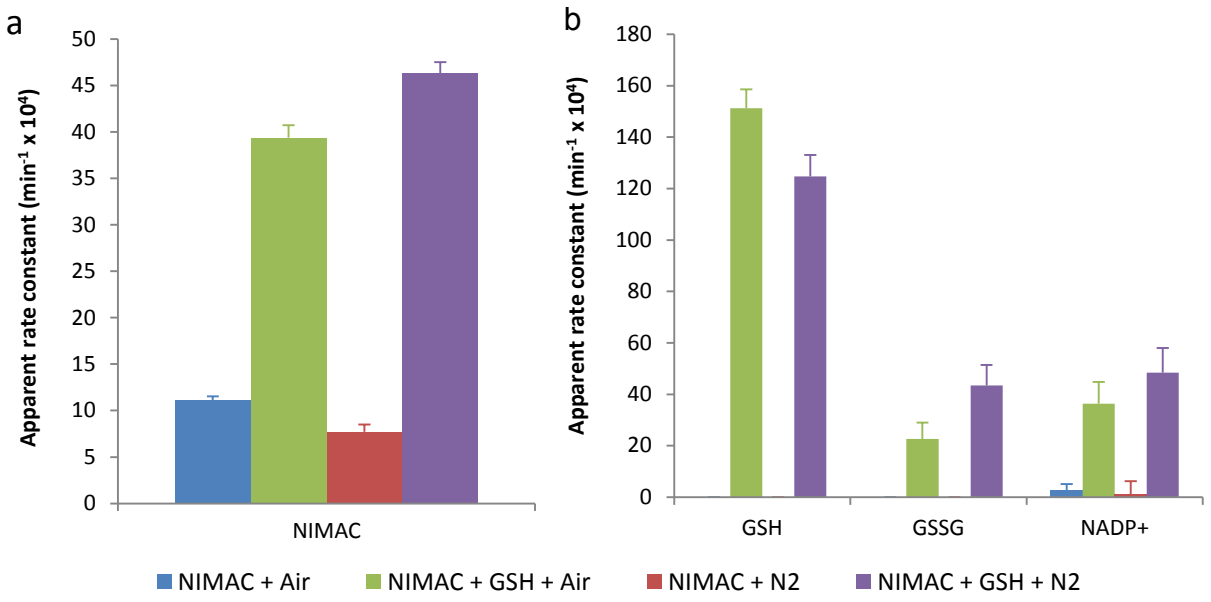

Figure 15. Apparent rate constants for the reduction of NIMAC under different conditions.
a) Apparent rate constants for the reduction of NIMAC. b) Apparent rate constants for GSH consumption and GSSG or $NAPD^+$ production. Normoxia (blue), normoxia + GSH (green), anoxia (red) and anoxia + GSH (purple).

Finally, the same set of experiments were performed with an additional 2-nitroimidazole derivative synthesized in our labs (155), NISUCA. As observed before, NISUCA (pink), NADPH (red) and GSH (purple) diminished with time (Figure 16a) while $NADP^+$ (blue) and GSSG (green) increased. These compounds followed apparently first order kinetics and the corresponding apparent rate constants were calculated by fitting the changes in concentration to a monoexponential equation (Figure 16b). The pattern of the new resonances arising during the reaction time course was more complex than in the aforementioned nitroimidazole derivatives. More specifically, new pairs of doublets appeared close to the original NISUCA signal (N2, Figure 16a & c) as with NIMAC. These were present both in presence and absence of GSH, although they became more abundant in the absence of GSH. As with other hypoxia markers, there was a group of resonances, both singlets (N3-N5, Figure 16a & c) and doublets (N6 and N7, Figure 16a & c) in the 6.8-7.1 ppm interval that only became visible when GSH was present in the incubation medium. Some of these new resonances increased at the beginning, reached a maximum and then decreased (N3, N5 and N6, Figure 16c) whereas others followed a hyperbolic growth (N4 and N7, Figure 16c). N2 reached a plateau level very early in the reaction and did not change significantly thereafter (Figure 16c). Notably, when GSH was not present, new singlet resonances were detected in the same spectroscopic area. They were different from those originated in the presence of GSH, depicting also a complex kinetic behavior as previously described. Molecular oxygen induced a small effect in the reduction rate of NISUCA under all the tested conditions (Figure 17a). GSH increased approximately 3 times the reduction rate of NISUCA, both in normoxia and in anoxia. The effect of reduced glutathione in the reduction rate of the nitroimidazolyl derivative was smaller than with MISO and PIMO, but similar to NIMAC. This effect could also be explained due to

the high reduction rate found without GSH in the medium, which was around 80 times higher than with the commercial markers for hypoxia. As previously found with the other nitroimidazoles, NADPH consumption was increased when reduced glutathione was present in the reaction mixture (Figure 17b). As in previous cases, the apparent rate constants for GSH disappearance and GSSG appearance were mismatched (Figure 17b), being 4 and 20 times faster for GSH in presence and absence of oxygen respectively. NISUCA's rate constants were higher compared with other nitroimidazolyl derivatives in all tested conditions.

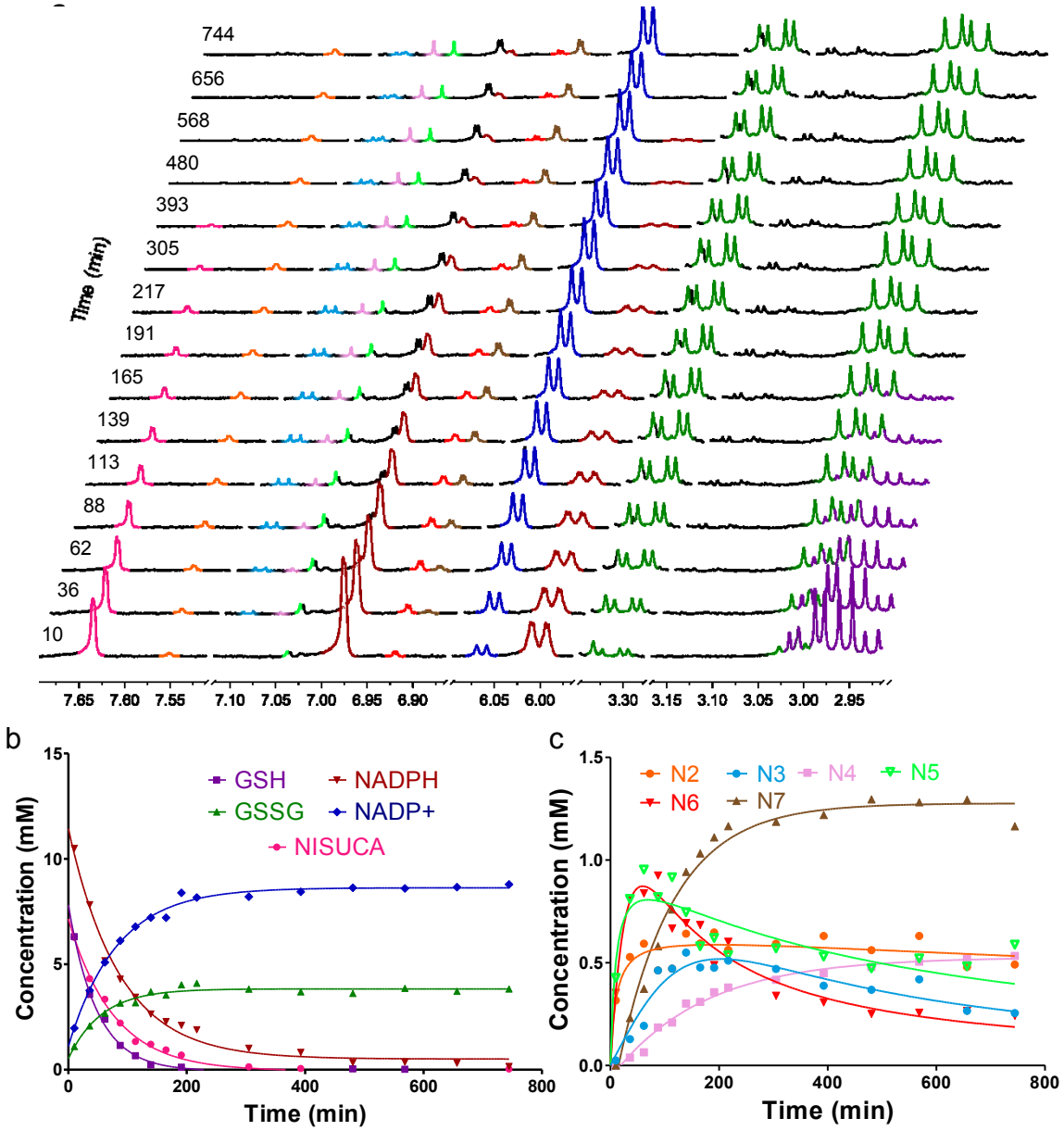

Figure 16. NISUCA reduction in vitro with P450ase under aerobic conditions in the presence of GSH.
a) Relevant regions of the ^{1}H MR spectra of the reaction mixture at increasing times. b) Monoexponential decays of NISUCA, NADPH and GSH and monoexponential increase of $NADP^{+}$ and GSSG with time after addition of the enzyme. c) Changes with time of the new generated resonances (N2, N3, N4, N5, N6 and N7). NISUCA (pink), NADPH (red), GSH (purple), $NADP^{+}$ (blue) and GSSG (green).

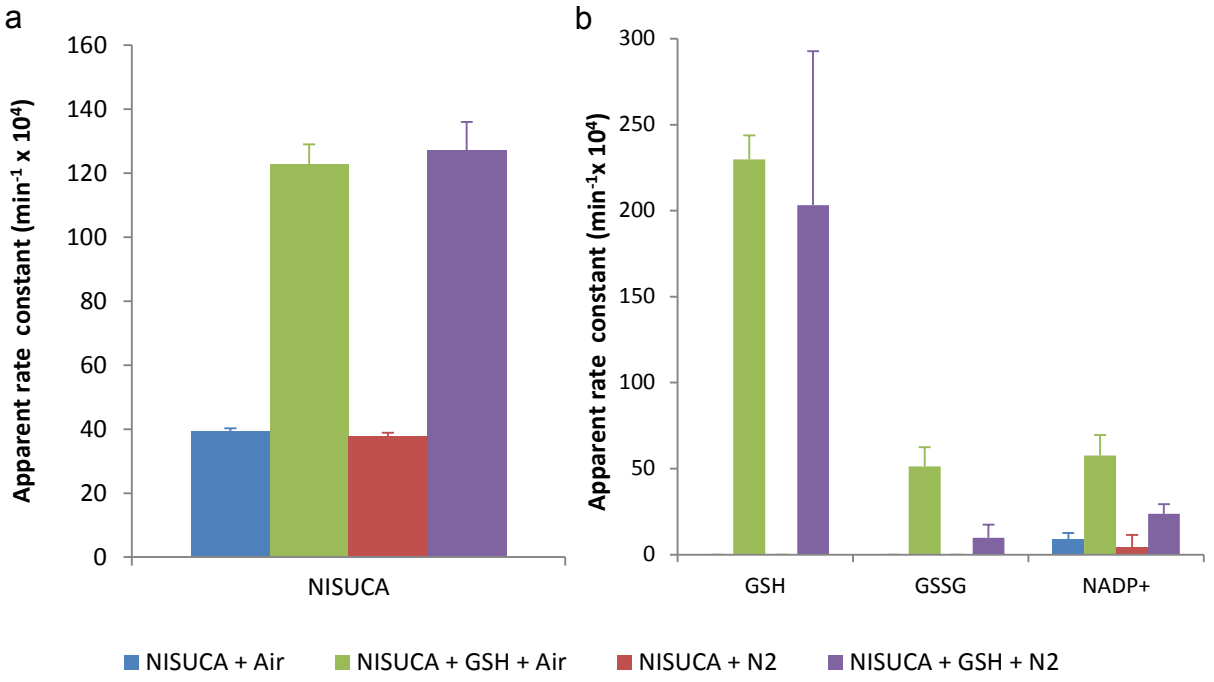

Figure 17. Apparent rate constants for the reduction of NISUCA under different conditions
a) Apparent rate constants for the reduction of NISUCA. b) Apparent rate constants for GSH consumption and GSSG or NAPD$^+$ production. Normoxia (blue), normoxia + GSH (green), anoxia (red) and anoxia + GSH (purple).

To investigate in more detail the role of GSH in the reduction process of hypoxic markers, the reactions were carried out in the presence of two enzymatic systems: P450ase and GR. This last system regenerated GSH levels as GGSG was formed and thus kept constant the GSH level during the entire time course of the reaction. For the commercial hypoxia markers MISO and PIMO, we found no significant changes in the reduction process under these conditions. However, with our home made NIMAC and NISUCA, the presence of GR approximately doubled their reduction rates both in absence and in presence of oxygen. Regarding the newly generated signals, their kinetic behavior did not change significantly in most of the cases. Only NISUCA depicted significant modifications. In this case, some of the signals that accumulated during the reaction (N7, Figure 16c) showed a decrease at certain stage when GR was present. Other signals, shifted from an increase and posterior decrease (N5, Figure 16c) to a continuous increase. To gain insight into the stoichiometry of the reduction, changes observed in GSSG and NADP$^+$ concentrations were compared to those detected in the hypoxia probe. NADPH and GSH were not used for this purpose since they depicted spontaneous, non enzymatic disappearance, without concomitant NADP$^+$ and GSSG production under the studied conditions. In the presence of reduced glutathione, the reduction of 1 mol of nitroimidazolyl derivative was accomplished with the oxidation of 1.5 to 2 mol of NADPH (which renders 2 electron per molecule oxidized) and 1 mol of GSH (with the concomitant liberation of 1 electron per molecule oxidized), resulting in a 4 to 5 electron reduction stoichiometry (Figure 18). No significant differences were found between the normoxic and anoxic conditions.

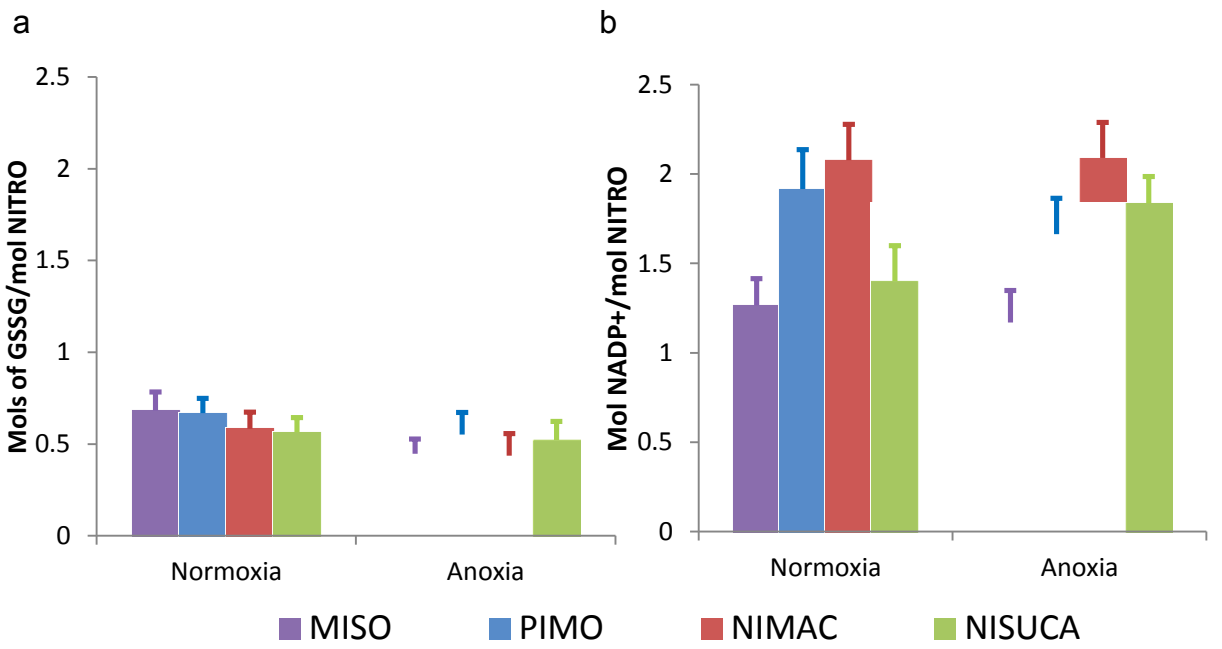

Figure 18. Stoichiometry of the reduction reaction.
a) Mol of GSSG produced by mol of NITRO consumed. b) Mol of $NADP^+$ produced by mol of NITRO consumed.

It should be stressed here that if we follow the total glutathione concentration (GSH + GSSG) by their H_b proton, which depict the same chemical shift (Table 5), its equivalents remained constant along the reaction coordinate. However, if we used H_a protons, which have different chemical shifts for GSH and GSSG (Table 5), we found that total glutathione decreased at the beginning of the reaction and then increased. But not all the GSH present originally was recovered as GSSG, indicating the existence of GSH/GSSG sink. Usually, only around 50% of the parental GSH is recovered as its oxidized counterpart at the end of the reaction. In the case of NISUCA, this recovered percentage increases reaching 75% of the initial GSH. These evidences revealed the formation GSH-nitroimidazole derivative conjugate during the reduction reaction. These adducts may be formed by the link of the thiol group of GSH to either the imidazole ring or the nitro moiety of the probe. GSH's and GSSG's H_b are located far away from thiol group and a link trough it would not affect significantly the chemical shifts of the H_b resonances. However, the H_a's are closer to the thiol group and thus, any chemical change in this moiety will be reflected in the chemical shift of these resonances. Importantly, new groups of multiplets were detected between 3.30 to 3.05 ppm (Figure 16a and Figure 19a). In order to characterize the influence of the initial concentration of hypoxia probe in the reduction rate, the reactions were implemented in the presence of different initial concentrations of MISO and NIMAC (Figure 20). The kinetics were followed for two hours to avoid interferences from the changes in other factors occurring at later stages (i.e, total consumption of NADPH or GSH). In the case of MISO (Figure 20a), reduction rate increased linearly with initial hypoxia marker concentration in both normoxia (r^2 = 0.9984) and anoxia (r^2=0.9468). However, NIMAC (Figure 20c)

followed an asymptotic growth reaching the maximum at 10 mM. The oxygen tension did not play an important role when NIMAC concentration was lower than 5 mM. At higher concentrations, the anoxic condition resulted in higher reductions rates. The impact of GSH in the reduction rate of MISO and NIMAC was assayed using a similar strategy. In this case, reduction rates increases with GSH concentration reaching a plateau at 10 mM. No significant differences were found between anoxia and normoxia for none of the hypoxia marker probes (Figure 20 b & d).

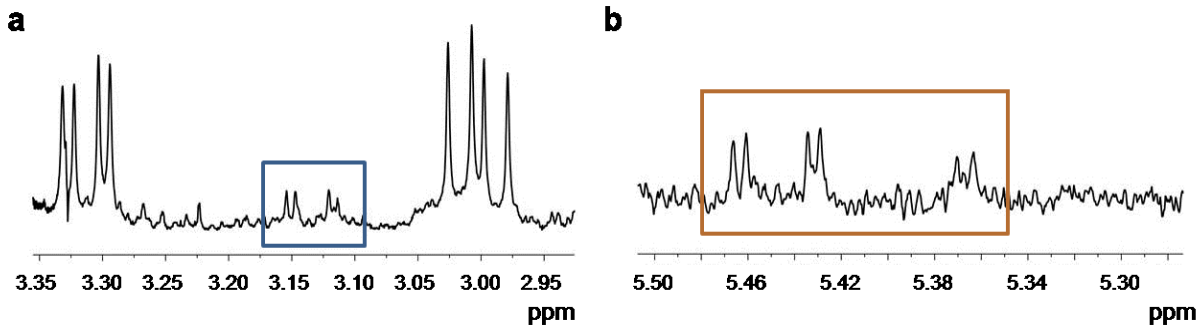

Figure 19. Newly generated resonances during the reduction of NISUCA with NADPH:cytochrome P450 reductase under aerobic conditions in presence of GSH.
a) Newly generated signals (blue square) for H_a protons of GSH when forming an adduct with NISUCA. b) Newly generated signals for H_a and H_b of NISUCA when forming and adduct with GSH.

4.1.3. Enzymatic reduction in a cell containing system

Next step was to test whether ^{1}H MRS was a suitable technology to detect hypoxia in vivo using 2-nitroimidazolyl derivatives. The four hypoxia markers previously investigated in cell free systems were incubated with C6 glioma cells, with different environmental oxygen concentrations. At the end of the incubation period, cell pellets were harvested and studied by HR-MAS. Figure 21 showed a representative ^{1}H HR-MAS spectrum from cell pellet incubated for six hours with NISUCA under hypoxic conditions (1% O_2). The resonances from NISUCA's H_a and H_b can be conveniently observed between 7.2 and 7.7 ppm. The reduction in the intensity of NISUCA's resonances (orange rectangles) for decreasing environmental oxygen tensions is depicted in the insert of Figure 21. PIMO rendered similar results, as shown in Figure 22. There was a significant decrease in the intensity of the hypoxia marker resonances (insert Figure 22, orange rectangles) between normoxic (blue) and hypoxic (red) or anoxic (green) conditions, indicating larger reductions under hypoxic or anoxic conditions.

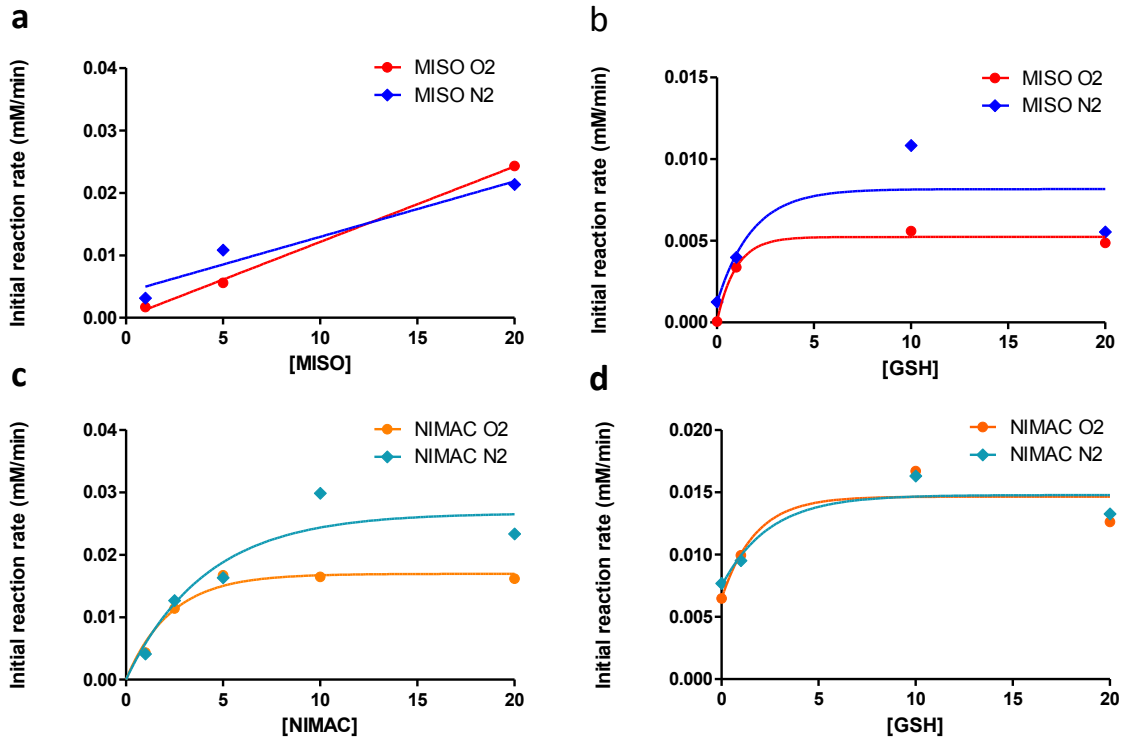

Figure 20. Influence of the initial concentrations of nitroimidazole and GSH in the reduction rate of the hypoxia marker in the presence of oxygen and under hypoxic conditions.

a) Initial reduction rate of MISO for different initial MISO concentrations. b) Initial reduction rate of MISO for different initial concentrations of GSH. c) Initial reduction rate of NIMAC analog for different initial concentrations of NIMAC. d) Initial reduction rate of NIMAC for different initial concentrations of GSH.

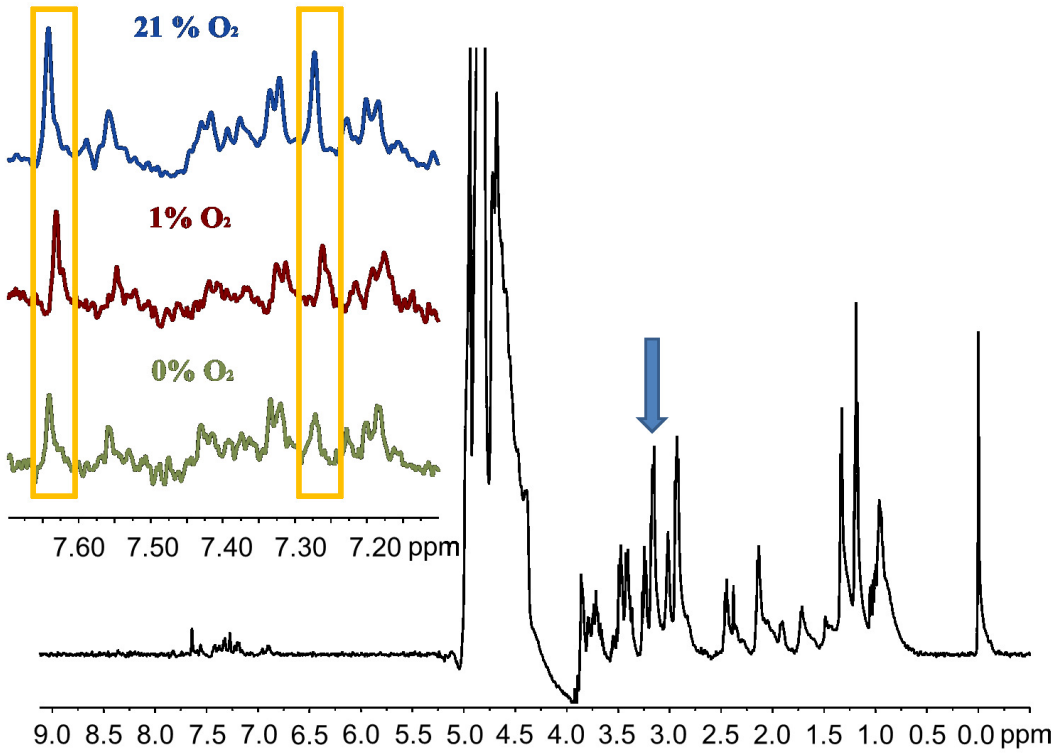

Figure 21. ^{1}H MR spectra of representative C6 cell pellets after six hours incubation with NISUCA under different oxygen tensions.

Blue arrow indicates total choline signal used for normalization. Insert shows an amplification of the spectral region (7.7 to 7.1 ppm) where NISUCA resonances (orange rectangle) appear. Normoxia (blue), hypoxia (red) and anoxia (green).

The amount of hypoxia marker remaining at the end of the incubation with C6 cells was quantified relative to total choline resonance (3.20 ppm, blue arrow in Figures 21 & 22), which did not change during the course of the experiment. A statistically significant decrease ($P < 0.05$, ONE way ANOVA) in the relative intensity of NISUCA resonances was found for decreasing oxygen tensions (Figure 23a). In the case of MISO, a decrease in the biomarker probe relative to choline was observed for decreasing oxygen tensions (Figure 23b), although it did not reach statistical significance ($P = 0.08$, one way ANOVA). NIMAC (Figure 23c) showed a statistically significant reduction ($P < 0.05$, t-test) in signal intensity when comparing normoxic and hypoxic conditions. Finally, PIMO showed a statistically significant difference ($P < 0.05$, one way ANOVA) between different incubation conditions (Figure 23d). In this case, it is important to remark that hypoxia caused a larger decrease in signal intensity than anoxia.

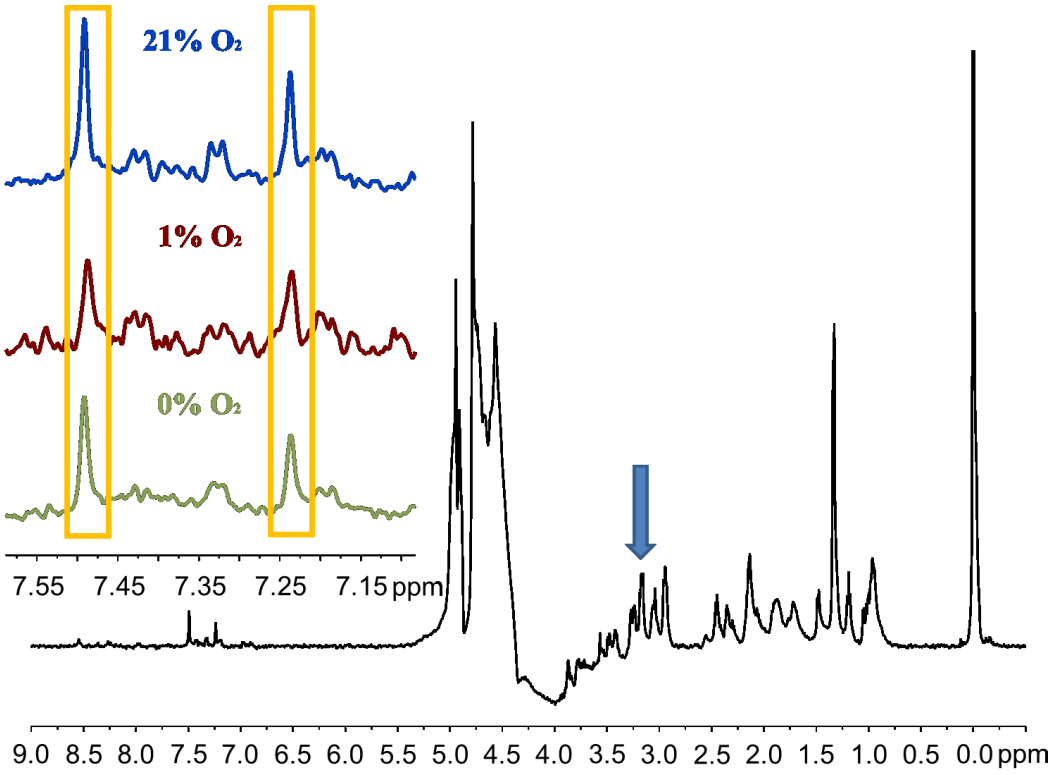

Figure 22. ^{1}H MR spectra of C6 cell pellet after six hours of incubation with PIMO under different oxygen tensions.
The blue arrow indicates the total choline resonance used for normalization. Insert shows a region of the spectra where PIMO resonances (orange rectangle) appear. Normoxia (blue), hypoxia (red) and anoxia (green).

To explore the influence of the redox state and GSH in the reduction rate of MISO in vivo, C6 cells grown to confluence were incubated under normoxic conditions with a special medium: DMEM without glucose, L-glutamine, phenol red, sodium pyruvate and sodium bicarbonate. This medium was supplemented with 2.5 mM MISO and i) 5 mM glucose (condition 1); ii) 5 mM glucose and 10 mM lactate (condition 2); iii) 5 mM glucose and 10 mM pyruvate (condition 3) and iv) 5 mM glucose

and 2 mM cystine (condition 4). ^{1}H HR-MAS spectra obtained from the cell pellets at the end of the incubations showed that MISO was clearly visible in conditions 1 and 2, whereas it depicted a much smaller signal intensities in conditions 3 and 4 (Figure 24a). The quantification was performed as described earlier using the total choline resonance as internal reference. Results showed marked changes in hypoxic marker content between the different incubation conditions (Figure 24b). Total GSH content in cells, measured in a separate cohort of pellets, indicated more than twice GSH concentration in cells in conditions 3 and 4 compared with conditions 1 and 2 (Figure 24c). There was a strong negative linear correlation ($R^2 > 0.97$) between the amount of MISO detected in the cell pellets and the total glutathione content (Figure 24d).

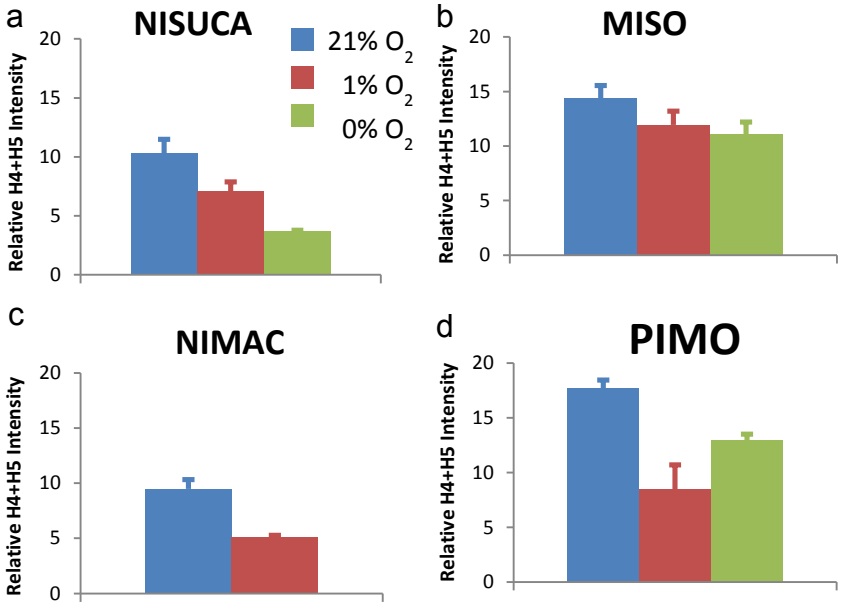

Figure 23. Influence of the environmental oxygen tension in the reduction rate of different hypoxia markers. Percentage of remaining NISUCA (a), MISO (b), NIMAC (c) and PIMO (d) resonances detected in pellets of C6 glioma cells, with respect to total choline, after 6 h of incubation under different oxygen tensions. Normoxia (blue), hypoxia (red) and anoxia (green). Lower oxygen tensions result in smaller amounts of probe remaining at the end of the reaction, revealing normally increased reduction rates for lower oxygen concentrations.

4.1.4. In vivo experiments

Finally, we aimed to investigate whether the combination of nitroimidazolyl derivatives and ^{1}H MRS could be used to detect changes in tumor oxygenation in vivo. For this purpose, we used a tumor model where C6 glioma tumors were grown in the flank of nude mice. This allowed the direct intratumoral injection of a mixture of MISO and TSP using a very fine needle (26G) to minimize tumor damage. TSP was employed as a reference molecule since it has a similar molecular weight (172.3 g/mol) than MISO (187.2 g/mol), appears far away from the MISO resonances (around 0 ppm) in the ^{1}H spectra where it is clearly detectable, and its in vivo behavior is not sensitive to oxygenation. Thus, its disappearance with time will provide a measurement of natural in vivo clearance of the

administered preparation. The hypoxia marker would suffer however, in addition to natural clearance, the disappearance due to in vivo reduction, the rate of which is oxygen dependent. Tumor oxygenation was modified by changing the proportion of oxygen in the anesthetic carrier gas breathed by animals: 100% O_2 in group 1 or hyperoxic condition; 21% O_2 (air) in group 2 or normoxic condition and a mixture of 10% O_2 and 90% N_2 in group 3 or hypoxic condition.

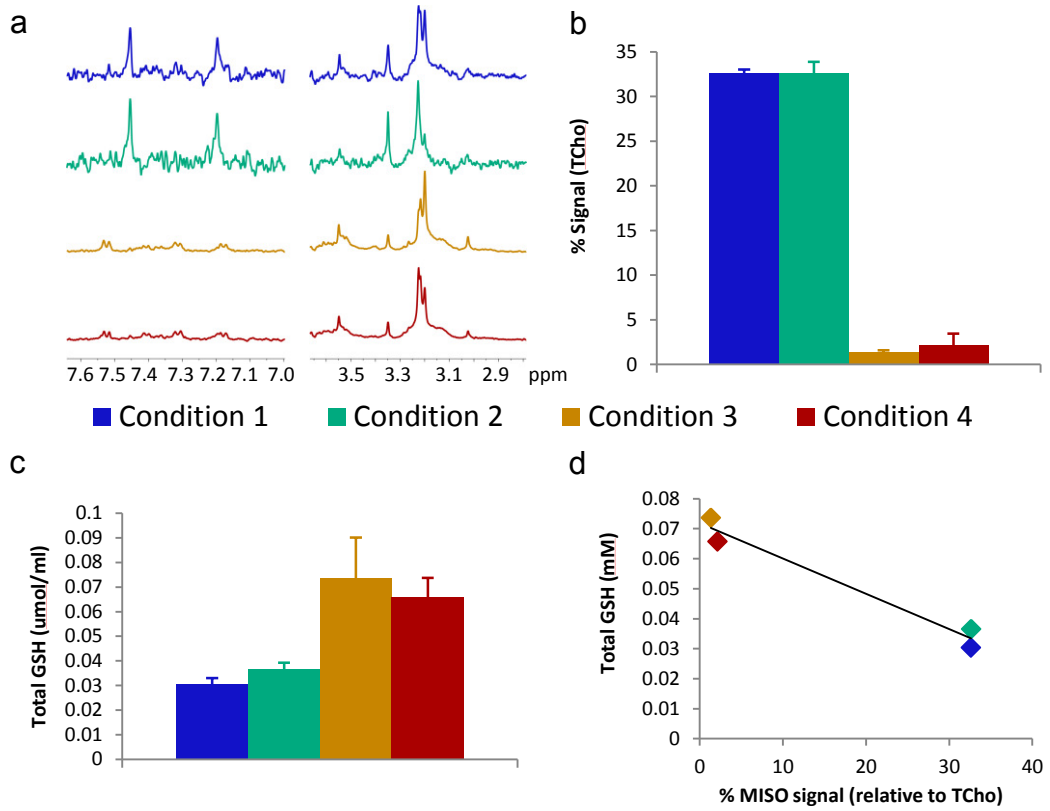

Figure 24. Influence of redox state in the reduction rate of hypoxic markers.
The redox state of C6 glioma cells was manipulated by incubating the cells with DMEM without glucose, L-glutamine, phenol red, sodium pyruvate and sodium bicarbonate but containing 2.5 mM MISO and either i) 5 mM glucose (condition 1, blue); ii) 5 mM glucose and 10 mM lactate (condition 2, green); iii) 5 mM glucose and 10 mM pyruvate (condition 3, yellow) and iv) 5 mM glucose and 2 mM cystine (condition 4, red). a) Representative regions of the ^{1}H-MR spectra of cell pellets 24 h after of incubation showing MISO (left) and total choline (right) signals. b) Percentage of MISO, with respect to total choline, detected in after the incubation in different redox states. c) Reduced glutathione content after incubation. d) Negative correlation between MISO and GSH measured in C6 pellets (r^2= 0.9679).

TSP (purple) and MISO H_a and H_b resonances (orange) were clearly detected using localized ^{1}H MRS PRESS after intratumoral injection (Figure 25a). Signal intensity of the hypoxia marker (orange) and reference compound (purple) decreased with time (Figure 25b) whereas the methylene resonances from lipids (blue) did not change significantly during the entire experimental time. On these grounds, MISO and TSP resonances were quantified relative to the methylene lipid signals. Under these conditions, MISO's and TSP's resonances decreased following apparent first order kinetics (Figure 25c).

In analogy to previous hypoxia measurements with fluorinated nitroimidazoles (4), we calculated for each animal the percentage of the remaining signal one hour after the injection with respect to the signal intensity detected immediately after the administration of the probe. When comparing these values in the different groups of animals, the percentage of remaining MISO decreases ($P > 0.01$, one way ANOVA) with the percentage of oxygen in the breathing gas (Figure 26). There was also a small decrease in TSP signal with decreasing oxygen content in the breathing gas, but these changes did not reach statistical significance ($P = 0.46$). When comparing percentage of remaining compound at the end of experiment between MISO and TSP, they turned out to be very similar for the hyperoxygenated group (Figure 26). Differences between both compounds increased in normoxic group and are more accentuated in hypoxic group.

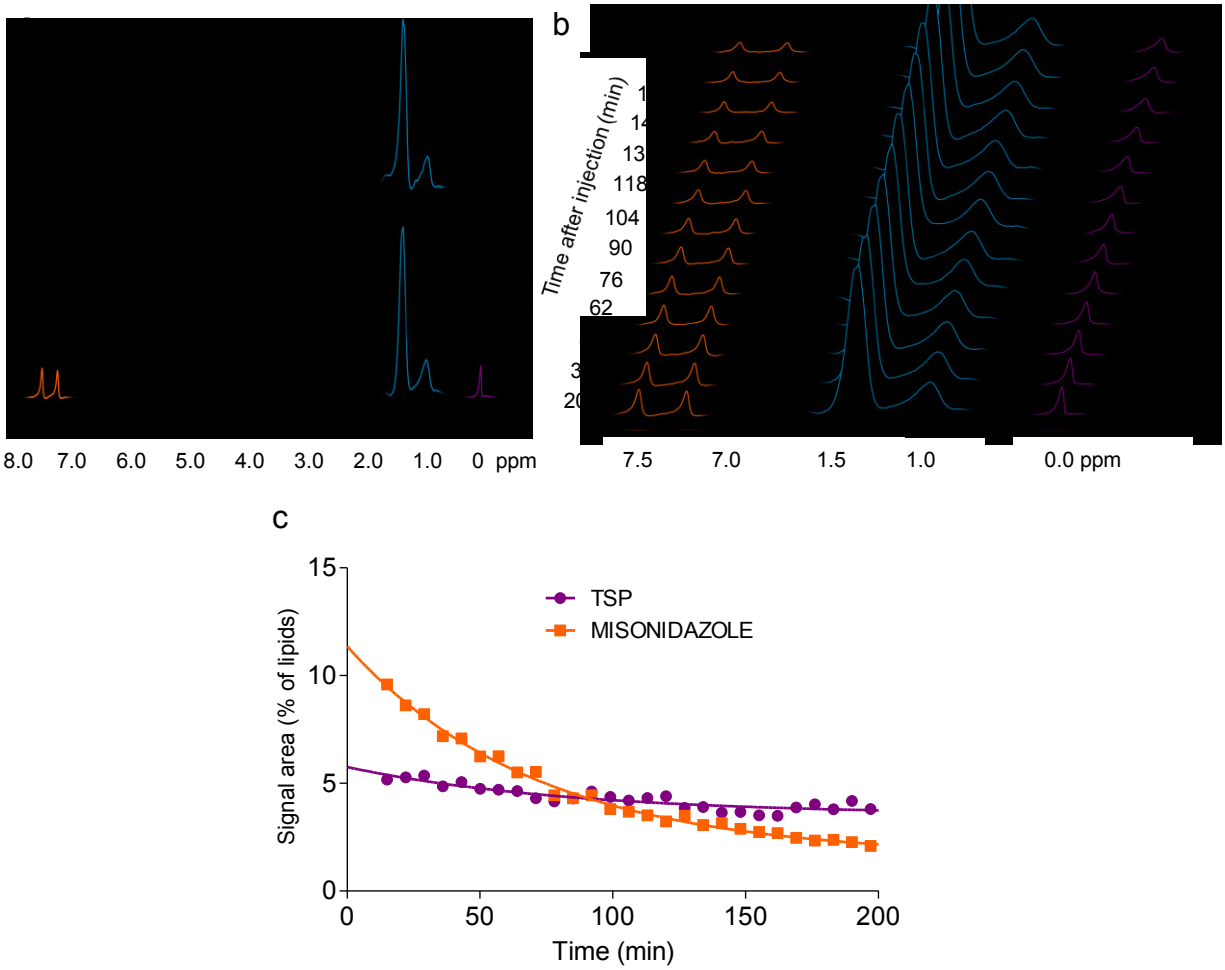

Figure 25. In vivo time course of MISO and TSP disappearance after intratumoral injection.
a) PRESS spectra of the C6 cell implanted tumor obtained before (top) and after (bottom) the injection (multisite) of a mixture of MISO (orange) and TSP (purple). Lipids signal are marked in blue. b) Time course of disappearance of MISO and TSP resonances as detected with ^{1}H MRS PRESS. c) In vivo monoexponetial decays of the MISO and TSP resonances, relative to the methylene lipid resonance.

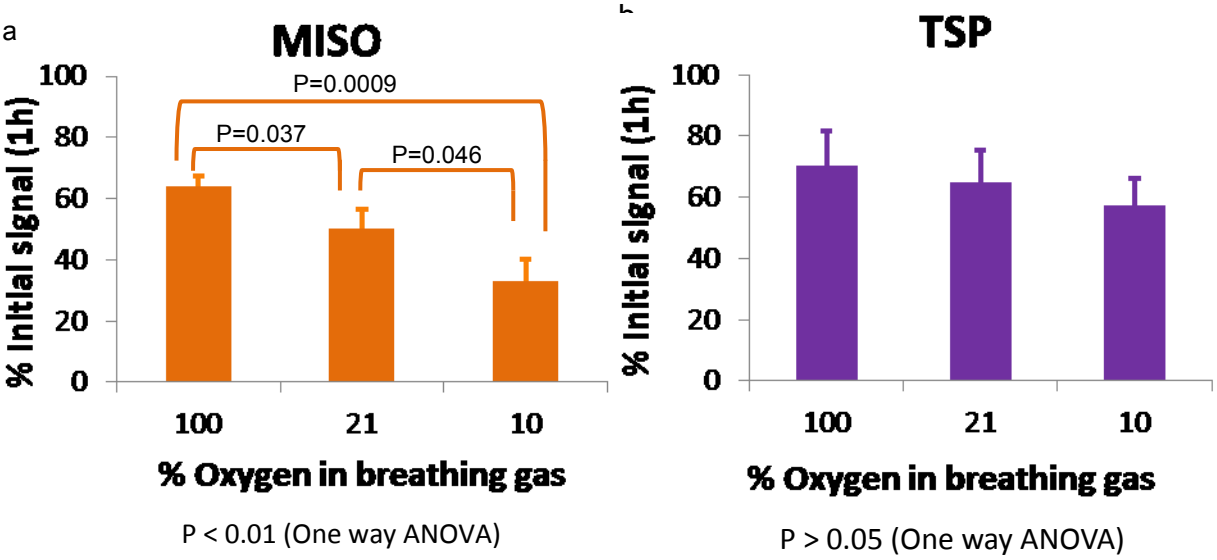

Figure 26. MISO and TSP disappearance in vivo.
Amount of MISO (a) and TSP (b) remaining in the tumor (median values) at one hour relative to the amount detected immediately after the injection of the compounds in hyperoxigenated (100% O_2), normoxic (21% O_2) and hypoxic (10% O_2) tumors.

Nevertheless, it is widely accepted that tumors present highly heterogeneous pO_2 distribution, highlighting the importance of spatial information. To this end, maps of the MISO and TSP percentage remaining 70 min after injection were calculated by acquiring multivoxel spectroscopy data of tumors treated as previously described for animal breathing pure oxygen and air (Figure 27). Obtained values were similar to those found with single voxel spectroscopy. Tumors depicted statistically significant differences in the percentage of MISO signal remaining in animal breathing pure oxygen (mean = 78 ± 1) and air (mean = 58 ± 1), whereas it was not the case for the % of TSP (mean = 72 ± 2 in both cases (Figure 28). As we observed with single voxel spectroscopy, the percentage of remaining compound between MISO and TSP turned out to be similar under hyperoxic conditions while differences were more accentuated in normoxic situation. On these grounds it seems reasonable to propose that maps of MISO intensity at different oxygen tensions provide a suitable indicator of the local tumoral oxygenation. It is also important to remark that there is no spatial correlation for the values obtained for MISO and TSP in a voxel by voxel way

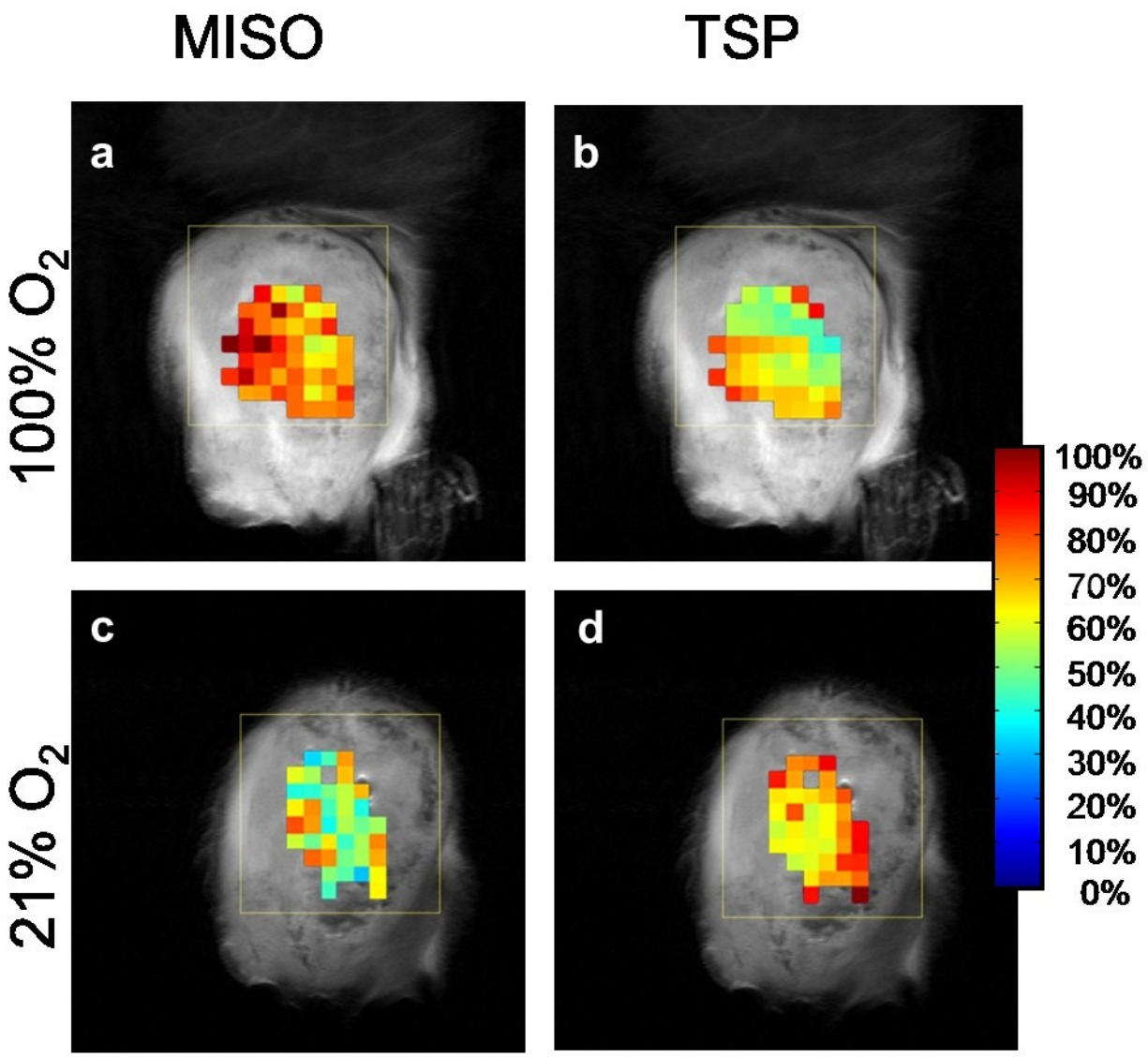

Figure 27. Maps of in vivo evolution of MISO and TSP.
Percentage of MISO and TSP remaining in the tumor at 70 minutes relative to the amount detected 30 minutes after intratumoral injection: a) % of MISO in animal breathing pure oxygen. b) % of TSP in animal breathing pure oxygen. c)% of MISO in animal breathing air and d) % of TSP in animal breathing air.

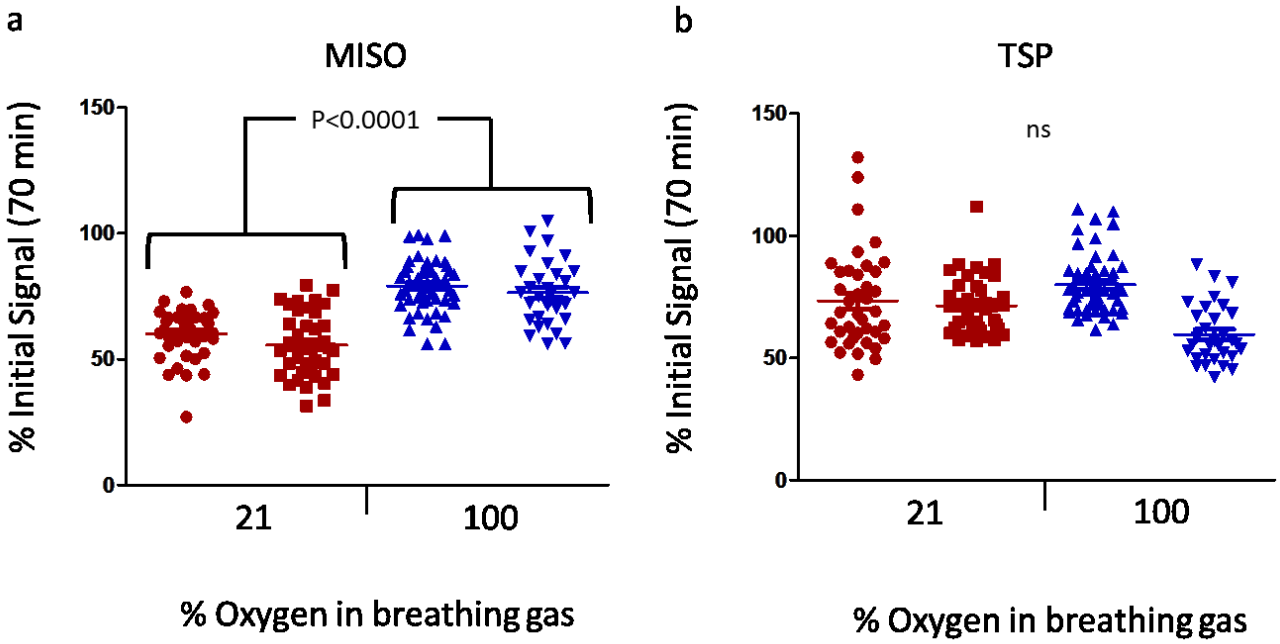

Figure 28. MISO and TSP disappearance in vivo by ^{1}H MRSI.
Scatter plot of the amount of MISO (left) and TSP (right) remaining in the tumor at 70 minutes relative to the amount detected 30 minutes after the injection of the compounds in hyperoxygenated (blue) and normoxic (red) tumors.

4.2. Endogenous contrast agents as detected by MRI

The spectroscopy method described above is not devoid of limitations including the mandatory use of an external contrast agent, the need of direct intratumoral injection and the reduced temporal and anatomical resolution. To overcome these shortcomings, we implemented a novel imaging approach to monitor the response of tumors to pO_2 modulation. We proposed to take advantage of the paramagnetic properties of molecular oxygen and deoxyhemoglobin as surrogate markers of tumor pO_2. Molecular oxygen acts as a T_1 contrast agent whereas deoxyhemoglobin behaves as a T_2* contrast agent. The method developed here improved considerably many of the limitations of the spectroscocopic approach, including higher temporal and spatial resolution, avoiding the administration of the exogenous probe. Briefly, two rat prostate tumor types, noted for differential growth rates, vascular development and oxygenation (25,227), were employed as models. Both T_1 and T_2* values and SI in T_1W and T_2*W images were compared while the animal model breathed air or carbogen in vivo.

4.2.1. BOLD and TOLD

During air breathing (baseline), MRI SI was generally stable (mean ΔSI in T_2*W and T_1W images were very similar, the differences being less than 1%, Figures 29-32), despite considerable heterogeneity, particularly in T_2*W images (Figure 33). Increased SI in T_2*W images was usually significant within 30 seconds after switching gases, normally reaching a stable plateau within two minutes for both small and large HI tumors and small AT1 tumors (Figures 29-31, a-c). Large AT1 tumors often showed a transient increase with return to baseline after two to six minutes (Figure 32c). BOLD response to carbogen was heterogeneous with focal signal changes ranging from plus 100% to minus 40% respect to baseline SI, but the mean value for each adjacent slice was quite uniform (Figures 29-32 c). T_1W signal response was considerably smaller under these data acquisition parameters and the response tended to be slower, but remained still significant (Figures 29-32, d-f).

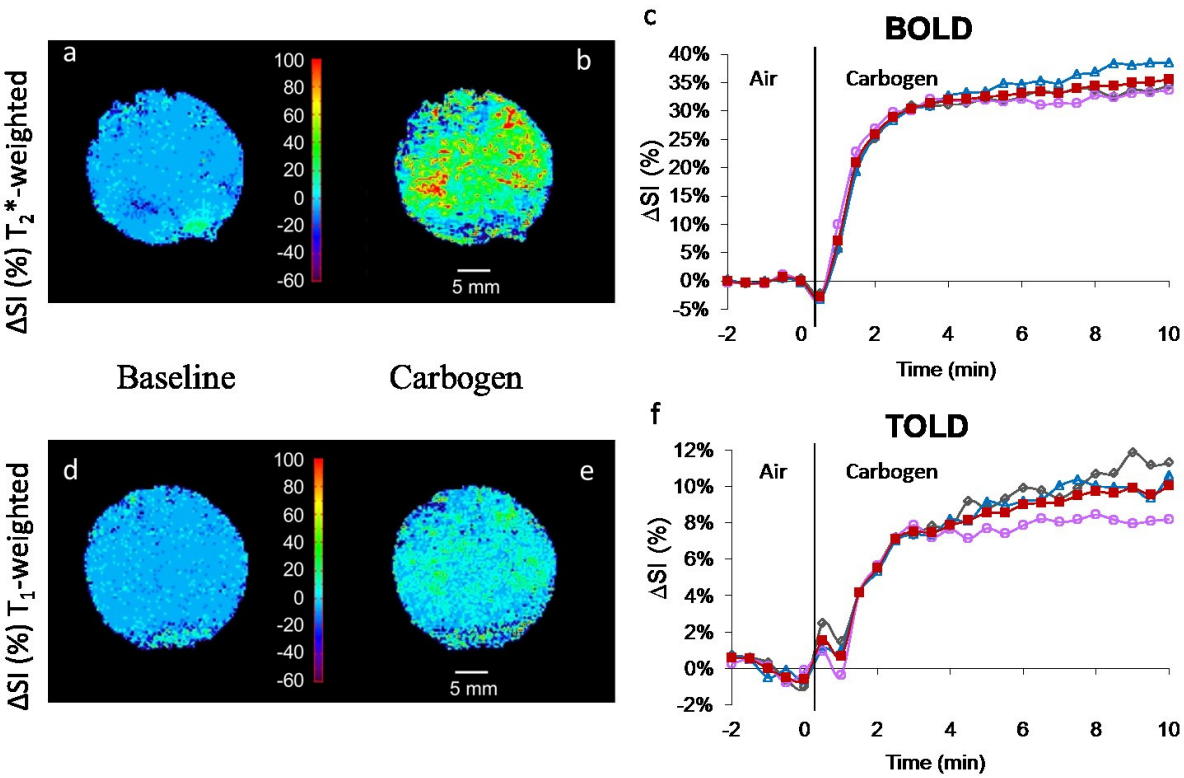

Figure 29. Response of T_1- and T_2*-weighted image signal intensity to carbogen challenge in a small Dunning prostate R3327-HI tumor.

Normalized spin echo planar T_2*W cross-sectional images of a representative tumor acquired while breathing (a) air (baseline), and (b) carbogen (image selected to show maximum change). c) Mean BOLD (normalized SI) response in three adjacent image slices (o, Δ,◇) and mean over whole tumor (■). Corresponding normalized T_1W gradient echo images of the tumor acquired breathing (d) air and (e) carbogen. f) Mean variations across the tumor of normalized ΔSI vs. time (TOLD response). Heat scale bar shows % increase or decrease and linear scale = 5 mm. Tumor size = 2.1 cm^3

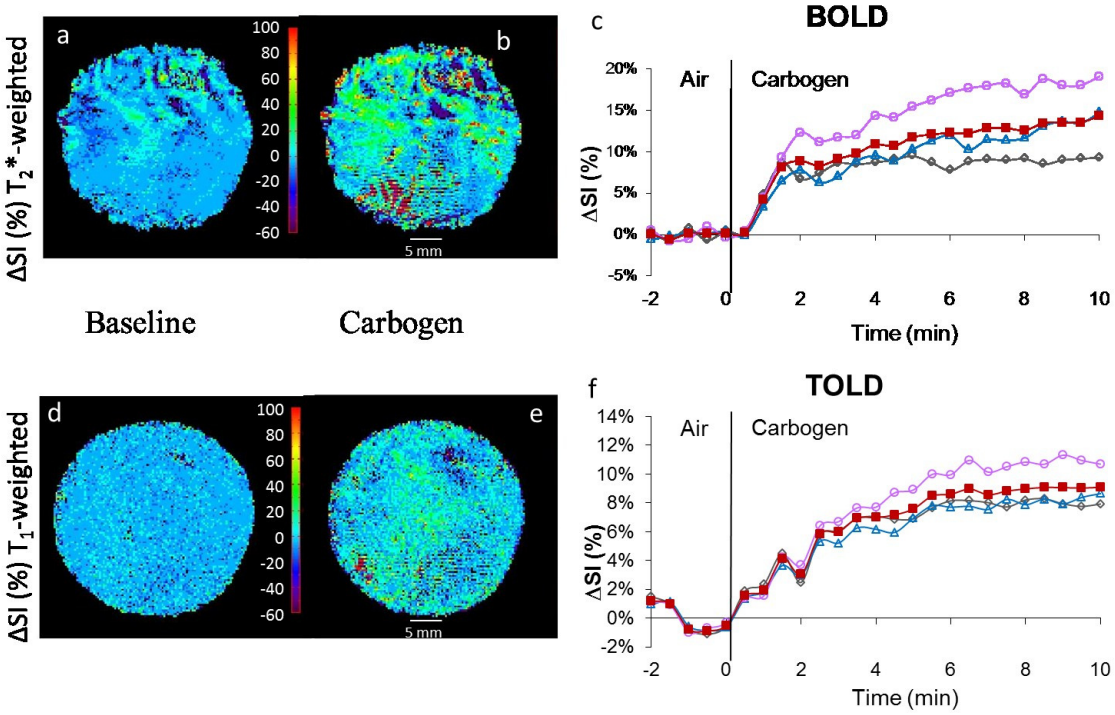

Figure 30. Signal response to carbogen challenge in a large Dunning prostate R3327-HI tumor.

Data correspond to Figure 29 but for a larger HI tumor (5.7 cm^3). The BOLD response was significant, but considerably lower than in the smaller HI tumor, whereas the TOLD response was quite similar to smaller tumors.

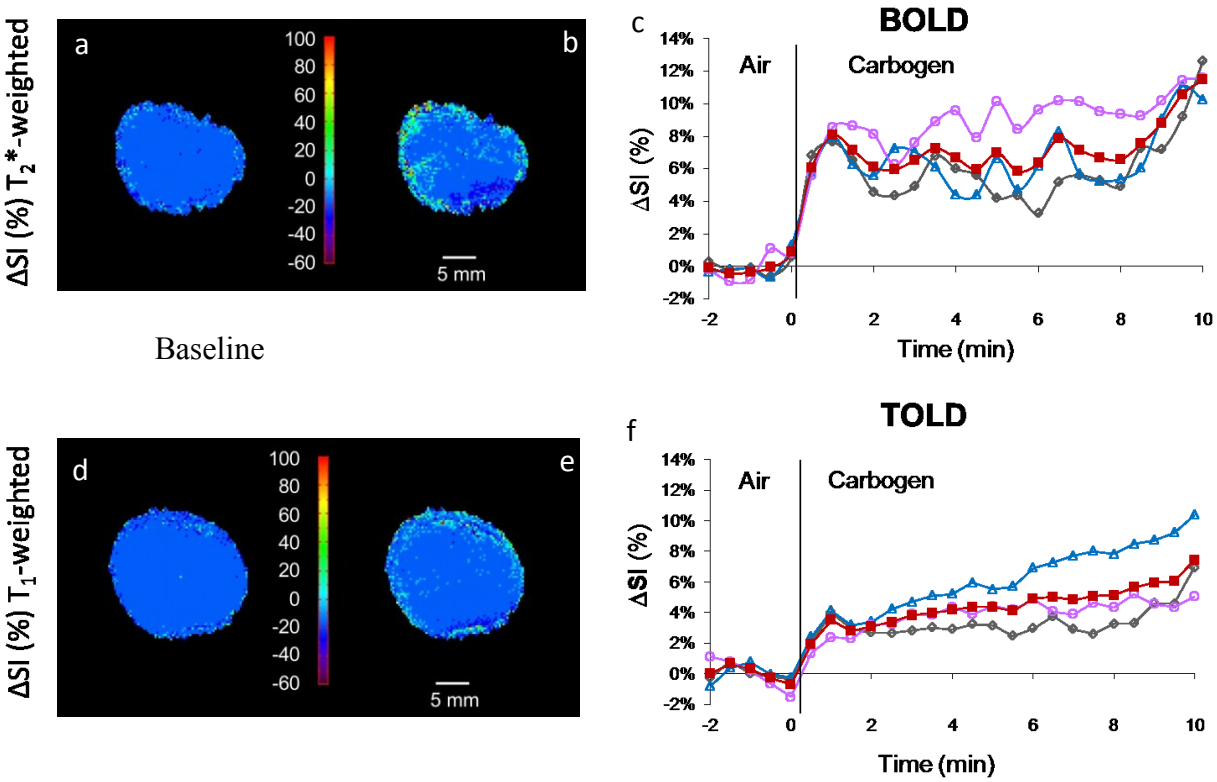

Figure 31. Signal response to carbogen challenge in a small Dunning prostate R3327-AT1 tumor.
Data correspond to Figure 29, but in a smaller AT1 tumor (0.75 cm^3). The BOLD and TOLD responses were both considerably lower than in the smaller HI tumor.

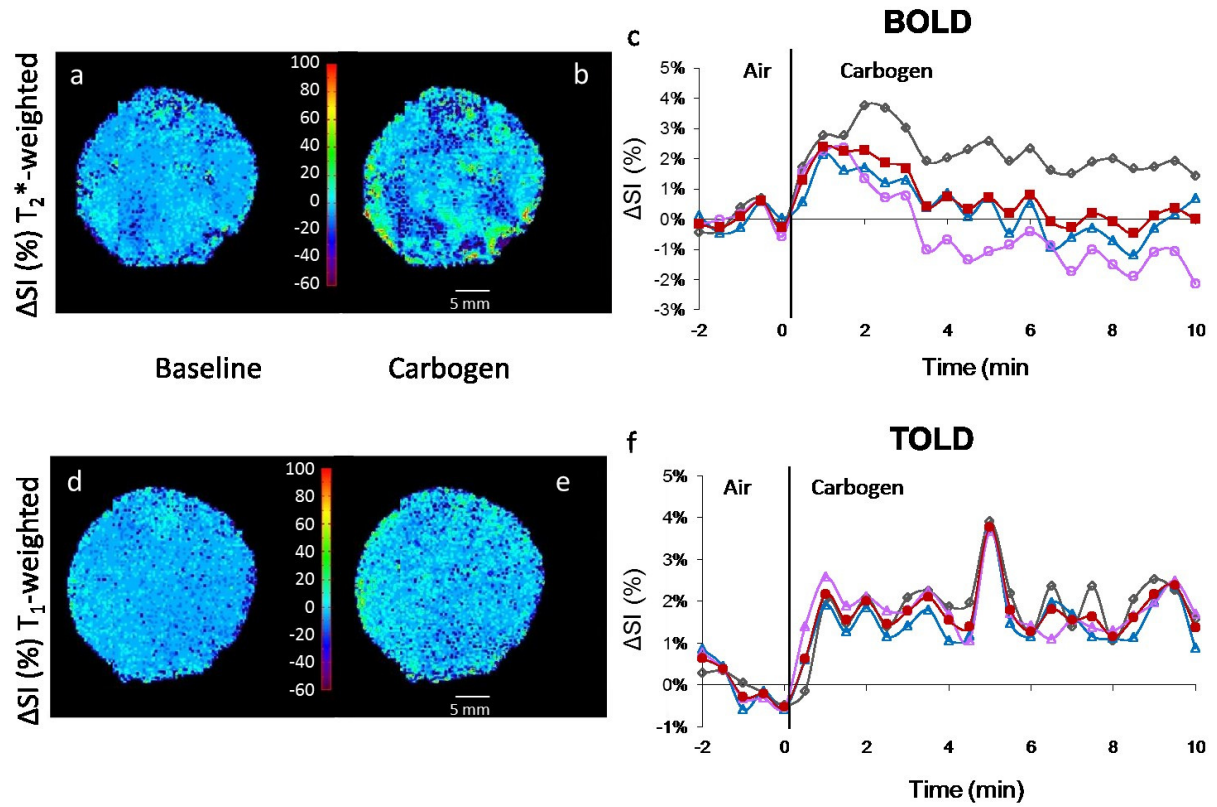

Figure 32. Signal response to carbogen challenge in a large Dunning prostate R3327-AT1 tumor.
Data correspond to Figure 29, but in a larger AT1 tumor (5.8 cm^3). The BOLD and TOLD responses were each considerably smaller than in the other tumors.

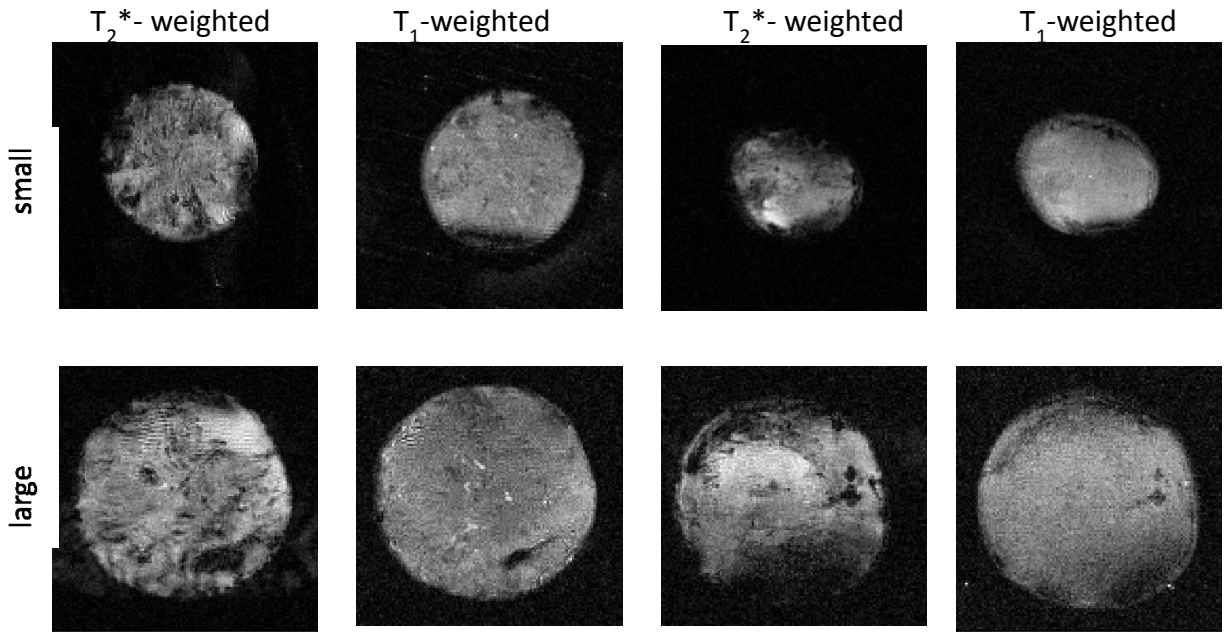

Figure 33. ^{1}H MRI of Dunning prostate tumors.
Representative baseline T_2*W and T_1W images are shown for each tumor type. Images: Upper row shows small tumors and lower row large tumors.

Small HI tumors generally showed the largest BOLD response with mean signal increase ranging from 6 to 57% within 1 minute of changing gas and settling on a plateau of 4% to 66% enhancement (mean 21 $\pm$ 7%, Table 8), as shown for a typical tumor (Figure 29 a-c). TOLD response was smaller and initial rapid response was followed by continued increase over 10 minutes reaching 4 to 16 % (*e.g.*, Figure 29 d-f). The mean response of three adjacent image slices was highly consistent (Figure 29f). Large HI tumors showed a smaller T_2*W response (Figure 30c), but T_1W response (3 to 9%) approached that of the smallest tumors (Figures 29 & 30 f). Small AT1 tumors responded rapidly in both T_1W and T_2*W images with little further change after 2 minutes. There was obvious heterogeneity with greatest response close to the tumor periphery in both T_1W and T_2*W images (Figure 31). Large AT1 tumors showed particularly small BOLD and TOLD response (Figure 32 c & f).

Each tumor type showed highly consistent responses and mean time courses are presented for both BOLD and TOLD experiments (Figure 34) and summarized in Table 8. Noting the initial rapid dynamic response leading to stable plateau, the data in Table 8 show the mean values for ΔSI considering only the last ten measurements during carbogen breathing. Mean changes in SI T_1W and T_2*W images of small HI tumors (known to be well oxygenated) were significantly greater than in small or large AT1 tumors ($p<0.05$). The T_1W image response was also significantly different between large HI and large AT1 tumors (Table 8).

Table 8. BOLD and TOLD signal responses to carbogen challenge in groups of Dunning prostate R3327 tumors of different sizes.

Tumor	BOLD (%ΔSI) / range	TOLD (%ΔSI) / range
Small HI (n=8)	21 ± 7 [a] / 0.4-65%	8 ± 1 [a] / 4-16%
Small AT1 (n=9)	8 ± 2 / 0.6-20%	4.5 ± 0.9 / 1-8%
Large HI (n=5)	7 ± 1 / 4-13%	5 ± 2 [b] / 3-9%
Large AT1 (n=7)	± 0.7 / -0.6-5.6%	± 0.3 /0.7-2.7%

[a] p<0.05 versus small and large AT1; [b] p<0.05 versus large AT1.

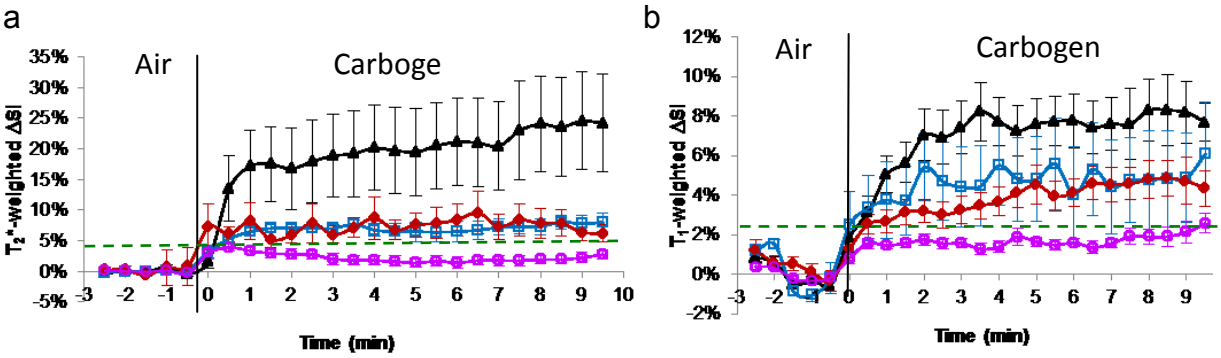

Figure 34. Comparison of BOLD and TOLD response in groups of Dunning prostate tumors.
a) Dynamic normalized T2*W signal response to carbogen challenge in the four different groups of tumors. b) Corresponding T1W signal responses. ▲ (small HI; n= 8), ◆ (small AT1; n= 9), ☐ (large HI; n= 6), o (large AT1; n= 7).

T_1W and T_2*W signal responses were well matched with a general trend of larger TOLD response being associated with larger BOLD response (Figure 35a). Considering the 29 tumors, where T_1W and T_2*W signal responses were evaluated, the linear correlation coefficient showed R^2>0.75 (p<0.0001), which strengthened considerably for HI tumors alone (R^2>0.85), although it was weaker for AT1 alone (R^2>0.53).

4.2.2. R_1 and R_2* changes during hyperoxigenation

To investigate the origin of the changes in SI, R_1 and R_2* maps, we evaluated 27 tumors during air and CB breathing (Figure 36 & 37) and the corresponding mean values are presented in Table 9. R_2* ranged from 28 to 108 s^{-1} and changed significantly for many individual tumors, although did not become significant among the groups of tumors (Table 9). There was a correlation between ΔSI in T_2*W images and ΔR_2* irrespective of tumor type and size (R^2>0.48), which improved to R^2>0.55 for AT1 tumors alone. A very similar result was observed if the percentage change in R_2* was considered instead of the absolute ΔR_2* value. Baseline R_1 ranged from 0.389 to 0.711 s^{-1} (Table 9). No apparent

correlation was found between ΔSI in T_1W signal and ΔR_1 (R^2<0.1 for each tumor type). A strong correlation was observed for ΔR_1 vs. ΔR_2* for HI tumors (R^2>0.67), but AT1 tumors showed no obvious trend (R^2<0.25; Figure 35b). R_1 and R_2* values were very tightly correlated during CB and air breathing , as expected since changes in relaxation values due to hyperoxigenation were relatively small (*e.g.*, $R_2*_{(AT1)}$ R^2>0.98; $R_{1(AT1)}$ R^2>0.98; $R_2*_{(HI)}$ R^2>0.71; $R_{1\,(HI)}$ R^2>0.8). Mean R_1 and R_2* values were not significantly different except for big HI tumors, as shown in Table 9.

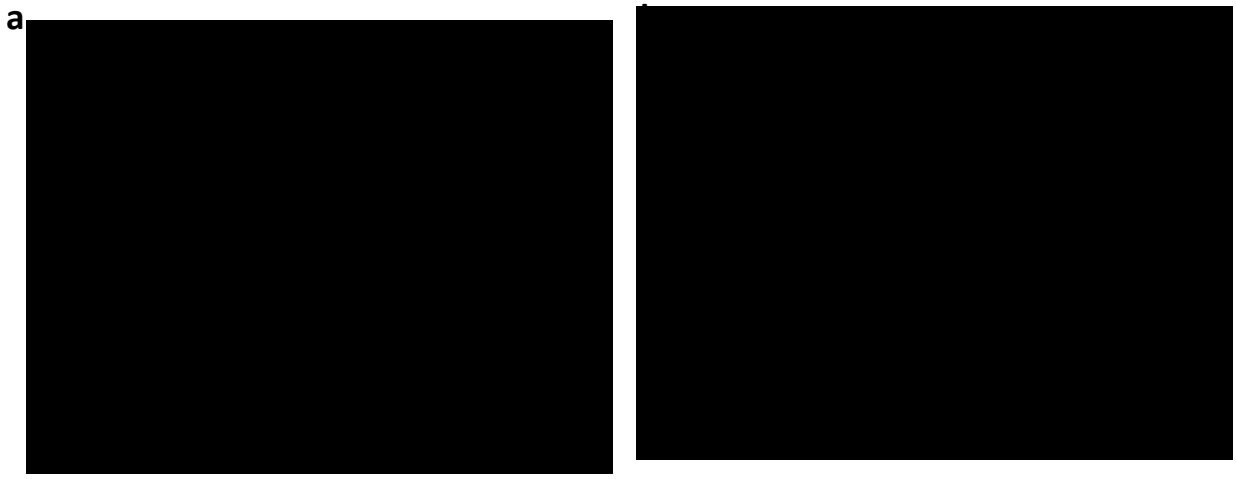

Figure 35. Correlation of TOLD and BOLD response to carbogen challenge.
Comparison of AT1 (●) and HI (Δ) tumors showed distinct trends for the group of 29 tumors. a) Signal enhancement showed a linear correlation for all tumors (R^2>0.75), which was even stronger for HI tumors alone (R^2>0.85). b) Mean change in R1 was closely reflective of R2* for HI tumors (R^2>0.67), but showed no obvious relationship for the AT1 tumors.

Table 9. Mean relaxation rates in groups of tumors to breathing air or carbogen

Tumor (n)	R_2* air	R_2* CB	ΔR_2*	R_1 air	R_1 CB	ΔR_1
HI (small) (5)	66.5 ± 6.5 [c] (42-82)	65.5 ± 7.8 [a] (42-85)	-1.1	0.45 ± 0.02 (0.39-0.51)	0.45 ± 0.02 [a] (0.41-0.51)	0.005
HI (large) (8)	43.9 ± 4.4 (34-72)	38.4 ± 2.0 (34-48)	-5.5	0.51 ± 0.01 (0.47-0.46)	0.55 ± 0.01 (0.46-0.61)	0.039
AT1 (small) (8)	64.4 ± 7.9 [a] (28-108)	64.3 ± 8.3 [a] (27-110)	-0.1 [a]	0.52 ± 0.04 (0.44-0.71)	0.51 ± 0.03 (0.41-0.65)	-0.007 [a]
AT1 (large) (5)	56.3 ± 4.7 (44-69)	58.2 ± 4.6 [a] (44-70)	1.9 [a]	0.46 ± 0.03 (0.41-0.53)	0.46 ± 0.03 [a] (0.42-0.54)	0.001 [a]

($\Delta R = R_{CB} - R_{air}$); all data presented as mean ± SE (s^{-1})with range in parentheses; (n) represents number of tumors; [a] p<0.05 vs. large HI tumors.

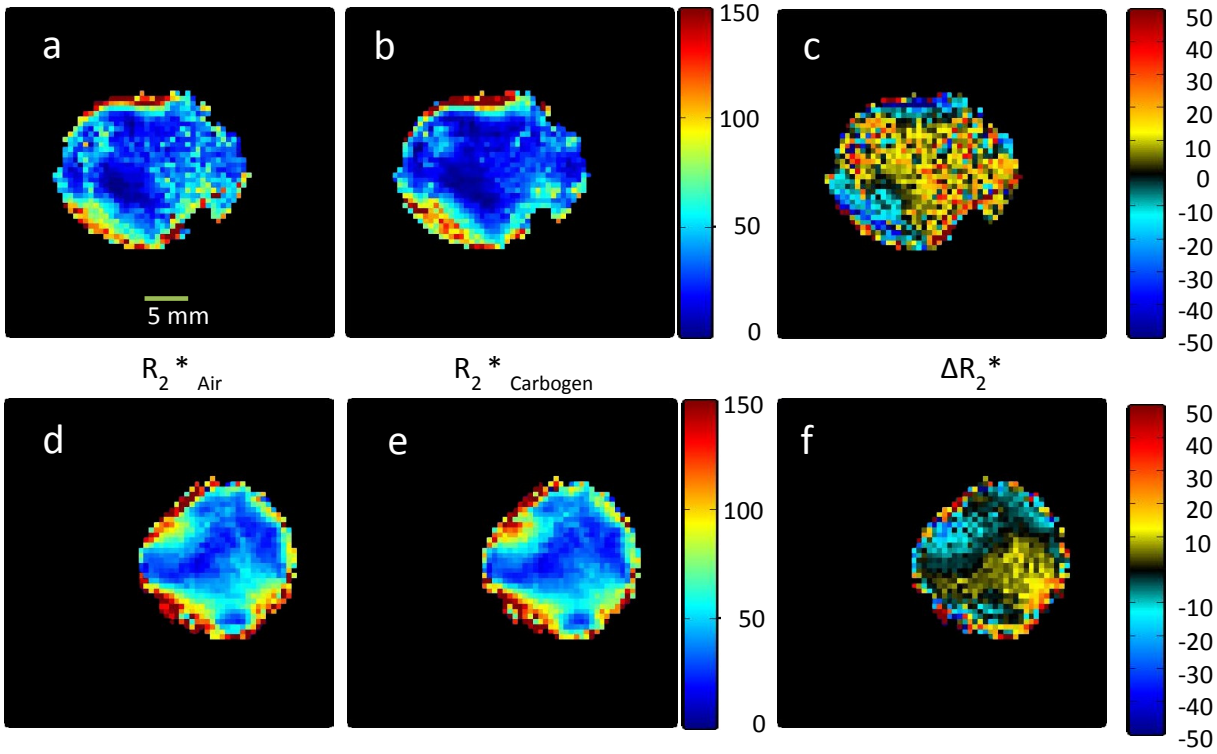

Figure 36. R_2* response to carbogen challenge.
R_2* maps of small HI (a-c) and large AT1 (d-f) tumors respectively, when the rats were breathing air (a, d) or carbogen (b, e), together with difference maps ΔR_2* (s^{-1}) = R_2*$_{Air}$ – R_2*$_{CB}$ (c, f).

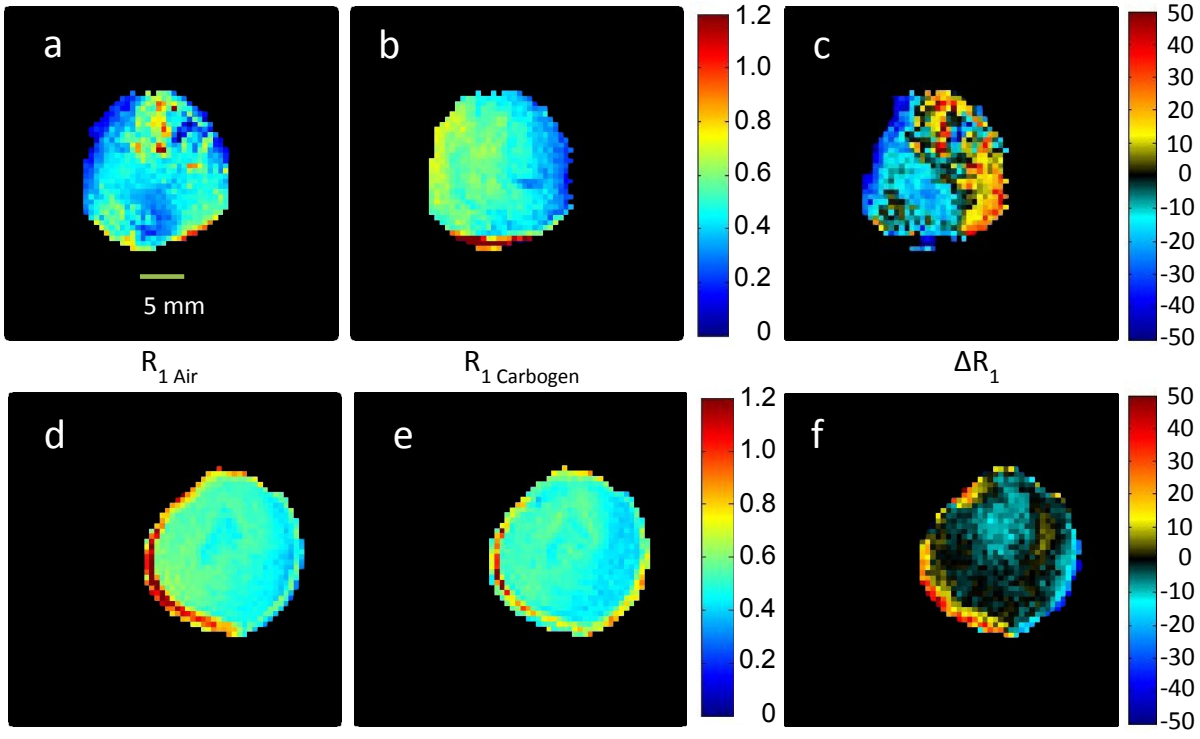

Figure 37. R_1 response to carbogen challenge.
R_1 maps of a small HI (a-c) and a large AT1 (d-f) tumor when the rats were breathing air (a, d) or carbogen (b, e) together with difference maps ΔR_1 (s^{-1}) = $R_{1\,Air}$ – $R_{1\,CB}$ (c, f).

4.2.3. Tumor stratification with DOCENT

There was little overlap between magnitude of BOLD and TOLD responses, as shown in the box and whisker plots (Figure 38) when tumors were stratified as Types 1 – 3 as indicated in methods, based on anticipated hypoxia and response to radiation. Since both Types 2 and 3 are expected to respond well to radiation with hyperoxic gas breathing, a further classification considered Type 1 versus all others (Types 2 and 3 combined) in an effort to correctly assign tumors to potential response groups (Table 10). Response thresholds were applied as Major (BOLD ΔSI>6% and TOLD ΔSI >3%) or Minor (BOLD ΔSI<6% and TOLD ΔSI <3%). All Type 1 tumors were correctly identified as hypoxic based on Minor signal enhancement. 8 out of 23 Type 2 or 3 tumors did appear to be hypoxic based on the BOLD threshold alone. However, the TOLD criterion left only 3 tumors as misidentified (apparently hypoxic), when actually responsive. If a 2% TOLD response was applied as the response threshold, then classification of responsive tumors improved, although now TOLD alone would misclassify some hypoxic tumors.

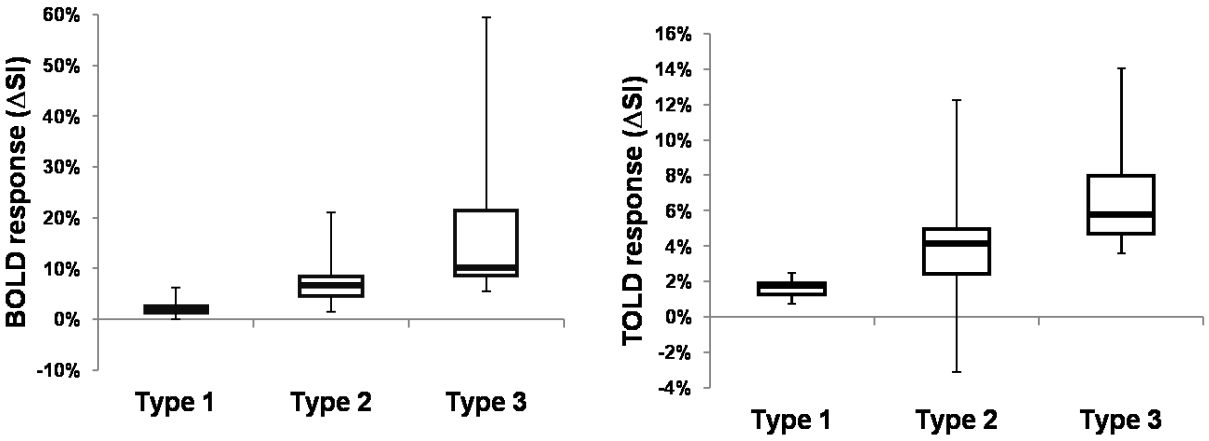

Figure 38. Stratification of tumors in terms of expected radiation response.
Type 3 tumors (small HI) are expected to show little hypoxia, large increase in response to breathing hyperoxic gas and good response to radiation. Type 2 tumors are expected to exhibit considerable hypoxia, which may be eliminated by breathing hyperoxic gas and hence generating good radiation response. Type 1 tumors are expected to be hypoxic and resist modulation by hyperoxic gas yielding poor radiation response. a) Stratification based on BOLD; b) Stratification based on TOLD.

Table 10. Predictive value for identifying tumor types.

Magnitude of response[a]	BOLD (T_2*W)		TOLD (T_1W)	
	Hypoxic[b]	Non-hypoxic or responsive[c]	Hypoxic[b]	Non hypoxic or responsive[c]
Major	0	14	0	19
Minor	7	8	7	3

[a] Major BOLD response threshold >6%; Major TOLD response > 3%

[b] Hypoxic tumors (Type 1) are those which exhibit large hypoxic fraction, low mean pO_2, do not respond to hyperoxic gas breathing and show no enhanced response to single high dose radiation, specifically large AT1 tumors, based on published reports (25,124,227).

[c] Non hypoxic or responsive tumors (Types 2 or 3) are those expected to have minimal hypoxic fraction or hypoxia, which is eliminated by hyperoxic gas breathing, and hence, these tumors respond to high dose radiation (25,124,227).

5. DISCUSSION

5.1. Nitroimidazolyl probes as hypoxia markers

Despite their applications in nuclear medicine and histochemistry, nitroimidazole derivatives have not been previously used as ^{1}H MR hypoxia markers. In particular, several ^{19}F nitroimidazolyl derivatives have been proposed previously as PET, ^{19}F-MRS and fluorescent histochemical probes for hypoxia. One of these molecules (SR-4554) entered recently in Phase I clinical trials (140-141). Nevertheless, the limited access to PET scanners and labeled radiofarmaceuticals, the usual lack of ^{19}F-MR capabilities in clinical scanners and the impossibility to use fluorescence bioimaging methods to examine deep regions in the human body, constitute important limitations to the widespread use of these compounds in the clinic. On these grounds, we decided to prepare here a new series of nitroimidazole derivatives that could be used in combination with more accessible preclinical and clinical ^{1}H-MR instrumentation.

5.1.1. Synthesis of new 2-nitroimidazole probes a hypoxic markers.

Based in the previous experience of our laboratories (19,58,199), we choose to synthesize nitro analogs of the pH indicator ISUCA (2-(imidazol-1-yl)succinic acid) due to its favorable pharmacokinetic properties. However, the addition of 2-nitro-1*H*-imidazole to diethyl fumarate, under the conditions previously reported (62) did not yield the expected Michael adducts. We implemented then an alternative synthetic approach, as depicted in Scheme 2. It was not possible to obtain compound **5** in pure form, but compound **4** (NISUCA) was obtained in relatively high yield and was therefore further tested as a potential hypoxia marker. We also synthesized on our own and further investigated as an hypoxia probe methyl 2-(2-nitro-1H-imidazol-1-yl)acetate (NIMAC), the synthesis of which had been previously reported (115), but not used, to our knowledge, as a hypoxia probe.

It is widely accepted that the biological activity of nitroimidazoles is dependent upon the reduction of the nitro group, a process originating the active species able to combine with biomacromolecules forming adducts that accumulate in the hypoxic environments (218). The first step consists of the single-electron reduction of the nitro group. Hence, the initial steps in the evaluation of NISUCA and NIMAC, as pO_2 indicators, included the determination of their redox potential by cyclic voltammetry methods, using the corresponding 2-nitroimidazole **1** as a reference. We found a reduction potential of -0.511 V and -0.615/-1.138 V for NISUCA, in aprotic and protic medium, respectively (Table 6). These reference values were compared with those determined in the literature for other nitroimidazolyl derivatives (24), finding similar values to the other hypoxia markers in the case of NIMAC but not for NISUCA (Table 11). The differences found for NISUCA may be related to the different parameters assayed ($E_{1/2}$ vs E respectively) and experimental conditions used in the

previous measurements (pH, aprotic medium, reference electrodes...). Notably, the use of hypoxia markers depicting different reduction potentials allowed us to investigate for the first time the relevance of this thermodynamic property in the in vitro and in vivo reduction rates of this type of compounds, comparing the obtained in vitro and in vivo reduction rate with their reduction potential.

Table 11. Reduction potential of different nitroimidazole derivatives used as hypoxia markers.

Compound	Parameter	pH	Value (mV)	Reference
NISUCA	$E_{1/2}$ [a]	7.2	-551	(155)
2-Nitroimidazole	E [b]	7.0	-418	(217)
Misonidazole	$E_{1/2}$	7.2	-395	(150)
	E	7.0	-389	(217)
Misonidazole analog	E	7.0	-389	(217)
NIMAC	E	7.0	-355	(217)
Pimonidazole	E	7.0	-352	(217)
NADPH	E	7.0	320	(17)
GSH	E	7.0	240	(177)

[a] $E_{1/2}$: half wave potential. [b] E: reduction potential

Table 11 indicates that all nitroimidazolic compounds depict in all cases more negative redox potentials than NADPH or GSH and are therefore suitable electron acceptors from these physiological electron donor molecules. However, we have shown that the presence of the nitroimidazolil derivative and NADPH or GSH, does not lead to an appreciable reduction of the probe, indicating that the different reduction reactions are not controlled thermodynamically by uncatalized electron transfers, but require the participation of an enzyme to control kinetically the reduction process.

5.1.2. Main determinants of the enzymatic reduction of 2-nitroimidazole derivatives used as hypoxic markers.

Once established that the control of the reduction rate involved kinetic, rather than thermodynamic control, we proceeded to investigate in more detail the determinants of the reduction rate of nitroimidazolyl derivatives. We performed a wide series of kinetic studies under different incubation conditions using initially a cell free, relatively simple, enzymatic reduction system. There is a large panel of enzymes that may be responsible of the nitroimidazole bioreduction; NADPH:cytochrome P450 reductase, cytochrome P450, xantine oxidase or DT-diaphorase. Joseph et al. (91) overexpressed P450ase and DT-diaphorase in monkey kidney cells. They found that 80 times augmented P450ase activity correlated with 5 to 7 fold increase in 2-nitroimidazole binding, whereas 1000 fold activity increase of DT-diaphorase only correlated with a 1.5 growth in 2-nitroimidazole

binding. Aboagye et al. (3) used mouse liver microsomes and found that nitroimidazole reduction was markedly inhibited in air, in the absence of NADPH and in the presence of a P450ase inhibitor ($TlCl_3$ $4H_2O$). Taken together, these evidences indicated that P450ase is the dominant enzyme involved in the in vivo reduction of nitroimidazol based hypoxia markers, although it may not the only one (3). We decided, thus, to implement the P450ase system to investigate in vitro, in a cell free system under highly controlled conditions, the kinetic mechanism underlying the reduction of nitroimidazoles.

At this point, it could be asked whether the differences in nitroreductase levels could be important factors determining the variations in nitroimidazole reduction and retention in tumor, rather than the environmental oxygen tension. However, a large study compared P450ase activity in 69 tumor cell lines (54), and found only relatively low activity for this enzyme compared with other reductases as DT-diaphorase and small variations across the different cell lines. Aboagye et al. (3) compared P450ase activity in mouse liver and various mouse and human tumors. It was high in liver microsomes but low and relatively constant (only 3-fold variation) in different tumors. These results suggest that the small variations in nitroreductase levels are not the main determinants of the large variations in nitroimidazole bioreduction observed in vitro and in vivo.

Remarkably, our results showed that the oxygen tension by itself had also a small influence in the observed reduction rate of nitroimidazoles, whereas the GSH levels had a strong influence, increasing the rate of nitroimidazole reduction very significantly (Table 12). Based on our spectroscopic measurements, we propose that this increase in the reduction rate is mediate through the formation of an intermediate between nitroimidazole derivative and GSH. Furthermore, this adduct is formed through the union of the thiol group of GSH and either the imidazole ring or the nitro moiety of the probe.

Table 12. Relative reduction rate constant of hypoxia markers.

Hypoxic marker	Condition					
	Normoxia	Anoxia	Normoxia + GSH	Anoxia + GSH	Normoxia + GSH + GR	Anoxia + GSH + GR
MISO	-0.7 ± 0.7	-1.0 ± 0.9	-15.8 ± 0.6	-16.7 ± 0.9	-13.7 ± 0.6	-12.7 ± 0.5
PIMO	-0.3 ± 0.5	-1.0 ± 0.6	-69 ± 2	-61 ± 2	-45 ± 3	-49 ± 2
NIMAC	-11.1 ± 0.4	-7.7 ± 0.8	-39 ± 1	-46 ± 1	-82 ± 2	-96 ± 4
NISUCA	-39 ± 1	-38 ± 1	-122 ± 6	-127 ± 9	-----	-299 ± 33

Values are expressed in min^{-1} x 10^4

Notably, early studies by Whitmore and Varghese (204,218) demonstrated by HPLC the existence of conjugates between GSH and reduced products of nitroimidazole derivatives both in vitro and in chinese hamster ovarian (CHO) cells. Furthermore, it had been shown that treatment with MISO

under hypoxia results in GSH depletion (31). The precise mechanism for the formation of the adducts has not yet been established, although covalent bonding of GSH to either C4, C5 and both C4 and C5 of the nitroimidazole ring have been detected both by MR and mass spectra (202). Studies concerning the metabolism of MIS0 by hypoxic rat livers showed that a MISO-glutathione conjugate was formed as a major metabolite, and that high doses of MIS0 result in depletion of hepatic glutathione (191,192). Furthermore, it was noted that formation of the MISO-GSH appears to correlate with the metabolic reduction of MIS0 (192).

A key issue to be solved to fully understand the activity of these markers is the nature of the complexes formed between reduced nitroimidazole derivatives and cellular components. Immunohistochemistry studies clearly detect the presence of macromolecular adducts, since the lower molecular weight adducts would have been washed away during histological processing. The situation may result more complex if nitroimidazole markers are investigated by non histochemical techniques. For example, in the case of MRS detection, narrow peaks would only become visible if the adduct can tumble sufficiently rapid in the MR timescale; otherwise, a significant T_2 reduction would lead to drastic resonance broadening, complicating the detection. Moreover, if the reduced drug reacts with immobilized macromolecules, it will become undetectable by MR after assuming the correlation time of the host macromolecule. In vivo ^{19}F MR studies have shown, however, the presence of narrow resonances. Ex vivo experiments carried out at high field revealed shorter T_2 values for the reduced bound compounds, and the signal detected at later time points was composed of several unresolved peaks (180). A possible explanation for these findings is that the MR-visible complexes are formed with small sulfhydryl-containing peptides, such as glutathione, rather than with large macromolecules. These adducts would then be small enough to tumble rapidly in the magnetic field, generating sufficiently narrow resonances detectable by in vivo and in vitro MR. The elimination rate of these small adducts may be relatively high, so that, 6 h after drug administration, no MR signals are detected anymore within the tissue. Such a rapid elimination would not be possible for adducts formed with larger macromolecules. In this context, Hoff et al. (82) found an inverse relationship between MRS and flow cytometry measurements of EF5 in prostate tumors. They explained this by suggesting that nitroimidazole binding to macromolecular and non-macromolecular cellular components is a competitive event between these two different binding sites. Summarizing, resonances observed by MRS shortly after drug administration are likely to be caused by nitroimidazole adducts with small molecules, such as reduced glutathione. The adducts observed immunohistochemically at later times may derive from coupling reactions with higher molecular weight cellular components, such as proteins or nucleic acids (174).

There are several possibilities for the formation of adducts between nitromidazole derivatives and GSH, as indicated in Figure 39. Unfortunately, these molecules are highly unstable and it has not

been possible to isolate and characterize them individually. However, our MR study provides some useful information. We focused in the imidazolyc protons in the region 6.8-7.7 ppm, since they are inherently very sensitive to any change in the redox state of the nitro group and/or any change in the imidazole ring. In addition, only the imidazole derivative and some NADPH's protons appear in this relatively uncrowded region of the spectra. Using this strategy, compounds I and II would appear as two doublets of the same intensity. Compounds III, IV, V and VI would appear as singlets. Compounds VII would give no signal in the aromatic region. Finally, compounds VIII would appear as several doublets (due to different conformational configuration possible). We detect indeed some these resonances (Figures 10, 12, 14, 16 & 19b) but at present we are not be able to assign them unambiguously. However, it is possible to propose a tentative assignment based in theoretical calculations, previous studies (36,203) and the kinetic time course (Table 13).

Considering this new information, it turns out that the previously presented scheme describing the biological reduction of nitroimidazole derivatives (Scheme 1) does not provide a completely correct interpretation of the reduction process. Our *in vitro* studies point towards a much more complex situation. Knox et al. (95) found 32 different reduction products of misonidazole by HPLC. In vivo, nitroimidazole based drugs eliminated by the renal pathway are basically excreted unchanged, with no metabolites detected by HPLC, either in urine or in plasma (1,2). Nevertheless, two steps have been proved to be certain, i) the formation of an anion radical at the beginning (137,213) and ii) that the reaction proceeds through hydoxilamine formation (44,95). Furthermore, some studies suggest that hidroxilamine is the terminal reactive species responsible for nitroimidazole in vivo activities (106,218) and a number of reaction mechanisms with cellular nucleophiles have been proposed (140). In this thesis we propose a new reduction mechanism that explains our present findings as well as those previously reported (Scheme 4).

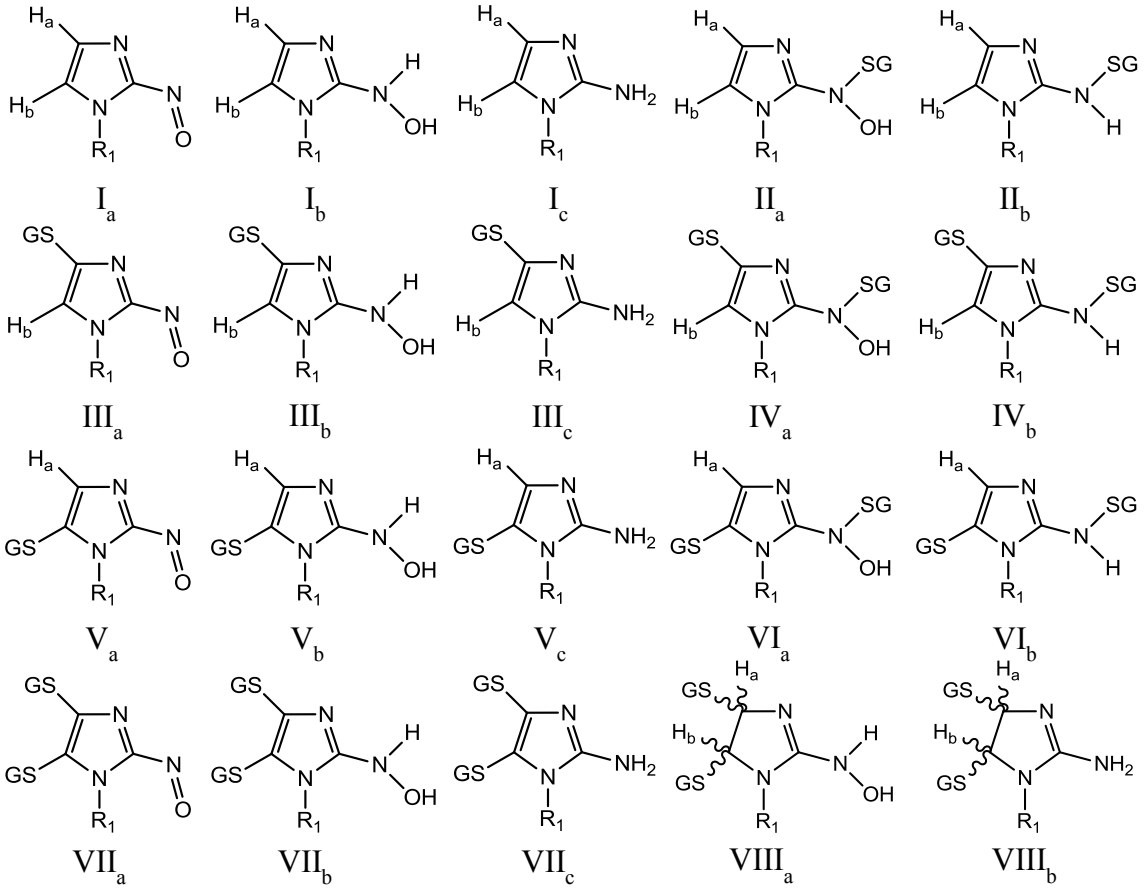

Figure 39. Chemical structure of the possible adducts formed between reduced nitroimidazolyl derivatives and reduced glutathione (GSH).
R_1 would be different for each hypoxia marker used (see Figure 7).

Table 13. Proposed assignment of the newly generated resonances of NISUCA conjugates originated during the bioreduction: theoretical and experimental chemical shift.

Compound[a]	Theoretical chemical shift (ppm)		Experimental chemical shift (ppm) [b]	
	H_a	H_b	H_a	H_b
I_a	**7.36 (d)**	**7.47 (d)**	7.24 (d)	7.55 (d) [N2]
I_b	**7.03 (d)**	**6.80 (d)**	6.98 (d)	6.897 (d) [N6]
II_a	7.08 (d)	7.11 (d)		
II_b	**7.04 (d)**	**6.84 (d)**		
I_c	**7.02 (d)**	**6.76 (d)**	6.92 (d)	6.85 (d) [N7]
III_c	-	**7.10 (s)**	7.06 (s) [N4]	
V_c	7.70 (s)	-		
III_b	-	6.78 (s)	7.095 (s) + 7.085 (s) [N3] 7.04 (s) [N5]	
IV_a	-	7.03 (s)		
IV_b	-	6.70 (s)		
V_b	7.28 (s)	-		
VI_a	7.64 (s)	-		
VI_b	7.09 (s)	-		
$VIII_a$	5.62 (d)	5.27 (d)	5.46 (d), 5.43 (d) [c] 5.37 (d)	
$VIII_b$	4.97 (d)	5.20 (d)		

[a] Roman numbers indicate the corresponding structure of Figure 39 to what these resonances were assigned.
[b] Square brackets indicate the molecular structure originating the newly generated resonances as indicated in Figure 16. [c] Newly generated signals depicted in figure 19b.

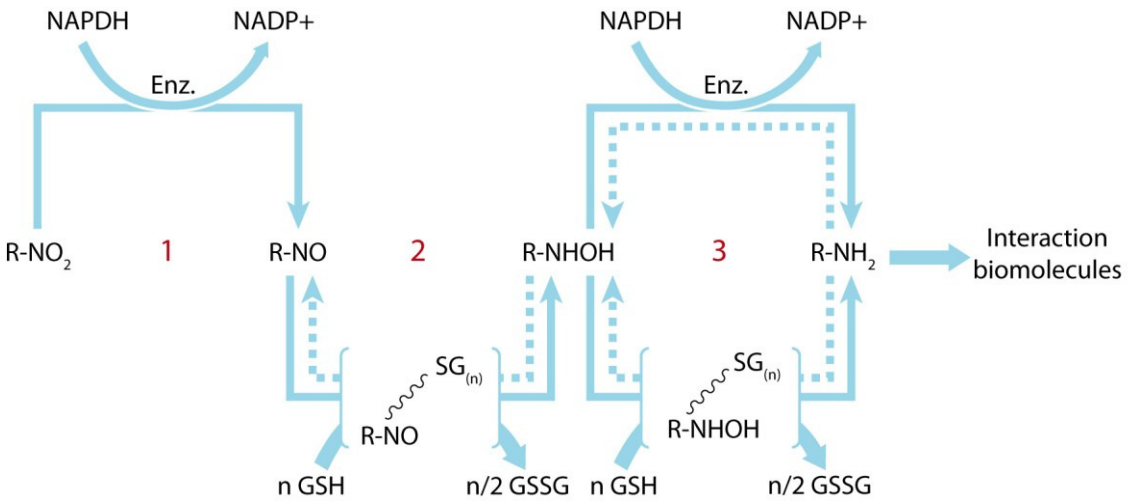

Scheme 4. Proposed mechanism for bioreduction of nitroimidazole derivatives with the concomitant participation of GSH and NADPH.

1. Enzymatic reduction of nitro to nitroso with NADPH consumption. 2 .Non enzymatic reduction of nitroso to hydroxylamine with the formation of a Nitroimidazole-GSH adduct. 3. Enzymatic (up) and non-enzymatic (bottom) reduction of hydroxylamine to amine derivative with NADPH consumption (up) and/or Nitromidazole-GS (bottom) adduct.

The first intermediate of the bioreduction process: a nitroso derivative (reaction 1, Scheme 4).

Metabolism of these compounds begins by the enzymatic reduction of the nitroimidazole derivative to the nitroso counterpart. This reaction is enzymatically catalyzed and proceeds with NADPH consumption. In fact, when no P450ase is present, the reaction does not progress. The disappearance of the probe occurs only when both P450ase and NADPH are present. GSH does not participate in this initial step since reduction proceed when GSH is not present and it is not able to reduce the hypoxic markers directly either alone or with P450ase, in the absence of NADPH (Table 7).

The second step: the hydroxylamine intermediate (reaction 2, Scheme 4)

The next step would be the non-enzymatic reduction of nitroso derivative to hydroxylamine with the concomitant oxidation of GSH to GSSG (reaction 2, Scheme 4). This reaction was proposed by Bump et al. (31) although it was not proved nor the exact mechanism elucidated. The reaction proceeds through the formation of an intermediate where GSH bonded covalently to the imidazole ring. We detected two new doublets closed to the original signals of NIMAC (NM2, Figure 14) and NISUCA (N2, Figure 16). We believe that these resonances belong to the nitroso derivatives, based on the theoretical chemical shift calculated for them by computational methods (Table 13). Indeed when GSH is not present, these resonances accumulate during the complete reaction time without any further transformation in both compounds. In contrast, when GSH is present, N2 reaches a plateau value early in the reduction process and, later, decreases slowly, indicating a net disappearance by transformation in a downstream intermediate. NM2 increases during the whole reaction. In both cases, the maximum concentration of N2 and NM2 is significantly smaller when GSH is present than

when it is not, suggesting that GSH favors the augmented disappearance of the nitroso intermediate. The nitroso derivatives cannot be further reduced in the absence of GSH, and can be considered as the final reduction products under these conditions. However, when GSH is present, the reduction can advance further and additional intermediates appear. The differences between NISUCA and NIMAC can be explained by the faster reduction rate of NISUCA, leading this compound to reach more rapidly a steady state of its reaction intermediates, whereas NIMAC is not able to reach this situation during the reaction time investigated. In both cases, the nitroso derivative generation was faster than its subsequent reactions, and a temporary accumulation can be detected. MISO and PIMO depicted a completely different situation. The fact that the nitroso derivative resonances from MISO and PIMO are not observed when GSH is not present is most probably due to a higher instability of their corresponding nitroso derivatives. When GSH is present, the generation of nitroso derivative is much slower than the posterior reactions of this reduced metabolite and thus no accumulation can be detected. This is in good agreement with the slower reduction constant found for MISO and PIMO under all tested conditions (Table 11).

When GSH and GR were present, GSH becomes not limiting (since it is continuously regenerated from GSSG) and signal N2 achieved a maximum value early in the reduction process and then began to decrease. These results indicate unambiguously that GSH is involved in later reduction steps (reaction 3, Scheme 4) whose velocity will be faster with high GSH availability. This explains why, in presence of GR, N2 reached a maximum faster in the reduction process (reaction 2 is GSH dependent) and afterwards, decreased more rapidly (reaction 3 is also GSH dependent). On the other hand, NM2 increases during the whole reaction time. It is explained because the reduction of NIMAC is slower in all tested conditions (Table 12) and even in the presence of GR, NIMAC was not fully consumed during the reaction time investigated. Interestingly, PIMO and MISO, those with low reduction constant, showed a small decrease in their reduction rates with GR (Table 12). This may be due to the fact that GR consumes also NADPH to reduce GSSG to GSH causing a decrease in NADPH availability for the initial reduction step (nitro to nitroso derivative), diminishing then competitively the rate of the overall process.

The third intermediate and final product: the amine derivative (reaction 3, Scheme 4)

Afterwards, hydroxylamine can be reduced to amine either by enzymatic (reaction 3 up, Scheme4) or non enzymatic (reaction 3 bottom, Scheme 3) pathways, with the concomitant oxidation of NADPH and GSH respectively. We found several newly generated signals when GSH is present in the medium that could be attributed to the different adducts depicted in Figure 39.

We propose that the reduction of the nitroso to hydroxilamine intermediates (reaction 2, Scheme 3) is the limiting step for the reduction of the nitroimidazole probes. The finding that the reaction is

inhibited at the nitroso derivative level in the absence of GSH and that the addition of GSH releases this inhibition and results in a high increase in the reduction rates under all the tested conditions provides a strong support to this concept. Furthermore, when GSH becomes not limiting (i.e., when GR is present), the reduction rate speeds up significantly with NIMAC and NISUCA. This is not the case with MISO and PIMO, due to the competition of GR and P450ase for NADPH in the in vitro situations tested. Several studies have reported the formation of conjugates between the chemically generated hydroxylamine derivatives and reduced glutathione, detected by ^{1}H MR (201,202,204). Nevertheless, to our knowledge, no previous studies have addressed the reduction and the chemistry of nitroso derivatives, most probably because the high instability of these compounds.

Previous studies proposed a mechanism for the addition of GSH to hydroxilamine (128,203). Based on these, the results presented above and the kinetics of formation of the different adducts, we propose the consensus reaction sequence depicted in Scheme 5. The previous proposals claimed that these types of reactions would occur in absence of P450ase and GSH, using hydroxyl anion (HO^-) as the nucleophile. This process could well be the origin of the resonances we detected with NISUCA in absence of GSH. Also, Varghese et al. (203) detected small group of resonances between 5.3 and 5.5 ppm, with the assigned to the different possible conformations of adduct VIII (Figure 39). We also detect such resonances in our spectra (Figure 19b) and our theoretical calculations predicted similar chemical shifts for these adducts (Table 13). The total reduction of nitroimidazole derivatives to their amine counterparts would require six electrons. However, our stoichiometry results reveal that 1.5 to 2 molecules of NADPH and 1 molecule of GSH were oxidized to $NADP^+$ and GSSG respectively, for every molecule of hypoxic marker consumed. This renders a 4 to 5 electron reduction under our conditions. These results are probably due to an incomplete reduction of the nitroimidazolyl derivatives. This interpretation is strongly supported by the fact that in all cases, at the end of the reaction, we still detect signals belonging to adducts between hypoxia marker and GSH.

The cell free results described above contribute valuable new information to the previously accepted relationship between the environmental oxygen tension and the reduction rate of 2-nitroimidazolyl derivatives, currently the basis for their use as hypoxia markers. Our results reveal that bioreduction of these probes cannot be explained only on the basis of decreased oxygen tension. Indeed, a reduced or absent oxygen tension alone has been shown to be unable to reduce the probes in cell free systems. Present results show that NADPH, GSH, P450ase and eventually GR play, in addition, determinant roles during the reduction processes of these probes. However, these are not independent events and in vivo, a reduced oxygen tension leads generally to a more reduced redox state and concomitant NADPH and GSH accumulation. Thus, the bioreduction of nitroimidazoles appears not to be directly related to a lower oxygen level, but rather to the increases in NADPH and GSH triggered by hypoxia.

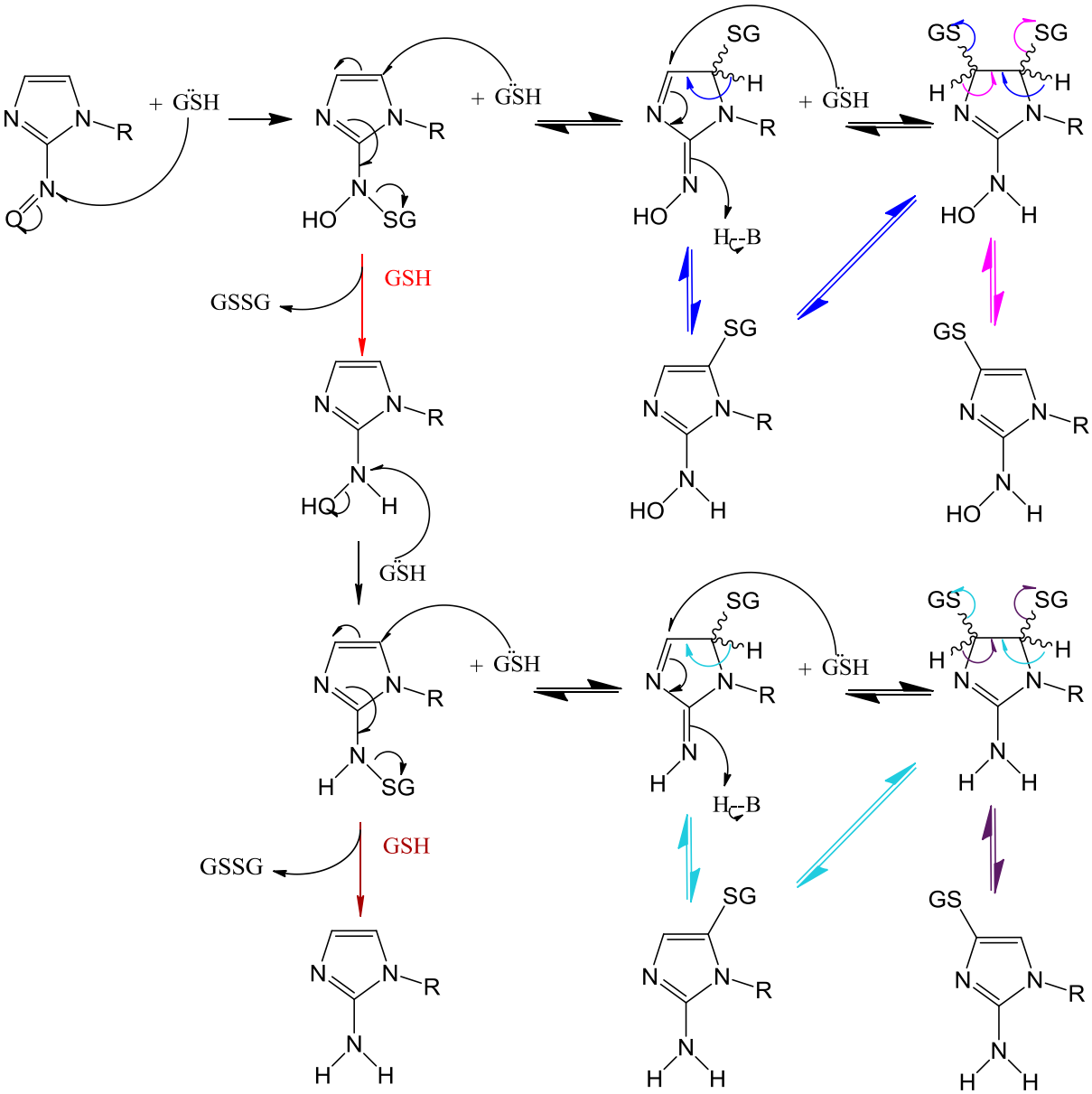

Scheme 5. Proposed reaction scheme for the formation of stable glutathione adducts of the nitroso derivatives of hypoxia probes.
B represents any base.

5.1.3. Reduction of hypoxic markers by C6 tumor cells

Tumor cells are frequently observed to exhibit elevated levels of GSH (20,32,39,49,53,81,162,219). Furthermore, several studies demonstrated that low oxygen levels increased GSH concentration both ex vivo, in normal (11,22) and in tumoral cells (11,149) and in vivo, as in the liver of healthy chicken (14) and in radiation induced tumors (RIF-1) grown in mice (105). Additionally, it has been shown that GSH concentration is proportional to environmental oxygen tension in normal cells while tumoral cells show greater GSH levels at low oxygen tensions than normal cells (11). Increases in GSH levels

promote an increase in the reductive capacity in the tumor, mimicking hypoxic situations (84). In general, a direct correlation between GSH levels and the reductive capacity of different tissues has been reported (84).

There is a variety of redox couples that work cooperatively in a cell to maintain the homeostasis of the redox environment including thioredoxins, NADPH, flavins, ascorbate, and others. However, the GSSG/GSH couple is the most abundant redox pair in cells and tissues (181). The intracellular concentration of GSH in eukaryotes is 1–10 mM while GSSG is maintained within 1/100–1/30 of the GSH levels (101). Nevertheless, high intertumor variability has been reported (68,73). Cysteine is another important thiol containing molecule that acts as redox buffer. Cysteine concentrations are typically much lower than GSH (1 to 10% of GSH) both in cell culture (214) and in normal tissues (96), but abnormally high levels have been found in vivo both in rodent tumors (96) and in human tumor biopsies (68).

We tested whether the oxygen tension had an impact in the ex vivo metabolism of nitroimidazolyl derivatives in cell cultures. Our results clearly showed that the remaining amount of initial hypoxia marker detectable after six hour of incubation decreased with oxygen availability, indicating increased reductive metabolism (Figure 22). Both hypoxic (1% O_2) and anoxic (0% O_2) conditions resulted in measurable decreases in the amounts of all nitroimidazolyl derivatives investigated. As expected, those probes with slow in vitro reduction rates, MISO and PIMO, were detected, at higher concentrations (8 to 18 % of total choline signal) compared with those that exhibited higher reduction constants, NIMAC and NISUCA (4 to 10 % of total choline signal) in all tested conditions.

We characterized the impact of the redox state in the normoxic metabolism of these compounds by changing the reductive capacity in the incubation medium. For that purpose, we added GSH to incubation medium. However, GSH is taken only in small amounts by cells (109) and no appreciable changes were detected. Then, MISO was incubated in C6 cells in normoxia within oxidative conditions (glucose, glucose + lactate) and reductive conditions (glucose + pyruvate, glucose + cysteine). It should be noted that pyruvate is a precursor for the biosynthesis of glutathione through oxidative metabolism in HepG2 cells under normoxic conditions (178), preventing the loss of GSH and the reduction in the GSH:GSSG ratio of swine liver after hemorrhagic shock (135). Increased cysteine uptake and GSH synthesis under hypoxia in glioma cells have been reported (149). Total glutathione levels were measured as an indicator of the redox state of the cell. Glucose alone and in combination with lactate resulted in low levels of GSH and a decrease in the reduction of the hypoxic marker (Figure 23). On the other hand, pyruvate and cysteine had the opposite effect, increasing both total GSH and the reduction of nitroimidazolyl derivatives. Nitroimidazolyl derivatives under oxidative conditions behaved as in normoxia whereas reductive conditions mimicked hypoxic situation. The effect of the redox state in the amount of detectable hypoxia marker 6 h after incubation is, thus,

much higher than the effect of oxygen availability. The remaining MISO was detected at much higher concentration (33% of the TCho) for oxidative than reductive conditions (3% of the TCho) under normoxia (Figure 23b). Reducing oxygen availability induced a decrease from 15% in normoxia to 12% and 11% in hypoxia and anoxia respectively (Figure 22b). Taken together, these results highlight the importance of the redox state in the reduction rate of nitroimidazolyl derivatives.

Using EPR and EPRI, Kuppusamy *et al* (105) showed a preferential reduction of nitroxides in RIF-1 tumors compared to normal tissue in mice. Furthermore, these authors showed that this increase was directly related to higher GSH concentration in tumor than in muscle. Using the GSH depletion agent BSO they demonstrated that the reduction rate of nitroxides is tightly coupled to reduced glutathione content in tumors. Previously, they demonstrated that these tumors present lower pO_2 (10 ± 2 mm Hg) than muscle (40 ± 2 mm Hg) and higher reducing capacity (104). Similar results were found by Yamada et al. (223). Depletion of GSH using diethylmaleate (DEM) decreased the reduction rate of nitroxides by 24% and 36% in normal and tumor (RIF-1) tissues respectively. This was linked to a reduction in GSH levels of 55% and 60% in tumor and muscle tissue respectively. On these grounds, the reason for the higher impact in tumor compared to normal tissue may be reflect the higher basal GSH levels in tumors.

Several studies reported a relationship between nitroimidazolyl reduction and high levels of Non Protein Sulfhydryl groups (NPSH). Moreno-Merlo et al. (136) used cervical cancer xenografts (ME180 and SiHa) grown in mice. They showed that areas with positive EF5 staining presented significantly higher levels of NPSH that those without EF5. Vukovic et al. (215) found differential expression of NPSH levels in regions of hypoxia, measured by EF5 staining, that are proximal or distal to blood vessels in cervical carcinoma xenografts tumors (SiHa cell line). Regions positively stained for EF5 were classified by distance to the nearest visible blood vessel. Significantly higher NPSH levels were found in EF5 positive regions close to blood vessels than in regions at a higher distance from them. These results were explained through the assumption that regions distal from blood vessels presented impaired cellular metabolic status. Thus, increase in GSH consumption cannot be counterbalanced by the regeneration mechanism of GSH, resulting in a net loss. On the other hand, EF5 positive regions close to blood vessel are indeed intermittently perfused, and thus NPSH levels could be regenerated after transient hypoxia and the concomitant increase in GSH consumption.

On these grounds, we proposed that the nitroimidazole reduction rate and subsequent binding to cellular components is controlled not only by pO_2, but more importantly by the redox state. The relative contribution of each one of these parameters must be evaluated for each hypoxia marker individually. Nevertheless, both factors appear to be closely related in vivo. Furthermore, there is increasing evidence for crosstalk between hypoxia sensitivity and redox response pathways, mainly through the transcription factors HIF-1α and NF-κB (69). It is widely accepted that hypoxia increase

the production of reactive oxygen species (ROS) (37,38,45,46,118), while ROS promote the stabilization and activity of HIF-1α (7,8,38,118,182).

Taken together, all these evidences suggest that oxygenation controls the reduction rate of nitroimidazolyl probes through the modulation of the redox state of the cell rather than through a direct effect on the reduction rate of these compounds.

5.1.4. Maps of in vivo bioreduction of 2-nitroimidazole derivatives

Finally, we aimed to investigate whether nitroimidazolyl derivatives can be used as hypoxia marker in vivo in combination with ^{1}H MRS detection. Previously, fluorinated nitroimidazole has been used for this purpose (157). This approach generates excellent signal to noise spectra due to absence of natural abundance fluorine signal. By using ^{1}H MRS, metabolic information could be obtained at the same time, but the large amount of background resonances could difficult the detection. However, heterocyclic protons of nitroimidazole derivatives appear between 7.2 and 7.7 ppm, a spectral region where no resonances from other metabolites are usually detected, therefore overcoming this limitation.

We used a similar approach to that described previously for fluorinated nitroimidazoles. We measured the MISO and TSP signal immediately after intratumoral injection and 60 min post injection, and their ratio was calculated. Due to the direct intratumoral injection of the probes, these were rapidly distributed within the tumor. The first measurement was considered as reflecting the total parental compound injected. The TSP decrease would provide a measurement of the natural clearance. We detected a tendency towards faster TSP clearance with decreasing oxygen availability (Table 8), although it did not reach statistical significance. Notably, MISO depicted a much larger decrease when diminishing the percentage of oxygen breathed. There was an increasing difference between the amount of remaining compound 1 h after injection between MISO and TSP with increasing hypoxia (Table 8). Both percentages were very similar in hyperoxia ([TSP]-[MISO]=6%), but this difference increased significantly in normoxia (15%). Moreover, during hypoxia, the difference between the remaining TSP and MISO reached his maximum value (24%). These results suggest that the main source of compound disappearance under hyperoxia is the physiological clearance, but under hypoxia, the biomarker reduction plays a dominant role in signal decrease. These results demonstrate that the new methodology is sensitive enough to detect changes in tumor oxygenation in vivo.

We also show that real time imaging of the distribution of MISO and TSP is possible using multivoxel spectroscopy. Spectroscopic maps of the percentage of remaining MISO and TSP showed high intratumoral variability both for MISO and TSP in all animals investigated (Figures 27 and 28).

However, hyperoxygenated animals showed significantly higher percentage of remaining MISO (77 ± 1 %) than normoxic animals (58 ± 1%). It should be noted that, there is not such difference for remaining TSP, which showed 72 ± 2 and 72 ± 1 % for hyperoxic and normoxic tumors, respectively.

The approach proposed here presents several advantages over the previous studies. The use of ^{1}H MRSI would allow obtaining metabolic and/or pH maps the region of interest. It presents, however, several drawbacks, as the high background signal from natural components of the imaged tissue. This prompted us to use larger doses (300 mg/kg) that previously described for ^{19}F nitroimidazole (200 mg/kg) (169), which afforded us also improved spatial (4 μl^3) and temporal (12 min) resolution. Even with this higher dose, animals did not show any visible symptoms of toxicity. One of the main advantages of this approach relays in its direct and convenient translation to clinic, especially for tumors located superficially, as lymph nodes from head and neck tumors, where hypoxia has been demonstrated to become particularly relevant (6,29,86). Taken together, these results support the use of nitroimidazolyl derivatives as ^{1}H MRS hypoxia sensitive probes.

5.2 DOCENT (Dynamic Oxygen Challenge Evaluated by NMR T_1 and T_2*)

In many cases, the selection of patients responding positively to hypoxia-directed treatments would not necessarily require a quantitative measurement of the oxygen tension but rather to monitor the response of tumors to a specific pO_2 modulation. To this end, we implemented a novel imaging approach with high temporal and spatial resolution and using endogenous sources of contrast. This method is based on the paramagnetic properties of molecular oxygen (TOLD) and deoxyhemoglobin (BOLD) as surrogate markers of pO_2.

5.2.1. Predictive value of BOLD and TOLD to identify tumors responsive to pO_2 modulation

As expected, BOLD and TOLD contrast responses to breathing hyperoxic gas were quite different for the diverse tumor sublines and sizes employed. Smaller HI tumors, reported to be well oxygenated and highly responsive to hyperoxic gas challenge (226), showed the largest signal changes, whereas larger AT1 tumors, reported to be hypoxic and unresponsive (25), showed the smallest responses. Each tumor showed considerable heterogeneity within an image slice, but quite similar response between slices and overall consistency between multiple tumors of a given group.

BOLD signal responses were larger than TOLD using the current acquisition parameters (Figure 34), but there was a strong correlation between the magnitudes of both (Figure 35a). There was generally an inverse relationship between the magnitude of BOLD signal response and change in R_2*, but direct correlation was weak (R^2 = 0.6). This finding suggests additional effects beyond deoxyhemoglobin concentration influencing the SI (83). Indeed, carbogen breathing has been reported to increase both

oxyhemoglobin and total hemoglobin, as observed using near infrared spectroscopy of small HI tumors (113).

The fact that the BOLD response is generally greater than the TOLD response prompts the question as to the advantage of measuring both parameters. A particular concern with BOLD alone is that it is subject to additional influences such as flow (83) and has been shown to exhibit contradictory behavior with respect to tumor oxygenation in some cases (83,89). Noting that BOLD responses preceded TOLD (Figures 29-32 & 34) adds confidence to the oxygen dependence, since enhanced oxygen delivery generates elevated pO_2. Moreover, in HI tumors a strong correlation was found between ΔR_1 and ΔR_2* consistent with change in vascular oxygenation underlying the change in tumor pO_2, although this was not observed in the AT1 tumors (Figure 34b). BOLD alone showed significant differences between smaller HI tumors and smaller or larger AT1 tumors (Table 8). TOLD additionally showed a significant difference between the responses of larger HI and AT1 tumors. As a potential predictive biomarker, BOLD alone correctly characterized all the larger AT1 tumors as likely to be hypoxic (Table 10). However, BOLD misclassified 8 of 22 tumors expected to be oxic as hypoxic. TOLD alone misclassified only three of these tumors, suggesting that combined BOLD and TOLD stratification may be more robust. The large BOLD and TOLD responses in the HI tumors as compared with AT1 tumors were expected, since the HI tumors are reported to be much better vascularized and grow more slowly (227,228).

5.2.2. Origin of BOLD and TOLD signals

The T_2*W signal response was very similar to that reported previously for AT1 tumors (87) and baseline R_2* values fell within the range reported for diverse tumors types at 4.7 T (10,130,175,176). Human prostate tumors in patients and DU145 and PC3 tumor xenografts in mice were reported to have R_2* values and signal responses similar to the R3327-AT1 and HI tumors found here (10). A return to baseline R_2* before return to air breathing was reported in PC3 tumors, as seen for the larger AT1 tumors here (Figure 32c).

Rodrigues *et al.* (176) previously reported that ΔR_2* in response to breathing carbogen was indicative of tumor growth delay in response to radiotherapy, in highly vascularized GH3 prolactinomas, but not in RIF-1 tumors. RIF-1 showed particularly low baseline R_2* and little response to carbogen, consistent with small vascular fraction. Likewise, larger AT1 tumors, which are reported to exhibit large hypoxic fraction, which does not respond to hyperoxic gas breathing, showed the smallest BOLD signal response (Table 8). The larger AT1 tumors showed a tendency for increases in R_2* with CB, as opposed to the other groups of tumors, which showed decreased values (Table 9). R_1 values were in the range reported for many other tumor types at 4.7 T (131), though much lower than those reported for SCC tumors in a study of hyperoxic and hyperbaric gas intervention (125).

The T_2*W measurements agree with independent reported oximetry both for HI and AT1 tumors, and hence, may become useful as non-invasive prognostic biomarkers to assess hypoxia, and predict response to hyperoxic gas breathing interventions. Indeed, in a previous study in rat breast tumors, it was shown that a BOLD signal response exceeding 3% coincided with elimination of hypoxic fraction (HF_{10}< 5%) (230). A recent study by Arias-Ramos et al. (12) showed the predictive value of this technique. They used a C6 glioblastoma model implanted in rat brain and treated with radiotherapy in combination with hyperoxic gas breathing. The authors showed that tumors depicting diferences in TOLD response between tumoral and normal tissue bigger than 40% respond well to treatment combination whereas those with smaller changes showed no additional benefit to the animals treated in normoxic conditions. T_2*W measurements alone are subjected to additional influences as blow flow, hemoglobin content… Thus adding T_1W imaging protocols appears valuable.

In summary, this new methodology is non-invasive, simple to implement, highly reproducible and reveals spatial and temporal heterogeneity of oxygen dynamics. Change in SI alone appears useful in itself, but we recognize its absolute magnitude depends on R_1 and R_2*, and the TE and TR times. Our results showed similar tumor stratification to that reported using quantitative ^{19}F oximetry. Tumor stratification (oxic- responsive to oxygen breathing vs. hypoxic) may allow therapy to be tailored to the individual characteristics of the tumor.

6. CONCLUSIONS

1. We investigated the synthesis and the redox properties of a new series of nitroimidazole succinic esters, potentially useful as hypoxia probes. Dimethyl 2-nitroimidazol-1-ylsuccinate (NISUCA) depicted suitable properties, prompting their use as a novel ^{1}H-MR hypoxia markers.
2. The role of oxygen and GSH availability in the reduction of four nitroimidazole derivatives was tested. GSH showed to have a much greater impact than molecular oxygen in the reduction rate, increasing it either in anoxic and normoxic conditions. The influence of oxygen deprivation in the in vitro reduction of these compounds was negligible.
3. We propose a new mechanism for the reduction of nitroimidazolyl derivatives. Within this new scheme, the control point in the reduction rate would be the covalent binding of the nitroso derivative, enzymatically generated, to GSH. This process would continue through the non enzymatic reduction of nitroso to hydroxylamine with concomitant oxidation of GSH to GSSG. Further reduction steps could occur either enzymatically of through the formation of new nitroimidazole-GSH adducts. The possible structures of these adducts are proposed.
4. The potential use of nitroimidazole derivatives as hypoxia marker by ^{1}H-MRS was investigated. All the compounds showed a greater decrease in the signal of initial concentration when incubated under hypoxic conditions than in normoxia, suggesting increased metabolism under hypoxic conditions. Nitroimidazolyl derivatives with higher in vitro reduction rate constants were more rapidly reduced ex vivo by C6 cells than those with slower in vitro reduction rate constants.
5. Ex vivo studies showed that the redox state of the cell depicted a larger impact than the oxygen tension in the reduction of nitroimidazole derivative. Highly reductive environment (high GSH concentrations) resulted in faster consumption of the hypoxia probe than hypoxic environment, whereas highly oxidative environment (low GSH concentration) resulted in slower depletion of the hypoxia probe than normoxic conditions.
6. We propose that the reduction of nitroimidazole derivative is not a direct measurement of pO_2 but of the associated changes in the redox state. Thus the in vivo selective reduction and retention of nitroimidazolyl derivatives is not a direct consequence of hypoxia but of the shift of the redox state towards a more reduced environment, resulting in faster reduction rates and increased retention of the biomarkers. Any other alteration of the redox environment not related to oxygen availability would eventually cause changes in the metabolism of 2-nitroimidazolyl derivatives.
7. A new methodology for the use of 2-nitroimidazole derivatives as in vivo ^{1}H-MRS hypoxia marker was described. It was based on the ratio of the hypoxia marker signal immediately after and 1 h after compound administration. This ratio was related to the percentage of oxygen in the inspired gas and these differences came from in vivo reduction of the hypoxia probe.

8. Dynamic Oxygen Challenge Evaluated by MR T_1 and T_2* (DOCENT) provided a non-invasive method to distinguish between responsive and non responsive tumors to hyperoxic gas challenge, potentially allowing hypoxic tumor identification and tailor therapy to these characteristics.
9. DOCENT methodology is non-invasive, simple to implement, highly reproducible and reveals spatial and temporal heterogeneity of oxygen dynamics. It does not quantify pO_2 or hypoxic fraction (potential advantages of ^{19}F oximetry, ESR, or electrodes) but requires no exogenous reporter molecule and it is directly and easily translatable to the clinic.

7. BIBLIOGRAPHY

1. Aboagye E. O., et al. (1995), 'Development and validation of a solid-phase extraction and high-performance liquid chromatographic assay for a novel fluorinated 2-nitroimidazole hypoxia probe (SR-4554) in Balb/c mouse plasma', *J Chromatogr B Biomed Appl,* 672 (1), 125-32.
2. Aboagye E. O., et al. (1996), 'The pharmacokinetics, bioavailability and biodistribution in mice of a rationally designed 2-nitroimidazole hypoxia probe SR-4554', *Anticancer Drug Des,* 11 (3), 231-42.
3. Aboagye E. O., et al. (1997), 'Bioreductive metabolism of the novel fluorinated 2-nitroimidazole hypoxia probe N-(2-hydroxy-3,3,3-trifluoropropyl)-2-(2-nitroimidazolyl) acetamide (SR-4554)', *Biochem Pharmacol,* 54 (11), 1217-24.
4. Aboagye E. O., et al. (1997), 'Preclinical evaluation of the fluorinated 2-nitroimidazole N-(2-hydroxy-3,3,3-trifluoropropyl)-2-(2-nitro-1-imidazolyl) acetamide (SR-4554) as a probe for the measurement of tumor hypoxia', *Cancer Res,* 57 (15), 3314-18.
5. Aboagye E. O., et al. (1998), 'The relationship between tumour oxygenation determined by oxygen electrode measurements and magnetic resonance spectroscopy of the fluorinated 2-nitroimidazole SR-4554', *Br J Cancer,* 77 (1), 65-70.
6. Adam M. F., et al. (1999), 'Tissue oxygen distribution in head and neck cancer patients', *Head Neck,* 21 (2), 146-53.
7. Agani F. H., et al. (2000), 'The role of mitochondria in the regulation of hypoxia-inducible factor 1 expression during hypoxia', *J Biol Chem,* 275 (46), 35863-7.
8. Agani F. H., et al. (2002), 'Inhibitors of mitochondrial complex I attenuate the accumulation of hypoxia-inducible factor-1 during hypoxia in Hep3B cells', *Comp Biochem Physiol A Mol Integr Physiol,* 132 (1), 107-9.
9. Akerboom T. P. and Sies, H. (1981), 'Assay of glutathione, glutathione disulfide, and glutathione mixed disulfides in biological samples', *Methods Enzymol,* 77, 373-82.
10. Alonzi R., et al. (2009), 'Carbogen breathing increases prostate cancer oxygenation: a translational MRI study in murine xenografts and humans', *Br J Cancer,* 100 (4), 644-48.
11. Allen R. G. and Balin, A. K. (2003), 'Effects of oxygen on the antioxidant responses of normal and transformed cells', *Exp Cell Res,* 289 (2), 307-16.
12. Arias-Ramos N., Pacheco-Torres, J., and López-Larrubia, P. Magnetic Resonance Imaging in a rat high-grade glioma model to predict the improvement in radiotherapy response by hyperoxic conditions. Proceedings of Annual Scientific Meeting of the European Society for Magnetic Resonance in Medicine and Biology; 2012; Lisbon, Portugal. p 311.
13. Avril N. E. and Weber, W. A. (2005), 'Monitoring response to treatment in patients utilizing PET', *Radiol Clin North Am,* 43 (1), 189-204.
14. Bao H. G., et al. (2011), 'Comparison of effects of hypoxia on glutathione and activities of related enzymes in livers of Tibet chicken and Silky chicken', *Poult Sci,* 90 (3), 648-52.
15. Baudelet C. and Gallez, B. (2002), 'How does blood oxygen level-dependent (BOLD) contrast correlate with oxygen partial pressure (pO2) inside tumors?', *Magn ResonMed,* 48 (6), 980-86.
16. Bauerle T., Komljenovic, D., and Semmler, W. (2012), 'Monitoring molecular, functional and morphologic aspects of bone metastases using non-invasive imaging', *Curr Pharm Biotechnol,* 13 (4), 584-94.
17. Berg J. M., Tymoczko, J.L., and Stryer, L. (2001), *Biochemistry* (5 edn.).
18. Bergemeyer H.U. (1983), *Methods of enzymatic analysis.* (Weinheim: Verlag Chemie).
19. Bhujwalla Z. M., et al. (2002), 'Combined vascular and extracellular pH imaging of solid tumors', *NMR Biomed,* 15 (2), 114-9.
20. Blair S. L., et al. (1997), 'Glutathione metabolism in patients with non-small cell lung cancers', *Cancer Res,* 57 (1), 152-5.
21. Blouw B., et al. (2003), 'The hypoxic response of tumors is dependent on their microenvironment', *Cancer Cell,* 4 (2), 133-46.

22. Bogdanova A. Y., et al. (2003), 'Pivotal role of reduced glutathione in oxygen-induced regulation of the Na(+)/K(+) pump in mouse erythrocyte membranes', *J Membr Biol,* 195 (1), 33-42.
23. Bolton J. L. and McClelland, R. A. (1989), 'Kinetics and mechanism of the decomposition in aqueous-solutions of 2-(hydroxyamino)imidazoles.', *Journal of the American Chemical Society,* 111 (21), 8172-81.
24. Bollo S., et al. (2001), 'Cyclic voltammetric studies on nitro radical anion formation from megazol and some related nitroimidazole derivatives', *J Electroanal Chem,* 511 (1-2), 46-54.
25. Bourke V. A., et al. (2007), 'Correlation of Radiation Response with Tumor Oxygenation in the Dunning Prostate R3327-AT1 Tumor', *Int J Radiat Oncol Biol Phys,* 67 (4), 1179-86.
26. Brezden C. B., et al. (1998), 'Oxidative stress and 1-methyl-2-nitroimidazole cytotoxicity', *Biochem Pharmacol,* 56 (3), 335-44.
27. Brizel D. M., et al. (1995), 'Patterns and variability of tumor oxygenation in human soft tissue sarcomas, cervical carcinomas, and lymph node metastases', *Int J Radiat Oncol Biol Phys,* 32 (4), 1121-25.
28. Brizel D. M., et al. (1996), 'Tumor oxygenation predicts for the likelihood of distant metastases in human soft tissue sarcoma', *Cancer Res,* 56 (5), 941-43.
29. Brizel D. M., et al. (1999), 'Oxygenation of head and neck cancer: changes during radiotherapy and impact on treatment outcome', *Radiother Oncol,* 53 (2), 113-17.
30. Bubnovskaya L., et al. (2007), 'Bioenergetic status and hypoxia in Lewis lung carcinoma assessed by 31P NMR spectroscopy: correlation with tumor progression', *Exp Oncol,* 29 (3), 207-11.
31. Bump E. A., Taylor, Y. C., and Brown, J. M. (1983), 'Role of glutathione in the hypoxic cell cytotoxicity of misonidazole', *Cancer Res,* 43 (3), 997-1002.
32. Butler R. N., et al. (1994), 'Glutathione concentrations and glutathione S-transferase activity in human colonic neoplasms', *J Gastroenterol Hepatol,* 9 (1), 60-3.
33. Cairns R. A., Khokha, R., and Hill, R. P. (2003), 'Molecular mechanisms of tumor invasion and metastasis: an integrated view', *Curr Mol Med,* 3 (7), 659-71.
34. Cerdan S., Kunnecke, B., and Seelig, J. (1990), 'Cerebral metabolism of [1,2-13C2]acetate as detected by in vivo and in vitro 13C NMR', *J Biol Chem,* 265 (22), 12916-26.
35. Clottes E. (2005), 'Hypoxia-inducible factor 1: regulation, involvement in carcinogenesis and target for anticancer therapy', *Bull Cancer,* 92 (2), 119-27.
36. Chacon E., et al. (1988), 'Regioselective formation of a misonidazole-glutathione conjugate as a function of pH during chemical reduction', *Biochem Pharmacol,* 37 (2), 361-3.
37. Chandel N. S., et al. (1998), 'Mitochondrial reactive oxygen species trigger hypoxia-induced transcription', *Proc Natl Acad Sci U S A,* 95 (20), 11715-20.
38. Chandel N. S., et al. (2000), 'Reactive oxygen species generated at mitochondrial complex III stabilize hypoxia-inducible factor-1alpha during hypoxia: a mechanism of O2 sensing', *J Biol Chem,* 275 (33), 25130-8.
39. Chang T. C., Chang, M. J., and Hsueh, S. (1993), 'Glutathione concentration and distribution in cervical cancers and adjacent normal tissues', *Gynecol Obstet Invest,* 36 (1), 52-5.
40. Chapa F., et al. (2000), 'Metabolism of (1-(13)C) glucose and (2-(13)C, 2-(2)H(3)) acetate in the neuronal and glial compartments of the adult rat brain as detected by [(13)C, (2)H] NMR spectroscopy', *Neurochem Int,* 37 (2-3), 217-28.
41. Chapman J. D., et al. (1998), 'Measuring hypoxia and predicting tumor radioresistance with nuclear medicine assays', *Radiother Oncol,* 46 (3), 229-37.
42. Dang C. V. and Semenza, G. L. (1999), 'Oncogenic alterations of metabolism', *Trends Biochem Sci,* 24 (2), 68-72.
43. de Graaf R. A. (2007), *In Vivo NMR Spectroscopy: Principles and Techniques, 2nd ed.* (Chichester, UK: Wiley) 592.
44. Declerck P. J. and Deranter, C. J. (1987), 'Electron requirements in nitroimidazole reduction', *Analusis,* 15 (3), 148-50.
45. Dirmeier R., et al. (2002), 'Exposure of yeast cells to anoxia induces transient oxidative stress. Implications for the induction of hypoxic genes', *J Biol Chem,* 277 (38), 34773-84.

46. Duranteau J., et al. (1998), 'Intracellular signaling by reactive oxygen species during hypoxia in cardiomyocytes', *J Biol Chem,* 273 (19), 11619-24.
47. Elaut G., et al. (2006), 'Molecular mechanisms underlying the dedifferentiation process of isolated hepatocytes and their cultures', *Curr Drug Metab,* 7 (6), 629-60.
48. Emsley John (2001), 'Oxygen', *Nature's building blocks: an A-Z guide to the elements* (Oxford: Oxford University Press), 297-304.
49. Engin A. (1976), 'Glutathione content of human skin carcinomas', *Arch Dermatol Res,* 257 (1), 53-5.
50. Evans S. M. and Koch, C. J. (2003), 'Prognostic significance of tumor oxygenation in humans', *Cancer Lett,* 195 (1), 1-16.
51. Evans S. M., et al. (2004), 'Comparative measurements of hypoxia in human brain tumors using needle electrodes and EF5 binding', *Cancer Res,* 64 (5), 1886-92.
52. Fels D. R. and Koumenis, C. (2006), 'The PERK/eIF2alpha/ATF4 module of the UPR in hypoxia resistance and tumor growth', *Cancer Biol Ther,* 5 (7), 723-28.
53. Ferraris A. M., et al. (1994), 'Increased glutathione in chronic lymphocytic leukemia lymphocytes', *Am J Hematol,* 47 (3), 237-8.
54. Fitzsimmons S. A., et al. (1996), 'Reductase enzyme expression across the National Cancer Institute Tumor cell line panel: correlation with sensitivity to mitomycin C and EO9', *J Natl Cancer Inst,* 88 (5), 259-69.
55. Flynn R. T., et al. (2008), 'Intensity-modulated x-ray (IMXT) versus proton (IMPT) therapy for theragnostic hypoxia-based dose painting', *Phys Med Biol,* 53 (15), 4153-67.
56. Foo S. S., et al. (2004), 'Functional imaging of intratumoral hypoxia', *Mol Imaging Biol,* 6 (5), 291-305.
57. Gallez B., Baudelet, C., and Jordan, B. F. (2004), 'Assessment of tumor oxygenation by electron paramagnetic resonance: principles and applications', *NMR Biomed,* 17 (5), 240-62.
58. Garcia-Martin M. L., et al. (2001), 'Mapping extracellular pH in rat brain gliomas in vivo by 1H magnetic resonance spectroscopic imaging: comparison with maps of metabolites', *Cancer Res,* 61 (17), 6524-31.
59. Gatenby R. A., et al. (1988), 'Oxygen distribution in squamous cell carcinoma metastases and its relationship to outcome of radiation therapy', *Int J Radiat Oncol Biol Phys,* 14 (5), 831-38.
60. Gatenby R. A. and Gillies, R. J. (2004), 'Why do cancers have high aerobic glycolysis?', *Nat Rev Cancer,* 4 (11), 891-9.
61. Gatenby R. A. and Gillies, R. J. (2008), 'A microenvironmental model of carcinogenesis', *Nat Rev Cancer,* 8 (1), 56-61.
62. Gil S., et al. (1994), 'Imidazol-1-ylalkanoic acids as extrinsic 1H NMR probes for the determination of intracellular pH, extracellular pH and cell volume', *Bioorg Med Chem,* 2 (5), 305-14.
63. Gillies R. J., et al. (2002), 'MRI of the tumor microenvironment', *J Magn Reson Imaging,* 16 (4), 430-50.
64. Graeber T. G., et al. (1996), 'Hypoxia-mediated selection of cells with diminished apoptotic potential in solid tumours', *Nature,* 379 (6560), 88-91.
65. Gray L. H., et al. (1953), 'The concentration of oxygen dissolved in tissues at the time of irradiation as a factor in radiotherapy', *Br J Radiol,* 26 (312), 638-48.
66. Greco O. and Scott, S. (2007), 'Tumor hypoxia and targeted gene therapy', *Int Rev Cytol,* 257, 181-212.
67. Griffiths J. R. and Robinson, S. P. (1999), 'The OxyLite: a fibre-optic oxygen sensor', *Br J Radiol,* 72 (859), 627-30.
68. Guichard M., et al. (1990), 'Glutathione and cysteine levels in human tumour biopsies', *Br J Radiol,* 63 (751), 557-61.
69. Haddad J. J. (2002), 'Oxygen-sensing mechanisms and the regulation of redox-responsive transcription factors in development and pathophysiology', *Respir Res,* 3, 26.
70. Hahn E. W., et al. (1993), 'Isolated tumor growth in a surgically formed skin pedicle in the rat: a new tumor model for NMR studies', *Magn Reson Imaging,* 11 (7), 1007-17.

71. Harris A. L. (2002), 'Hypoxia--a key regulatory factor in tumour growth', *Nat Rev Cancer,* 2 (1), 38-47.
72. Harrison L. and Blackwell, K. (2004), 'Hypoxia and anemia: factors in decreased sensitivity to radiation therapy and chemotherapy?', *Oncologist,* 9 Suppl 5, 31-40.
73. Hedley D. W., et al. (2005), 'Relations between non-protein sulfydryl levels in the nucleus and cytoplasm, tumor oxygenation, and clinical outcome of patients with uterine cervical carcinoma', *Int J Radiat Oncol Biol Phys,* 61 (1), 137-44.
74. Helczynska K., et al. (2003), 'Hypoxia promotes a dedifferentiated phenotype in ductal breast carcinoma in situ', *Cancer Res,* 63 (7), 1441-44.
75. Hennig J., Nauerth, A., and Friedburg, H. (1986), 'RARE imaging: a fast imaging method for clinical MR', *Magn Reson Med,* 3 (6), 823-33.
76. Hennig J. and Friedburg, H. (1988), 'Clinical applications and methodological developments of the RARE technique', *Magn Reson Imaging,* 6 (4), 391-5.
77. Hickey M. M. and Simon, M. C. (2006), 'Regulation of angiogenesis by hypoxia and hypoxia-inducible factors', *Curr Top Dev Biol,* 76, 217-57.
78. Hockel M., et al. (1996), 'Association between tumor hypoxia and malignant progression in advanced cancer of the uterine cervix', *Cancer Res,* 56 (19), 4509-15.
79. Hockel M., et al. (1999), 'Hypoxic cervical cancers with low apoptotic index are highly aggressive', *Cancer Res,* 59 (18), 4525-28.
80. Hockel M. and Vaupel, P. (2001), 'Tumor hypoxia: definitions and current clinical, biologic, and molecular aspects', *J Natl Cancer Inst,* 93 (4), 266-76.
81. Hochwald S. N., et al. (1997), 'Elevation of glutathione and related enzyme activities in high-grade and metastatic extremity soft tissue sarcoma', *Ann Surg Oncol,* 4 (4), 303-9.
82. Hoff M. N., et al. (2008), 'In vivo measurement of the hypoxia marker EF5 in Shionogi tumours using (19)F magnetic resonance spectroscopy', *Int J Radiat Biol,* 84 (3), 237-42.
83. Howe F. A., et al. (2001), 'Issues in flow and oxygenation dependent contrast (FLOOD) imaging of tumours', *NMR Biomed,* 14 (7-8), 497-506.
84. Ilangovan G., et al. (2002), 'In vivo measurement of tumor redox environment using EPR spectroscopy', *Mol Cell Biochem,* 234-235 (1-2), 393-8.
85. Isaacs J. T., et al. (1986), 'Establishment and characterization of seven Dunning rat prostatic cancer cell lines and their use in developing methods for predicting metastatic abilities of prostatic cancers', *Prostate,* 9 (3), 261-81.
86. Janssen H. L., et al. (2005), 'Hypoxia in head and neck cancer: how much, how important?', *Head Neck,* 27 (7), 622-38.
87. Jiang L., et al. (2004), 'Comparison of BOLD contrast and Gd-DTPA Dynamic Contrast Enhanced imaging in rat prostate tumor', *Magn Reson Med,* 51, 953-60.
88. Jordan B. F., et al. (2005), 'Dynamic contrast-enhanced and diffusion MRI show rapid and dramatic changes in tumor microenvironment in response to inhibition of HIF-1alpha using PX-478', *Neoplasia,* 7 (5), 475-85.
89. Jordan B. F., et al. (2006), 'Complex relationship between changes in oxygenation status and changes in R*2: the case of insulin and NS-398, two inhibitors of oxygen consumption', *Magn ResonMed,* 56 (3), 637-43.
90. Jordan B.F., Cron, G.O., and Gallez, B (2009), 'Rapid Monitoring of oxygenation by 19F magnetic Resonance Imaging: simultaneous comparison with fluorescence quenching', *Mag Res Med,* 61 (3), 634-8.
91. Joseph P., et al. (1994), 'The role of specific reductases in the intracellular activation and binding of 2-nitroimidazoles', *Int J Radiat Oncol Biol Phys,* 29 (2), 351-55.
92. Joyce J. A. and Pollard, J. W. (2009), 'Microenvironmental regulation of metastasis', *Nat Rev Cancer,* 9 (4), 239-52.
93. Karczmar G. S., et al. (1994), 'Effects of hyperoxia on T2* and resonance frequency weighted magnetic resonance images of rodent tumours', *NMR Biomed,* 7 (1-2), 3-11.

94. Khan N., et al. (2007), 'Repetitive Tissue pO(2) Measurements by Electron Paramagnetic Resonance Oximetry: Current Status and Future Potential for Experimental and Clinical Studies', *Antioxid Redox Signal,* 9 (8), 1169-82.
95. Knox R. J., Knight, R. C., and Edwards, D. I. (1983), 'Studies on the action of nitroimidazole drugs. The products of nitroimidazole reduction', *Biochem Pharmacol,* 32 (14), 2149-56.
96. Koch C. J. and Evans, S. M. (1996), 'Cysteine concentrations in rodent tumors: unexpectedly high values may cause therapy resistance', *Int J Cancer,* 67 (5), 661-7.
97. Koch C. J. (2002), 'Measurement of absolute oxygen levels in cells and tissues using oxygen sensors and 2-nitroimidazole EF5', *Methods Enzymol,* 352, 3-31.
98. Kodibagkar V. D., et al. (2006), 'Novel 1H NMR approach to quantitative tissue oximetry using hexamethyldisiloxane', *Magn ResonMed,* 55 (4), 743-48.
99. Kodibagkar V. D., Wang, X., and Mason, R. P. (2008), 'Physical principles of quantitative nuclear magnetic resonance oximetry', *Front Biosci,* 13, 1371-84.
100. Kodibagkar V. D., et al. (2008), 'Proton imaging of siloxanes to map tissue oxygenation levels (PISTOL): a tool for quantitative tissue oximetry', *NMR Biomed,* 21 (8), 899-907.
101. Kosower N. S. and Kosower, E. M. (1978), 'The glutathione status of cells', *Int Rev Cytol,* 54, 109-60.
102. Krause B. J., et al. (2006), 'PET and PET/CT studies of tumor tissue oxygenation', *Q J Nucl Med Mol Imaging,* 50 (1), 28-43.
103. Krohn K. A., Link, J. M., and Mason, R. P. (2008), 'Molecular imaging of hypoxia', *J Nucl Med,* 49 (Suppl 2), 129S-48S.
104. Kuppusamy P., et al. (1998), 'In vivo electron paramagnetic resonance imaging of tumor heterogeneity and oxygenation in a murine model', *Cancer Res,* 58 (7), 1562-8.
105. Kuppusamy P., et al. (2002), 'Noninvasive imaging of tumor redox status and its modification by tissue glutathione levels', *Cancer Res,* 62 (1), 307-12.
106. La-Scalea M. A., et al. (2002), 'Voltammetric behavior of benznidazole at a DNA-electrochemical biosensor', *J Pharm Biomed Anal,* 29 (3), 561-8.
107. Le Q. T., et al. (2008), 'In vivo 1H magnetic resonance spectroscopy of lactate in patients with stage IV head and neck squamous cell carcinoma', *Int J Radiat Oncol Biol Phys,* 71 (4), 1151-7.
108. Lee C. P., et al. (2009), 'A phase I study of the nitroimidazole hypoxia marker SR4554 using 19F magnetic resonance spectroscopy', *Br J Cancer,* 101 (11), 1860-68.
109. Levy E. J., Anderson, M. E., and Meister, A. (1993), 'Transport of glutathione diethyl ester into human cells', *Proc Natl Acad Sci U S A,* 90 (19), 9171-5.
110. Lewa C.J. and Majewska, Z. (1980), 'Temperature relationships of proton spin-lattice relaxation time T1 in biological tissues', *Bull Cancer,* 67 (5), 35.
111. Li C. W., et al. (1996), 'Metabolic characterization of human soft tissue sarcomas in vivo and in vitro using proton-decoupled phosphorus magnetic resonance spectroscopy', *Cancer Res,* 56 (13), 2964-72.
112. Liao D., et al. (2007), 'Hypoxia-inducible factor-1alpha is a key regulator of metastasis in a transgenic model of cancer initiation and progression', *Cancer Res,* 67 (2), 563-72.
113. Liu H., et al. (2004), 'Near infrared spectroscopy and imaging of tumor vascular oxygenation', *Methods Enzymol,* 386, 349-78.
114. Ljungkvist A. S., et al. (2007), 'Dynamics of tumor hypoxia measured with bioreductive hypoxic cell markers', *Radiat Res,* 167 (2), 127-45.
115. Long A., Parrick, J., and Hodgkiss, R. J. (1991), 'An efficient procedure for the 1-alkylation of 2-nitroimidazoles and the synthesis of a probe for hypoxia in solid tumours', *Synthesis,* (9), 709-13.
116. Mahy P., et al. (2003), 'In vivo colocalization of 2-nitroimidazole EF5 fluorescence intensity and electron paramagnetic resonance oximetry in mouse tumors', *Radiother Oncol,* 67 (1), 53-61.
117. Malinen E., et al. (2006), 'Adapting radiotherapy to hypoxic tumours', *Physics in Medicine and Biology,* 51 (19), 4903-21.

118. Mansfield K. D., Simon, M. C., and Keith, B. (2004), 'Hypoxic reduction in cellular glutathione levels requires mitochondrial reactive oxygen species', *J Appl Physiol,* 97 (4), 1358-66.
119. Manzoor A. A., Schroeder, T., and Dewhirst, M. W. (2008), 'One-stop-shop tumor imaging: buy hypoxia, get lactate free', *Journal of Clinical Investigation,* 118 (5), 1616-19.
120. Mason R. P., Rodbumrung, W., and Antich, P. P. (1996), 'Hexafluorobenzene: a sensitive 19F NMR indicator of tumor oxygenation', *NMR Biomed,* 9 (3), 125-34.
121. Mason R. P., Ran, S., and Thorpe, P. E. (2002), 'Quantitative assessment of tumor oxygen dynamics: molecular imaging for prognostic radiology', *J Cell Biochem Suppl,* 39, 45-53.
122. Mason R. P., et al. (2003), 'Tumor oximetry: comparison of 19F MR EPI and electrodes', *Adv Exp Med Biol,* 530, 19-27.
123. Mason R.P., Shukla, H., and Antich, P.P. (1993), 'In vivo oxygen tension and temperature: simultaneous determination using 19F NMR spectroscopy of perfluorocarbon', *Magn Reson Med,* 29, 296-302.
124. Mason R.P., et al. (2010), 'Multimodality imaging of hypoxia in preclinical settings', *QJ Nucl Med Mol Imaging,* 54, 259-80.
125. Matsumoto K., et al. (2006), 'MR assessment of changes of tumor in response to hyperbaric oxygen treatment', *Magn Reson Med,* 56 (2), 240-6.
126. Maxwell P. H. (2005), 'The HIF pathway in cancer', *Semin Cell Dev Biol,* 16 (4-5), 523-30.
127. Maxwell R. J., Workman, P., and Griffiths, J. R. (1989), 'Demonstration of tumor-selective retention of fluorinated nitroimidazole probes by 19F magnetic resonance spectroscopy in vivo', *Int J Radiat Oncol Biol Phys,* 16 (4), 925-9.
128. McClelland R. A., Panicucci, R., and Rauth, A. M. (1985), 'Electrophilic intermediate in the reactions of a 2-(hydroxyamino)imidazole. A model for biological effects of reduced nitroimidazoles', *J Am Chem Soc,* 107 (6), 1762-63.
129. McIntyre D. J., McCoy, C. L., and Griffiths, J. R. (1999), 'Tumour oxygenation measurements by 19 F magnetic resonance imaging of perfluorocarbons', *Curr Sci,* 76 (6), 753-62.
130. McPhail L. D. and Robinson, S. P. (2010), 'Intrinsic Susceptibility MR Imaging of Chemically Induced Rat Mammary Tumors: Relationship to Histologic Assessment of Hypoxia and Fibrosis', *Radiology,* 254 (1), 110-18.
131. McSheehy Paul M. J., et al. (2010), 'Quantified Tumor T1 Is a Generic Early-Response Imaging Biomarker for Chemotherapy Reflecting Cell Viability', *Clin Cancer Res,* 16 (1), 212-25.
132. Meads M. B., Gatenby, R. A., and Dalton, W. S. (2009), 'Environment-mediated drug resistance: a major contributor to minimal residual disease', *Nat Rev Cancer,* 9 (9), 665-74.
133. Menon C. and Fraker, D. L. (2005), 'Tumor oxygenation status as a prognostic marker', *Cancer Lett,* 221 (2), 225-35.
134. Moeller B. J., et al. (2004), 'The relationship between hypoxia and angiogenesis', *Semin Radiat Oncol,* 14 (3), 215-21.
135. Mongan P. D., et al. (2002), 'Pyruvate improves redox status and decreases indicators of hepatic apoptosis during hemorrhagic shock in swine', *Am J Physiol Heart Circ Physiol,* 283 (4), H1634-44.
136. Moreno-Merlo F., Nicklee, T., and Hedley, D. W. (1999), 'Association between tissue hypoxia and elevated non-protein sulphydryl concentrations in human cervical carcinoma xenografts', *Br J Cancer,* 81 (6), 989-93.
137. Moreno S. N., Mason, R. P., and Docampo, R. (1984), 'Reduction of nifurtimox and nitrofurantoin to free radical metabolites by rat liver mitochondria. Evidence of an outer membrane-located nitroreductase', *J Biol Chem,* 259 (10), 6298-305.
138. Munn L. L. (2003), 'Aberrant vascular architecture in tumors and its importance in drug-based therapies', *Drug Discov Today,* 8 (9), 396-403.
139. Munoz-Chapuli R., Quesada, A. R., and Medina, A. M. (2004), 'Angiogenesis and signal transduction in endothelial cells', *Cell Mol Life Sci,* 61 (17), 2224-43.
140. Nagasawa H., et al. (2006), 'Design of hypoxia-targeting drugs as new cancer chemotherapeutics', *Biol Pharm Bull,* 29 (12), 2335-42.

141. Ndubuizu O. and La Manna, J. C. (2007), 'Brain Tissue Oxygen Concentration Measurements', *Antioxid Redox Signal,* 9 (8), 1207-19.
142. Negendank W. G., et al. (1995), 'Metabolic characterization of human non-Hodgkin's lymphomas in vivo with the use of proton-decoupled phosphorus magnetic resonance spectroscopy', *Cancer Res,* 55 (15), 3286-94.
143. Neubauer A. M., et al. (2008), 'Gadolinium-modulated ^{19}F signals from perfluorocarbon nanoparticles as a new strategy for molecular imaging', *Magn Reson Med,* 60 (5), 1066-72.
144. Nilsson H., et al. (2005), 'HIF-2alpha expression in human fetal paraganglia and neuroblastoma: relation to sympathetic differentiation, glucose deficiency, and hypoxia', *Exp Cell Res,* 303 (2), 447-56.
145. Nordsmark M., et al. (2005), 'Prognostic value of tumor oxygenation in 397 head and neck tumors after primary radiation therapy. An international multi-center study', *Radiother Oncol,* 77 (1), 18-24.
146. O'Connor J. P., et al. (2007), 'Organ-specific effects of oxygen and carbogen gas inhalation on tissue longitudinal relaxation times', *Magn Reson Med,* 58 (3), 490-96.
147. O'Connor J. P., et al. (2009), 'Comparison of normal tissue R1 and R*2 modulation by oxygen and carbogen', *Magn Reson Med* 61 (1), 75-83.
148. O'Connor James P. B., et al. (2009), 'Preliminary study of oxygen-enhanced longitudinal relaxation in MRI: a potential novel biomarker of oxygenation changes in solid tumors', *Int J Radiat Oncol Biol Phys,* 75 (4), 1209-15.
149. Ogunrinu T. A. and Sontheimer, H. (2010), 'Hypoxia increases the dependence of glioma cells on glutathione', *J Biol Chem,* 285 (48), 37716-24.
150. Olive P. L. (1979), 'Inhibition of DNA synthesis by nitroheterocycles. I. Correlation with half-wave reduction potential', *Br J Cancer,* 40 (1), 89-93.
151. Olive P. L., Banath, J. P., and quino-Parsons, C. (2001), 'Measuring hypoxia in solid tumours--is there a gold standard?', *Acta Oncol,* 40 (8), 917-23.
152. Overgaard J. and Horsman, M. R. (1996), 'Modification of hypoxia-induced radioresistance in tumors by the use of oxygen and sensitizers', *Semin Radiat Oncol,* 6, 10-21.
153. Overgaard J. (2007), 'Hypoxic radiosensitization: adored and ignored', *J Clin Oncol,* 25 (26), 4066-74.
154. Overgaard J. (2011), 'Hypoxic modification of radiotherapy in squamous cell carcinoma of the head and neck--a systematic review and meta-analysis', *Radiother Oncol,* 100 (1), 22-32.
155. Pacheco-Torres J., et al. (2006), 'A Convenient and Efficient Synthesis of the First (Nitroimidazolyl)succinic Esters and their Diacids', *Synthesis,* 22, 3859-64.
156. Pacheco-Torres J., et al. More FREDOM: Evaluation of Lung Tumor Oxygenation in Rats. Proceedings of the 16th Annual Meeting ISMRM 2008 2008; Toronto, Canada. p 5339.
157. Pacheco-Torres J., et al. (2011), 'Imaging tumor hypoxia by magnetic resonance methods', *NMR Biomed,* 24 (1), 1-16.
158. Padhani A. R., et al. (2007), 'Imaging oxygenation of human tumours', *Eur Radiol,* 17 (4), 861-72.
159. Parhami Pejman and Fung, B. M. (1983), 'Fluorine-19 relaxation study of perfluoro chemicals as oxygen carriers', *J Phys Chem,* 87 (11), 1928-31.
160. Pathania M., Yan, L. D., and Bordey, A. (2010), 'A symphony of signals conducts early and late stages of adult neurogenesis', *Neuropharmacology,* 58 (6), 865-76.
161. Pavlik Christopher, et al. (2011), 'Synthesis and fluorescent characteristics of imidazole–indocyanine green conjugates', *Dyes and Pigments,* 89 (1), 9-15.
162. Pendyala L., et al. (1997), 'Translational studies of glutathione in bladder cancer cell lines and human specimens', *Clin Cancer Res,* 3 (5), 793-8.
163. Pennacchietti S., et al. (2003), 'Hypoxia promotes invasive growth by transcriptional activation of the met protooncogene', *Cancer Cell,* 3 (4), 347-61.
164. Perez-Mayoral E., et al. (2007), 'Dimethyl (2E)-2-(4-nitro-1H-imidazol-1-yl)but-2-enedioate', *Acta Crystallographica Section E-Structure Reports Online,* 63, O1790-O91.

165. Pijnenborg J. M., et al. (2007), 'Hypoxia contributes to development of recurrent endometrial carcinoma', *Int J Gynecol Cancer,* 17 (4), 897-904.
166. Piret J. P., et al. (2004), 'Hypoxia and CoCl2 protect HepG2 cells against serum deprivation- and t-BHP-induced apoptosis: a possible anti-apoptotic role for HIF-1', *Exp Cell Res,* 295 (2), 340-49.
167. Pitson G., et al. (2001), 'Tumor size and oxygenation are independent predictors of nodal diseases in patients with cervix cancer', *Int J Radiat Oncol Biol Phys,* 51 (3), 699-703.
168. Pouyssegur J., Dayan, F., and Mazure, N. M. (2006), 'Hypoxia signalling in cancer and approaches to enforce tumour regression', *Nature,* 441 (7092), 437-43.
169. Procissi D., et al. (2007), 'In vivo 19F magnetic resonance spectroscopy and chemical shift imaging of tri-fluoro-nitroimidazole as a potential hypoxia reporter in solid tumors', *Clin Cancer Res,* 13 (12), 3738-47.
170. Raleigh J. A., et al. (1986), 'Covalent binding of a fluorinated 2-nitroimidazole to EMT-6 tumors in Balb/C mice: detection by F-19 nuclear magnetic resonance at 2.35 T', *Int J Radiat Oncol Biol Phys,* 12 (7), 1243-45.
171. Raleigh J. A., et al. (1991), 'Development of an in vivo 19F magnetic resonance method for measuring oxygen deficiency in tumors', *Magn ResonMed,* 22 (2), 451-66.
172. Righi V., et al. (2009), '1H HR-MAS and genomic analysis of human tumor biopsies discriminate between high and low grade astrocytomas', *NMR Biomed,* 22 (6), 629-37.
173. Robinson S. P., Howe, F. A., and Griffiths, J. R. (1995), 'Noninvasive monitoring of carbogen-induced changes in tumor blood flow and oxygenation by functional magnetic resonance imaging', *Int J Radiat Oncol Biol Phys,* 33 (4), 855-59.
174. Robinson S. P. and Griffiths, J. R. (2004), 'Current issues in the utility of 19F nuclear magnetic resonance methodologies for the assessment of tumour hypoxia', *Philos Trans R Soc Lond B Biol Sci,* 359 (1446), 987-96.
175. Robinson S. P. , et al. (2003), 'Tumor vascular architecture and function evaluated by non-invasive susceptibility MRI methods and immunohistochemistry', *J Magn Reson Imaging,* 17, 445-54.
176. Rodrigues L., et al. (2004), 'Tumor R2* is a prognostic indicator of acute radiotherapeutic response in rodent tumors', *J Magn Reson Imaging,* 19 (4), 482-88.
177. Rost J. and Rapoport, S. (1964), 'Reduction-Potential of Glutathione', *Nature,* 201, 185.
178. Roudier E., Bachelet, C., and Perrin, A. (2007), 'Pyruvate reduces DNA damage during hypoxia and after reoxygenation in hepatocellular carcinoma cells', *FEBS J,* 274 (19), 5188-98.
179. Ruas J. L. and Poellinger, L. (2005), 'Hypoxia-dependent activation of HIF into a transcriptional regulator', *Semin Cell Dev Biol,* 16 (4-5), 514-22.
180. Salmon H. W. and Siemann, D. W. (2004), 'Utility of 19F MRS detection of the hypoxic cell marker EF5 to assess cellular hypoxia in solid tumors', *Radiother Oncol,* 73 (3), 359-66.
181. Schafer F. Q. and Buettner, G. R. (2001), 'Redox environment of the cell as viewed through the redox state of the glutathione disulfide/glutathione couple', *Free Radic Biol Med,* 30 (11), 1191-212.
182. Schroedl C., et al. (2002), 'Hypoxic but not anoxic stabilization of HIF-1alpha requires mitochondrial reactive oxygen species', *Am J Physiol Lung Cell Mol Physiol,* 283 (5), L922-31.
183. Seddon B. M., et al. (2002), 'Validation of the fluorinated 2-nitroimidazole SR-4554 as a noninvasive hypoxia marker detected by magnetic resonance spectroscopy', *Clin Cancer Res,* 8 (7), 2323-35.
184. Seddon B. M., et al. (2003), 'A phase I study of SR-4554 via intravenous administration for noninvasive investigation of tumor hypoxia by magnetic resonance spectroscopy in patients with malignancy', *Clin Cancer Res,* 9 (14), 5101-12.
185. Seddon B. M. and Workman, P. (2003), 'The role of functional and molecular imaging in cancer drug discovery and development', *Br J Radiol,* 76 (Spec No 2), S128-S38.
186. Seimiya H., et al. (1999), 'Hypoxia up-regulates telomerase activity via mitogen-activated protein kinase signaling in human solid tumor cells', *Biochem Biophys Res Commun,* 260 (2), 365-70.

187. Semenza G. L. (2003), 'Targeting HIF-1 for cancer therapy', *Nat Rev Cancer,* 3 (10), 721-32.
188. Shi Y. H. and Fang, W. G. (2004), 'Hypoxia-inducible factor-1 in tumour angiogenesis', *World J Gastroenterol,* 10 (8), 1082-87.
189. Singh A. S., Radu, C. G., and Ribas, A. (2010), 'PET imaging of the immune system: immune monitoring at the whole body level', *Q J Nucl Med Mol Imaging,* 54 (3), 281-90.
190. Sloane B. F., et al. (2006), 'I2 imaging: cancer biology and the tumor microenvironment', *Cancer Res,* 66 (23), 11097-9.
191. Smith B. R. (1984), 'Hypoxia-enhanced reduction and covalent binding of [2-3H]misonidazole in the perfused rat liver', *Biochem Pharmacol,* 33 (8), 1379-81.
192. Smith B. R. and Born, J. L. (1984), 'Metabolism and excretion of [3H]misonidazole by hypoxic rat liver', *Int J Radiat Oncol Biol Phys,* 10 (8), 1365-70.
193. Stephen R.N. and Gillies, R.J. (2007), 'Promise and progress for functional and molecular imaging response to targetted therapies', *Pharmaceutical Research,* 24 (6), 1172-85.
194. Swartz H. M., et al. (2004), 'Clinical applications of EPR: overview and perspectives', *NMR Biomed,* 17 (5), 335-51.
195. Taoufik E. and Probert, L. (2008), 'Ischemic neuronal damage', *Curr Pharm Des,* 14 (33), 3565-73.
196. Tatum J. L., et al. (2006), 'Hypoxia: importance in tumor biology, noninvasive measurement by imaging, and value of its measurement in the management of cancer therapy', *Int J Radiat Biol,* 82 (10), 699-757.
197. Thomas S. R., et al. (1994), 'Evaluation of the influence of the aqueous phase bioconstituent environment on the F-19 T1 of perfluorocarbon blood substitute emulsions', *J Magn Reson Imaging,* 4 (4), 631-35.
198. Thorwarth D., et al. (2007), 'Hypoxia dose painting by numbers: a planning study', *Int J Radiat Oncol Biol Phys,* 68 (1), 291-300.
199. van Sluis R., et al. (1999), 'In vivo imaging of extracellular pH using 1H MRSI', *Magn Reson Med,* 41 (4), 743-50.
200. Varghese A. J., Gulyas, S., and Mohindra, J. K. (1976), 'Hypoxia-dependent reduction of 1-(2-nitro-1-imidazolyl)-3-methoxy-2-propanol by Chinese hamster ovary cells and KHT tumor cells in vitro and in vivo', *Cancer Res,* 36 (10), 3761-65.
201. Varghese A. J. (1983), 'Glutathione conjugates of misonidazole', *Biochem Biophys Res Commun,* 112 (3), 1013-20.
202. Varghese A. J. and Whitmore, G. F. (1984), 'Misonidazole-glutathione conjugates in CHO cells', *Int J Radiat Oncol Biol Phys,* 10 (8), 1341-5.
203. Varghese A. J. and Whitmore, G. F. (1985), 'Properties of 2-hydroxylaminoimidazoles and their implications for the biological effects of 2-nitroimidazoles', *Chem Biol Interact,* 56 (2-3), 269-87.
204. Varghese A. J. and Whitmore, G. F. (1986), 'Identification of a reactive glutathione conjugate as a metabolite of SR-2508 in CHO cells', *Int J Radiat Oncol Biol Phys,* 12 (7), 1223-6.
205. Vaupel P., Kelleher, D. K., and Hockel, M. (2001), 'Oxygen status of malignant tumors: pathogenesis of hypoxia and significance for tumor therapy', *Semin Oncol,* 28 (2 Suppl 8), 29-35.
206. Vaupel P., et al. (2003), 'Oxygenation gain factor: a novel parameter characterizing the association between hemoglobin level and the oxygenation status of breast cancers', *Cancer Res,* 63 (22), 7634-37.
207. Vaupel P. and Harrison, L. (2004), 'Tumor hypoxia: causative factors, compensatory mechanisms, and cellular response', *Oncologist,* 9 Suppl 5, 4-9.
208. Vaupel P., Mayer, A., and Hockel, M. (2004), 'Tumor hypoxia and malignant progression', *Methods Enzymol,* 381, 335-54.
209. Vaupel P., et al. (2005), 'Hypoxia in breast cancer: role of blood flow, oxygen diffusion distances, and anemia in the development of oxygen depletion', *Adv Exp Med Biol,* 566, 333-42.
210. Vaupel P., Hockel, M., and Mayer, A. (2007), 'Detection and Characterization of Tumor Hypoxia Using pO(2) Histography', *AntioxidRedoxSignal*.

211. Vaupel Peter, Höckel, Michael, and Mayer, Arnulf (2007), 'Detection and Characterization of Tumor Hypoxia Using pO2 Histography', *Antioxid Redox Signal,* 9 (8), 1221-36.
212. Vikram D. S., Zweier, J. L., and Kuppusamy, P. (2007), 'Methods for noninvasive imaging of tissue hypoxia', *Antioxid Redox Signal,* 9 (10), 1745-56.
213. Viode C., et al. (1999), 'Enzymatic reduction studies of nitroheterocycles', *Biochem Pharmacol,* 57 (5), 549-57.
214. Vukovic V., Nicklee, T., and Hedley, D. W. (2000), 'Microregional heterogeneity of non-protein thiols in cervical carcinomas assessed by combined use of HPLC and fluorescence image analysis', *Clin Cancer Res,* 6 (5), 1826-32.
215. Vukovic V., Nicklee, T., and Hedley, D. W. (2002), 'Multiparameter fluorescence mapping of nonprotein sulfhydryl status in relation to blood vessels and hypoxia in cervical carcinoma xenografts', *Int J Radiat Oncol Biol Phys,* 52 (3), 837-43.
216. Walton M. I. and Workman, P. (1987), 'Nitroimidazole bioreductive metabolism. Quantitation and characterisation of mouse tissue benznidazole nitroreductases in vivo and in vitro', *Biochem Pharmacol,* 36 (6), 887-96.
217. Wardman Peter (1989), 'Reduction Potentials of One-Electron Couples Involving Free Radicals in Aqueous Solution', *J Phys Chem Ref Data,* 18 (4), 1637-755.
218. Whitmore G. F. and Varghese, A. J. (1986), 'The biological properties of reduced nitroheterocyclics and possible underlying biochemical mechanisms', *Biochem Pharmacol,* 35 (1), 97-103.
219. Wong D. Y., et al. (1994), 'Glutathione concentration in oral cancer tissues', *Cancer Lett,* 81 (2), 111-6.
220. Wouters B. G. and Brown, J. M. (1997), 'Cells at intermediate oxygen levels can be more important than the "hypoxic fraction" in determining tumor response to fractionated radiotherapy', *Radiat Res,* 147 (5), 541-50.
221. Wouters B. G., et al. (2005), 'Control of the hypoxic response through regulation of mRNA translation', *Semin Cell Dev Biol,* 16 (4-5), 487-501.
222. Xiang S., Pan, W., and Kastin, A. J. (2005), 'Strategies to create a regenerating environment for the injured spinal cord', *Curr Pharm Des,* 11 (10), 1267-77.
223. Yamada K. I., et al. (2002), 'Feasibility and assessment of non-invasive in vivo redox status using electron paramagnetic resonance imaging', *Acta Radiol,* 43 (4), 433-40.
224. Yang Y. and Xing, L. (2005), 'Towards biologically conformal radiation therapy (BCRT): Selective IMRT dose escalation under the guidance of spatial biology distribution', *Medical Physics,* 32 (6), 1473-84.
225. Yu J-X., et al. (2008), 'Non-invasive physiology and pharmacology using ^{19}F magnetic resonance', in Tressaud A. and G. Haufe (eds.), *Fluorine and Health* (Elsevier B.V.), 198-276.
226. Zhao D., et al. (2002), 'Differential oxygen dynamics in two diverse Dunning prostate R3327 rat tumor sublines (MAT-Lu and HI) with respect to growth and respiratory challenge', *Int J Radiat Oncol Biol Phys,* 53 (3), 744-56.
227. Zhao D., et al. (2003), 'Correlation of Tumor Oxygen Dynamics with Radiation Response of the Dunning Prostate R3327-HI Tumor', *Radiat Res,* 159, 621-31.
228. Zhao D., et al. (2003), 'Tumor oxygen dynamics: correlation of in vivo MRI with histological findings', *Neoplasia,* 5 (4), 308-18.
229. Zhao D., Jiang, L., and Mason, R. P. (2004), 'Measuring changes in tumor oxygenation', *Methods Enzymol,* 386, 378-418.
230. Zhao D., et al. (2009), 'Comparison of ^{1}H blood oxygen level-dependent (BOLD) and ^{19}F MRI to investigate tumor oxygenation', *Magn Reson Med,* 62 (2), 357-64.
231. Ziemer L. S., et al. (2005), 'Oxygen distribution in murine tumors: characterization using oxygen-dependent quenching of phosphorescence', *J Appl Physiol,* 98 (4), 1503-10.